Light Water Reactor Sustainability Program

Multi-Hazard Advanced Seismic Probabilistic Risk Assessment Tools and Applications

Justin L. Coleman
Chandu Bolisetti
Swetha Veeraraghavan
Carlo Parisi
Steven R. Prescott
Abhinav Gupta
Annie M. Kammerer

Light Water Reactor Sustainability Program

Multi-Hazard Advanced Seismic Probabilistic Risk Assessment Tools and Applications

Justin L. Coleman
Chandu Bolisetti
Swetha Veeraraghavan
Carlo Parisi
Steven R. Prescott
Abhinav Gupta
Annie M. Kammerer

September 2016

Idaho National Laboratory
Idaho Falls, Idaho 83415
http://www.inl.gov

EXECUTIVE SUMMARY

Design of nuclear power plant (NPP) facilities to resist natural hazards has been a part of the regulatory process from the beginning of the NPP industry in the United States, but has evolved substantially over time. The original set of approaches and methods was entirely deterministic in nature and focused on a traditional engineering margins-based approach. However, over time probabilistic and risk-informed approaches were also developed and implemented in US Nuclear Regulatory Commission guidance and regulation. A defense-in-depth framework has also been incorporated into US regulatory guidance over time. As a result, today, the US regulatory framework incorporates deterministic and probabilistic approaches for a range of different applications and for a range of natural hazard considerations.

Although the US regulatory framework has continued to evolve over time, the tools, methods and data available to the US nuclear industry to meet the changing requirements have not kept pace. Notably, there is room for improvement in the tools and methods available for external event probabilistic risk assessment (PRA), which is the principal assessment approach used in risk-informed regulations and risk-informed decision-making applied to natural hazard assessment and design. Development of a new set of tools and methods that incorporate current knowledge, modern best practice, and state-of-the-art computational resources would lead to more reliable assessment of facility risk and risk insights (e.g., the plant elements and accident sequences that are most risk-significant), with less uncertainty and reduced conservatisms.

Development of the next generation tools and methods for external events PRA is ongoing under the Risk Informed Safety Margins Characterization (RISMC) technical pathway. Toolkit success centers on integration of the tools and methods under a common framework, MOOSE. These tools and methods make use of existing and newly developed tools and methods, coupled with the experience and data gained in the past decades, to define and analyze more realistic risk assessment models. Specific focus in this report is on the capability to model external hazards, with focus on seismically induced flooding, using dynamic PRA. The following RISMC based codes are discussed in the report, Mastodon (nonlinear seismic soil-structure interaction), Neutrino (flood progression and Structure, System, and Components (SSC) impact), and EMRALD (dynamic PRA tool).

Significant capability has been added to Mastodon to simulate 3-D wave passage effects through nonlinear soil. Verification has demonstrated the capability of Mastodon to model wave passage effects in 1-D, 2-D, and 3-D. Additional capability will be added to Mastodon over the next year to implement a robust gapping and sliding element for cyclic shaking, web-based verification and user manuals, stochastic finite elements, and frequency independent damping. Verification of added capabilities will occur in parallel with code writing activities. The Table below provides an overview of the planned activities for FY 2017.

LWRS (FY 2015 and FY 2016)	LWRS (FY 2017)
Newmark Beta Time Integration	Gapping and Sliding Element for Cyclic Shaking
Hilber-Hughes-Taylor Time Integration	Web-based Verification and User Manuals
Nonlinear Soil Constitutive Model (Soil-HYS)	Frequency Independent Damping
Soil-Foundation Interaction, Gapping and Sliding (Under Development)	Verification of New Capabilities
	Beta Version of Mastodon

Neutrino provides an advanced graphical user interface that makes it easy to visualize the in-progress model. Neutrino provides a mesh-less based smooth particle hydrodynamic approach for simulating both internal and external flooding. Neutrino allows for different types of particle emitters: a flow rate particle emitter that can be used to simulate water flow through a penetration or a pipe break; a Toricelli emitter that creates particles to match a given rainfall rate, surface area, and opening; a teleport emitter that moves particles from one level to another simulating the flow through a pipe. Other emitter options and validation tests are in development.

EMRALD is a dynamic PRA code based on three-phased discrete event simulation. EMRALD communicates with both the seismic and flooding tools to calculate risk. A model for EMRALD consists of States with immediate actions, and conditional event actions. Many different types of events and actions can be evaluated or executed, designed in a way for easy equivalents to items in traditional PRA such as basic events and fault trees. States can also be tagged as "key states" and are noted if a simulation run ends on that state. Through multiple runs of the simulation model, probabilities of each key state are derived. In addition, heuristics can be made to show the path or cause of the key state and the times of those events.

The advanced seismic PRA demonstration presented implements nonlinear gapping and sliding (differential movement between a NPP foundation and the soil) into seismic PRA calculations to quantify the impact on fragilities of SSCs. The results of the demonstration show that gapping and sliding are important parameters that should be considered when quantifying seismic risk at sites with higher seismic hazard curves. The slope of the seismic hazard curve is also an important parameter in determining the final risk number.

The report presents a dynamic PRA calculation of seismically induced flooding coupled with thermal-hydraulics. In this demonstration RELAP5 was used to pre-calculate some core damage conditions and dynamically determine core damage. This demonstration provides a methodology for linking multiple tools together on a common computation platform to produce a more holistic result set. Current PRA calculations do not directly consider time dependent phenomena. These results indicate that time can be an important parameter to capture when performing PRA calculations.

FY 2017 will focus on coupling the seismic, flooding, and dynamic PRA capabilities in the MOOSE framework. Verification of capabilities will be a key focus of FY 2017. In addition RISMC is currently working with an industry partner to identify an industry application problem that the RISMC toolkit will evaluate in FY 2017.

CONTENTS

FIGURES

TABLES

ACRONYMS

1-D	One-Dimensional
2-D	Two-Dimensional
3-D	Three-Dimensional
AC	Alternating Current
AFW	Auxiliary Feed-Water
ASPRA	Advanced Seismic Probabilistic Risk Assessment
ATR	Advanced Test Reactor
CDF	Core Damage Frequency
CFR	Code of Federal Regulation
DOE	Department of Energy
ECST	Emergency Condensate Storage Tank
EE	External Events
EDG	Emergency Diesel Generator
EPRI	Electric Power Research Institute
ERG-EH	Experimental Research Group – External Hazards
EQ	Earthquake
ESF	Engineered Safeguards
FOM	Figure Of Merit
FSF	Fundamental Safety Functions
FTE	Full Time Equivalent
FY	Fiscal Year
GUI	Graphical User Interface
HPC	High Performance Computing
HPI	High Pressure Injection
HPIS	High Pressure Injection System
IA2	Industry Application 2
IGPWR	INL Generic Pressurized Water Reactor
INL	Idaho National Laboratory
ISRS	In-Structure Response Spectrum
LB-LOCA	Large Break LOCA

LOCA   Loss of Coolant Accident

LOOP   Loss of Offsite Power

LPIS   Low Pressure Injection System

LWR   Light Water Reactor

LWRS   Light Water Reactor Sustainability

MCC   Main Circulation Circuit

MCP   Main Coolant Pump

MAFE   Mean Annual Frequency of Exceedance

MFW   Main Feed-Water

MLE   Maximum Likelihood Estimate

MOOSE   Multi-Physics Object-Oriented Simulation Environment

MSLB   Main Steam Line Break

NC   Natural Circulation

NCSU   North Carolina State University

NEM   Nodal Expansion Method

NEP   Non-Exceedance Probability

NLSSI   Non-linear Soil-Structure-Interaction

NPP   Nuclear Power Plant

NRC   Nuclear Regulatory Commission

NUREG   Nuclear Regulatory Report

PCT   Peak Clad Temperature

PCTR   PCT Ratio

PGA   Peak Ground Acceleration

PIRT   Phenomena Identification and Ranking Table

PORV   Pilot-Operated Relief Valve

PRA   Probabilistic Risk Assessment

PRZ   Pressurizer

PSHA   Probabilistic Seismic Hazard Assessment

PWR   Pressurized Water Reactor

RA   Risk Assessment

RAVEN   Risk Analysis and Virtual Control Environment

RCS   Reactor Cooling System

RandD   Research and Development

RELAP5   Reactor Excursion and Leak Analysis Program 5
RELAP-7   Reactor Excursion and Leak Analysis Program 7
RHR   Residual Heat Removal System
RIMM   Risk-Informed Margin Management
RISMC   Risk Informed Safety Margin Characterization
ROM   Reduced Order Model
RPV   Reactor Pressure Vessel
RWST   Refueling Water Storage Tank
SA   Severe Accident
SBO   Station Black-Out
SG   Steam Generator
SPRA   Seismic Probabilistic Risk Assessment
SRV   Steam Relief Valve
SSCs   Structures, Systems, and Components
SSI   Soil-Structure-Interaction
SV   Safety Valve
TD-AFW   Turbine Driven Auxiliary Feed-Water
TH   Thermalhydraulic
UHS   Uniform Hazard Spectrum
US   United States

1. INTRODUCTION

Design of nuclear power plant (NPP) facilities to resist natural hazards has been a part of the regulatory process from the beginning of the NPP industry in the United States, but has evolved substantially over time. The original set of approaches and methods was entirely deterministic in nature and focused on a traditional engineering margins-based approach. However, over time probabilistic and risk-informed approaches were also developed and implemented in US Nuclear Regulatory Commission (NRC) guidance and regulation. A defense-in-depth framework has also been incorporated into US regulatory guidance over time. As a result, today, the US regulatory framework incorporates deterministic and probabilistic approaches for a range of different applications and for a range of natural hazard considerations. This framework will continue to evolve as a result of improved knowledge and newly identified regulatory needs and objectives, most notably in response to the NRC activities developed in response to the 2011 Fukushima accident in Japan.

Although the US regulatory framework has continued to evolve over time, the tools, methods and data available to the US nuclear industry to meet the changing requirements have not kept pace. Notably, there is room for improvement in the tools and methods available for external event probabilistic risk assessment (PRA), which is the principal assessment approach used in risk-informed regulations and risk-informed decision-making applied to natural hazard assessment and design. Development of a new set of tools and methods that incorporate current knowledge, modern best practice, and state-of-the-art computational resources would lead to more reliable assessment of facility risk and risk insights (e.g., the plant elements and accident sequences that are most risk-significant), with less uncertainty and reduced conservatisms.

Seismic Hazard and Risk

Probabilistic seismic hazard assessment (PSHA) and seismic probabilistic risk assessment (SPRA) approaches have been applied and improved for several decades and are now considered to be relatively mature in terms of their conceptual development and application. Unfortunately, the tools currently available for SPRA (of which PSHA is a part) are relatively inflexible and were developed principally for internal event PRAs. As a result, currently available tools are now significantly limiting the development of more advanced SPRA (ASPRA) methodologies.

Flood Hazard and Risk

There is also a recognized and growing need for tools and methods to assess risk from other natural phenomena, most notably flooding. Although flooding is an area of significant concern and focus for the US NRC and industry, in part as a result of the Fukushima accident, probabilistic hazard and risk assessment tools and methods for flooding are in their infancy. Although many elements of the tools and methods developed for seismic hazard and risk assessment can be applied to flooding assessments, significant challenges remain. In particular, the way in which floodwaters and seismic loads impact a NPP once they reach the site are fundamentally different. As a result, flood risk assessment methods must also incorporate robust time-domain physics-based modeling that can provide insight and information on realistic accident sequences, accident progression, and other inputs to both margins-based safety assessment tools and PRA tools.

Next Generation Tools and Methods for External Events Probabilistic Risk Assessment

Development of "next generation" seismic risk assessment tools and methods, which are built within the Idaho National Laboratory (INL) Risk Informed Safety Margin Characterization (RISMC) toolkit (discussed in detail in Section 0 of this report), would lead to significant improvements in

industry's ability to address regulatory requirements and make the most of regulatory opportunities (e.g., risk-informed relief) related to natural hazards. An overview of the ongoing development of a new set of ASPRA tools and methods being developed using INL's Multiphysics Object Oriented Simulation Environment (MOOSE) High Performance Computing framework (Gaston, Hansen, and Newman 2009) is shown in Figure 1. These tools are being developed to both integrate the existing large number of available modeling resources and fill in the gaps, as necessary, to address the risk from natural hazard phenomena. A key aspect of this integrated toolset is the use of dynamic PRA, which represents a significant improvement over current approaches, particularly in its ability to (1) incorporate time dependencies, to (2) incorporate multiple hazards and dependent hazards (e.g., seismically-induced flood), and to (3) quantify and carry uncertainties throughout the analysis.

Overview of this Report

This report discusses RISMC toolkit development for external hazards and provides two demonstrations on how the toolkit can be applied to nuclear power plant scenarios. Section 0 of this report provides background on the RISMC toolkit and discusses RISMC toolkit development for external hazards. Section 0 discusses tools in more depth, with a particular emphasis on three tools: Mastodon (a MOOSE-based code for NLSSI), Neutrino (a flooding assessment tool), and EMRALD (a dynamic PRA code). Section 4 describes two demonstration projects exploring the capabilities of the toolkit and demonstrating how the toolkit can be applied for analysis of integrated (multi-hazard) nuclear power plant scenarios. Section 4.1 focuses on new approaches and tools for enhanced nonlinear soil-structure-interaction (NLSSI) analysis, which addresses current issues related to interface between disciplines and provides more accurate best estimate results with reduced uncertainties. This section focuses on implementation of nonlinear gapping and sliding (differential movement between a NPP foundation and the soil) into SPRA calculations to quantify the impact on fragilities of SSCs. Section 4.2 describes demonstration project focused on a dynamic PRA application at a generic nuclear power plant. The dynamic PRA integrates seismic, flooding, and thermalhydraulic elements into a state-of-the-art dynamic PRA framework using EMRALD. Section 5 discusses the next steps in the ASPRA development efforts.

RISMC Toolkit for Advanced External Events PRA

Domain knowledge (earth science information, failure models, operational data, etc.)

Peacock (graphical user interface)

Scenarios and Controller for Dynamic PRA
EMRALD / RAVEN

Hazard Module (A) — hazard quantification → Hazard assessment

Neutrino (B) — flood progression/SSC impact

Grizzly (B&A) — material aging

LS-DYNA (B) Mastodon (A) — nonlinear soil-structure-interaction

RAVEN (B&A) — uncertainty quantification

RELAP5 (B) RELAP-7 (A) — thermalhydraulics/systems safety

Dynamic response of structures, systems and components

Fragility and human reliability modeling

Systems analysis

Advanced External Events PRA Methodology

RISMC Toolkit

(A) Advanced MOOSE-based tools under development
(B) Basic toolset - current practice MOOSE and non-MOOSE tools

MAMMOTH, BISON, etc.

Additional MOOSE-based resources as needed to support methodology

MOOSE (Solver framework)

Figure 1. Elements of the RISMC toolkit and their relation to Advanced Probabilistic Risk Assessment for External Events.

2.   ABOUT THE RISMC TOOLKIT

2.1   Background on the RISMC Toolkit

New methods and tools are under development in the RISMC toolkit, as shown in Figure 1. These tools can be applied to a variety of problems, including external event hazards. The RISMC toolkit can be used with in a risk-informed margins management (RIMM) approach to improve decision-making in managing NPP safety. The RIMM approach provides a technical framework to understand and address real world external hazard challenges, including those posed by the types of scenarios shown in (Figure 2). At a nuclear facility, an external hazard is a condition that may cause a deviation in the normal operation. External hazards of interest have a primary impact on the nuclear facility that may also lead to secondary phenomena. Examples of external hazards that cause primary impact are seismic shaking, flooding, and high winds. Examples of secondary phenomena induced by a seismic scenario are dam and levy failure, landslide, internal flood, and internal fire. These types of hazards complicate the determination of safety in any complex facility.   An example of how an event progresses in time is provided in Figure 3.

A key element of RIMM is an assessment of risk that considers all applicable external hazards together (as shown on the right side of Figure 4), instead the current approach calculates separately the risk from external hazards, even if they may have a common cause or other interrelations. The focus on RIMM provides a technical basis to understand and manage hazards. The tools available to develop the technical basis for use in RIMM incorporates the tools show in Figure 1, which are discussed in detail in Table 1, and also additional MOOSE-based tools that are developed outside the RISMC toolkit, as shown in Figure 5.
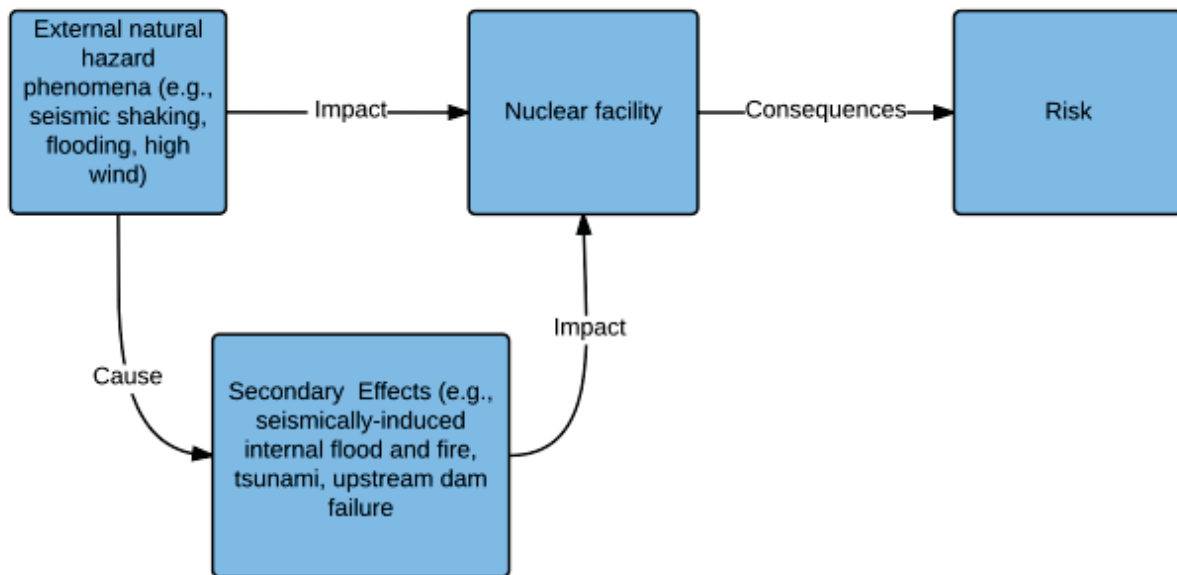
Figure 2.   Real world risk propagation at nuclear power plants
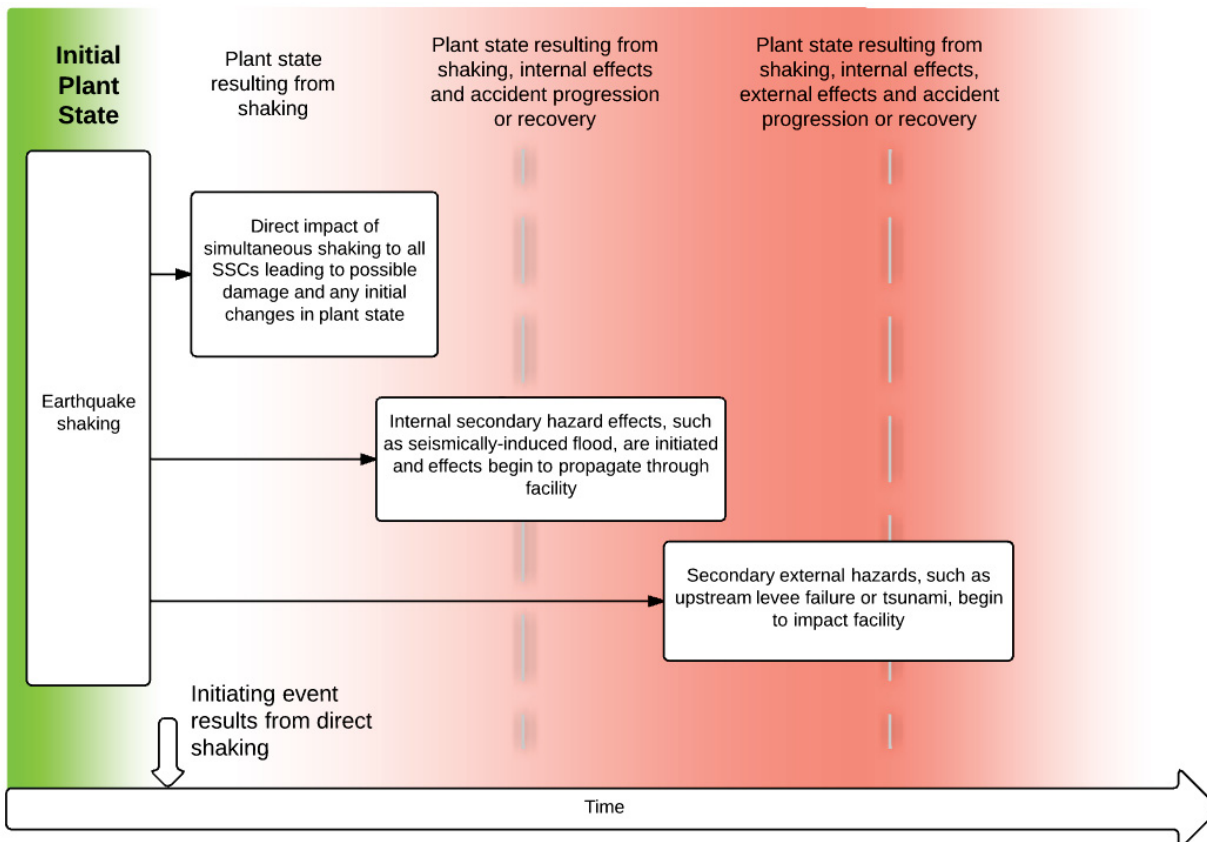
Figure 3.   Evolution of an external event over time.
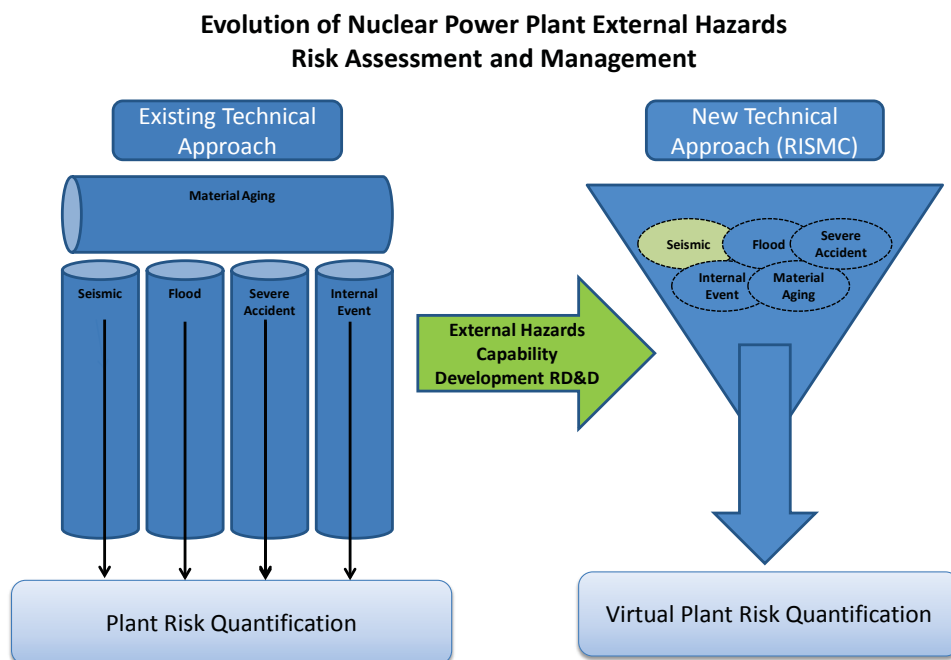
Figure 4.   Current risk calculation approach that generally considers external hazards separately versus the RIMM approach that considers external hazards together.

Table 1.   RISMC Toolkit advanced tools for dynamic probabilistic risk assessment

Advanced Tool	Capabilities
RELAP-7	RELAP-7 is a component-based integrated tool simulates nuclear plant energy and fluids systems behavior in normal, off-normal, and postulated accident scenarios. RELAP-7 builds upon the well-established and validated capabilities of nuclear systems codes (RELAP, TRAC, etc.) yet is extended by high-fidelity, multi-physics capabilities for new insight into nuclear plant safety. Implementing state of the art numerical methods and coupled multi-physics capabilities (via the MOOSE framework), enables the advancement of modern techniques for risk reduction and margin characterization, such as safety systems classification, thermal limit margin and fuel life cycle optimization, and maintenance program savings.
Grizzly	Grizzly simulates component ageing and damage evolution events for LWRS specific applications. Specifically, Grizzly will provide a simulation capability for: • Reactor Metals (embrittlement, fatigue, corrosion, etc.), such as Reactor Pressure Vessel and core internals • Weldment integrity • Concrete containment integrity subjected to a neutron flux, corrosive environment, and high temperatures and pressures.
Mastodon	Mastodon has the capability to model stochastic NLSSI in a risk framework coupled with virtual NPPs. These NLSSI simulations will include structural dynamics, time integration, dynamic porous media flow, hysteretic nonlinear soil constitutive models, hysteretic nonlinear structural constitutive models, and geometric nonlinearities at the foundation (gapping and sliding).
EMRALD/RAVEN	EMRALD and RAVEN are tools for dynamic probabilistic risk analysis, event sequence control, probabilistic evolution of accident scenarios. These tools use reduced order modeling used for uncertainty quantification.
Neutrino	Neutrino is a mesh-free, smooth particle hydrodynamics-based solver which also uses advanced boundary handling and adaptive time stepping. Neutrino is an accurate fluid solver and is being used simulate coastal inundation, river flooding, and other flooding scenarios. Neutrino models friction and adhesion between solid/fluid boundaries and various adhesive hydrodynamic forces between fluid/fluid particles.
Hazard Module	The hazard module takes as input the logic tree and underlying data developed by a probabilistic hazard assessment (i.e., a PSHA model as described in the Hazard Input Document described in NUREG-2115 (NRC 2012a) and NUREG-2117 (NRC 2012b)). Directly incorporating the hazard model into the PRA software, rather than only handing off the final results, maintains the complete set of hazard model information, including the complete characterization of uncertainties, in a form that can be queried by EMRALD and RAVEN. The hazard module, which is in the planning stages of development, will sit within the EMRALD or

Advanced Tool	Capabilities
	RAVEN tool.
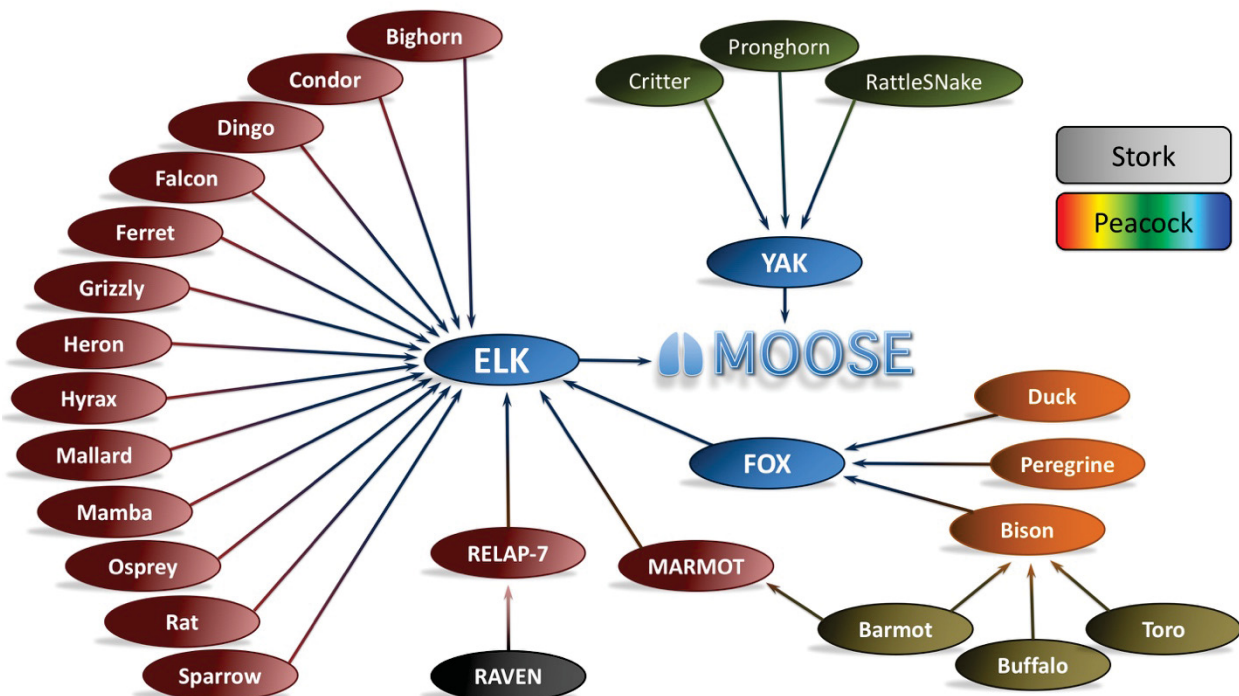
Figure 5.   Additional MOOSE resources and tools

2.2   External Hazard Applications

The RISMC toolkit ASPRA activity is developing a new set of tools and methods within the RISMC technical pathway to perform ASPRA. These tools and methods would be implemented within the MOOSE solver framework and would make use of existing and newly developed tools and methods, coupled with the experience and data gained in the past decades, to define and analyze more realistic risk assessment models.

The steps in ASPRA are shown the central box in Figure 1, along with their relationship to other RISMC elements. External event PRA is composed of three general elements: hazard assessment, fragility relationships, and systems analysis. SPRA also has the element of soil-structure-interaction analysis, which couples the rock hazard at the sites to the in-structure motions experienced by the systems and equipment within the NPP. The fragility of the structure itself is also important for assessment of the potential for early release into the environment. The new tools and approaches developed in this project cover the many steps in a SPRA in a more cohesive approach that could reduce interface issues and more accurately track uncertainties throughout the process. The methods developed would move away from the use of peak ground acceleration to incorporate parameters of most significance to response to earthquake ground motions. By tracking uncertainties more seamlessly and rigorously throughout the process, and using physics-based tools to investigate scenarios of interest that have traditionally been left out of SPRA (e.g., seismically-induced fire and flood), the new tools would provide more accurate models with a clearer view of uncertainties.

Development of a set of tools and methods to replace the existing SPRA is the first focus area of a multi-phase project. Focus area 2 would also develop new tools to seismically-induced flooding (internal and external). Focus area 2 feeds into the tools created in focus area one by developing methods and protocols to use various physics-based dynamic tools available in the RISMC toolkit to investigate issues and uncertainties in the systems model for facilities being analyzed. Activities following these first phase of activities would identify areas in which efficiencies are found and/or further developing methods based on ongoing use of the tools and methods.

Coupled with the development of the tools is an effort to perform verification and validation, which includes a program of small- to large-scale laboratory experiments (Coleman, Smith and Kammerer 2016). The development of the tools is also supported by a new cooperative multi-partner research consortium called the *Experimental Research Group – External Hazards* (ERG-EH) coordinated by INL (Coleman et al. 2016). The ERG-EH is being developed to obtain high quality, large-scale experimental data that can be used to validate RISMC tools and methods in a timely and cost-effective way. The ERG-EH includes recognized experts in the fields of seismic and flooding hazard assessment. The data developed by ERG-EH will be stored in databases for use within RISMC. These databases will be used to validate the advanced external hazard tools and methods.

3.   RISMC TOOLKIT DEVELOPMENT FOR EXTERNAL HAZARDS

Figure 4 shows the elements of the RISMC toolkit with application specifically for external events. The capability of the tools that make up the toolkit are described in Table 1 and the many MOOSE-based tools in Figure 5 are available. Continued development of three tools is of particular importance in meeting the needs of advanced external events PRA These tools, Mastodon, Neutrino, and EMRALD, are discussed in the remainder of this section.

3.1   The Mastodon Tool

Mastodon is a MOOSE based application that numerically models seismic soil-structure interaction for NPPs. It includes capabilities to simulate earthquake fault rupture, propagate the wave from the rupture site to the structure, and to estimate the response of a structure or nuclear facility and the soil around it to the resulting seismic wave. A brief description is provided in Table 1 and a description of ongoing Mastodon development is provided below. Development of the MOOSE-based Mastodon tool has been funded by both LDRD and LWRS. For clarity Table 2 provides specific capabilities being Mastodon under each funding source.

Table 2.   Modeling elements in Mastodon.

LDRD	LWRS
Point source earthquake fault rupture	Newmark Beta Time Integration
Stochastic Finite Elements (under development)	Hilber-Hughes-Taylor Time Integration
Absorbing Boundaries (Lysmer Dampers)	Nonlinear Soil Constitutive Model (Soil-HYS)
Domain Reduction Method	Soil-Foundation Interaction, Gapping and Sliding (Under Development)
	Dynamic Porous Media Flow in Soil Media

3.1.1   Earthquake Fault Rupture

Earthquakes originate due to the rupture of a fault segment. A fault rupture can be modeled using a series of point sources. Each point source takes the fault orientation, area of fault rupture and soil properties as input and generates a double couple. The methodology detailed in Chapter 4 of (Aki and Richards 2002) is used for modeling the point sources.

The formulation for releasing energy using a point source can be described by considering the orientation of an earthquake fault described using three directions (i.e., strike (ϕ_s), dip (δ) and slip direction (λ)), as shown in Figure 6.
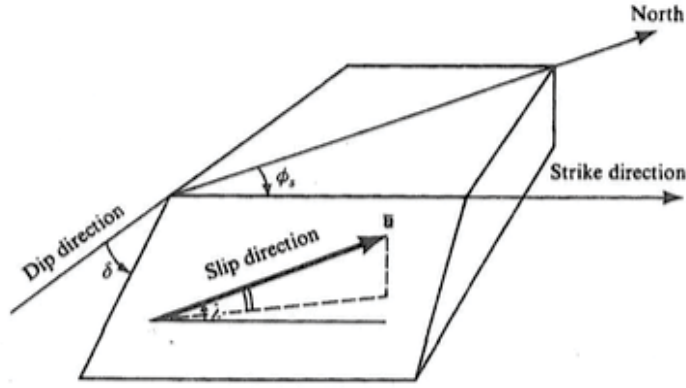
Note: The fault-orientation parameters (strike $\boldsymbol{\phi_s}$, dip $\boldsymbol{\delta}$) and slip-direction are measured clockwise around from north, with the fault dipping down to the right of the strike direction. $\boldsymbol{\delta}$ is measured down from the horizontal.

Figure 6.   Definition of the fault-orientation parameters (strike $\boldsymbol{\phi_s}$, dip $\boldsymbol{\delta}$) and slip-direction (from Aki and Richards 2012).

The seismic moment (M_o) of the earthquake point source in the above coordinate system is:

$$M_o(t) = \mu A \bar{u}(t)$$

where μ is the shear modulus of the soil, A is the area of fault rupture and $\bar{u}(t)$ is the spatially averaged slip rate of the fault.

When this seismic moment is converted into the global coordinate system (x, y and z) with the x direction along geographic north and z direction along soil depth, the resulting moment can be in written in a symmetric 3 x 3 matrix form whose components are as follows:

$$M_{xx}(t) = -M_o(t)(sin\delta \ cos\lambda \ sin2\phi_s + sin2\delta \ sin\lambda \ sin^2\phi_s)$$

$$M_{xy}(t) = M_o(t)\left(sin\delta \ cos\lambda \ cos2\phi_s + \frac{1}{2}sin2\delta \ sin\lambda \ sin2\phi_s\right) = M_{yx}(t)$$

$$M_{xz}(t) = -M_o(t)(cos\delta \ cos\lambda \ cos\phi_s + cos2\delta \ sin\lambda \ sin\phi_s) = M_{zx}(t)$$

$$M_{yy}(t) = M_o(t)(sin\delta \ cos\lambda \ sin2\phi_s - sin2\delta \ sin\lambda \ cos^2\phi_s)$$

$$M_{yz}(t) = -M_o(t)(cos\delta \ cos\lambda \ sin\phi_s - cos2\delta \ sin\lambda \ cos\phi_s) = M_{zy}(t)$$

$$M_{zz}(t) = M_o(t)sin2\delta \ sin\lambda$$

Each component of the above matrix is a force couple with the first index representing the force direction and the second index representing the direction in which the forces are separated (see Figure 7).
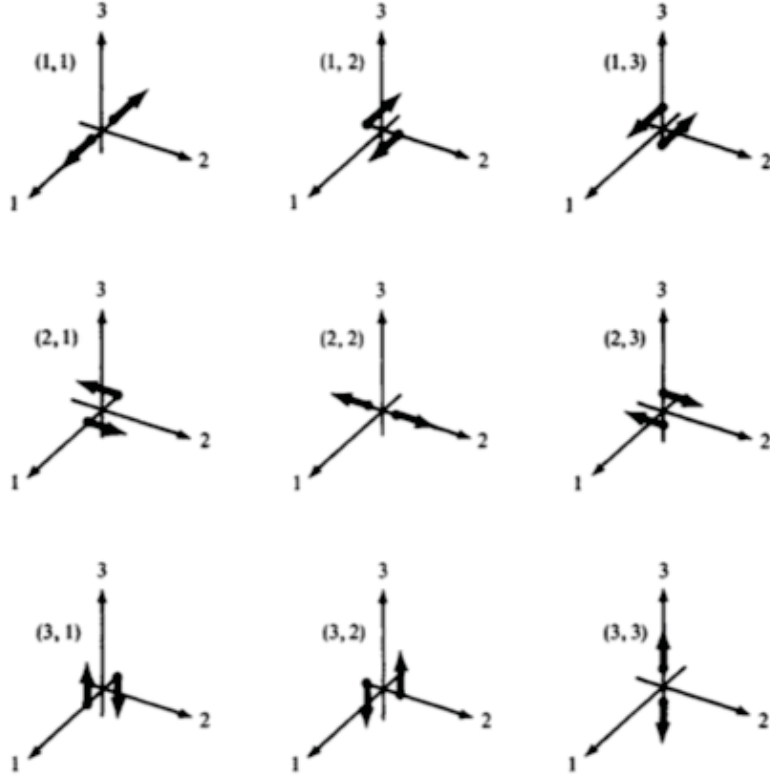
Note: The directions noted as 1, 2, and 3 refer to the global x, y and z directions, respectively.

Figure 7.   The nine different force couples that are required to model an earthquake point source (from Aki and Richards 2012).

The total force in each direction *i* resulting from this earthquake source applied at point $\vec{\xi}$ in space is then:

$$f_i(\vec{x}, t) = -\sum_{j=1}^{3} \frac{\partial M_{ij}(\vec{x}, t)}{\partial x_j} = -\sum_{j=1}^{3} M_{ij}(t) \frac{\partial \delta(\vec{x} - \vec{\xi})}{\partial x_j}$$

where $\delta(.)$ is the delta function in space.

Shown below is an example of an inclined fault rupture using 1600-point sources.
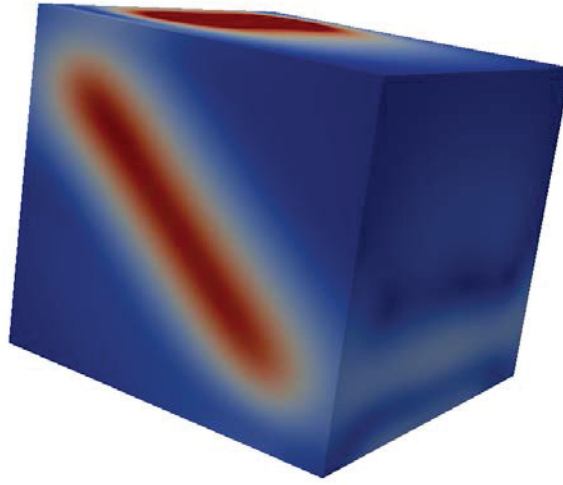
Note: The red region is where the fault rupture is triggered. The soil domain to the right of the fault moves up along the fault and the soil domain below the fault moves down along the fault.

Figure 8.   Inclined fault rupture generated using 1600-point sources along an inclined plane.

3.1.2   Wave Propagation in Soil

Once the earthquake fault ruptures, P (compressional) and S (shear) waves are generated and the propagation of these waves in a soil domain is governed by the wave equation:

$$c^2 \nabla^2 u = \frac{\partial^2 u}{\partial t^2}$$

Where u is the displacement variable, c is the velocity of wave propagation and ∇^2 is the spatial Laplacian operator. Finite element methods are used to discretize this governing equation of motion in space and Newmark-beta or Hilber-Hughes-Taylor time integration are used to solve the equation in time.

The following example problem is used to verify the ability of Mastodon to model simple wave propagation. Figure 9 shows an example problem with a linear elastic soil column that is 1 m x 1 m wide and 20 m deep. The Young's modulus of the soil is 50 MPa at the top and increases with depth to 325 MPa at the bottom. The top surface of the soil domain is free and the bottom surface is fixed in the y and z directions. An acceleration time history from the Chi-Chi earthquake is applied in the x direction to the bottom surface. Periodic boundary conditions have been used to force the left and right boundaries to move together and the front and back boundaries to move together. The propagation of the wave through the soil column is simulated using Mastodon. The acceleration response spectra at the top of the soil column, which provides information about the frequency content of the acceleration time history, is also shown in Figure 9. The results obtained from Mastodon are compared with that obtained from implicit and explicit versions of other commercial software such as LS-DYNA (LSTC 2013) and DEEPSOIL (Hashash et al. 2011). Figure 9 shows that the DEEPSOIL and Mastodon curves lie on top of one another,

there are slight differences in amplitude between the LS-DYNA results. This is due to an error in the LS-DYNA Rayleigh damping formulation. The results are considered to be within acceptable tolerances.
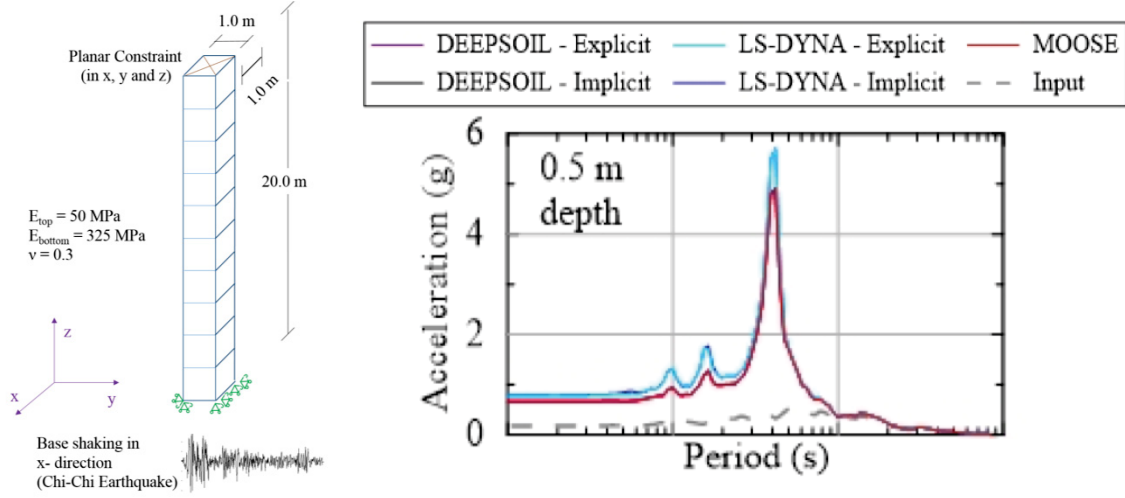
Figure 9. Schematic description of the linear elastic soil domain (left) and spectral acceleration at the top of the soil column obtained from Mastodon /MOOSE, LS-DYNA (implicit and explicit) and DEEPSOIL (implicit and explicit) (right).

The above analysis assumes the soil behavior is linear elastic. However, as the amplitude of the seismic wave increases, the soil behavior becomes nonlinear. To model this nonlinearity in the soil, a nonlinear soil constitutive model, termed Soil-HYS, has been implemented in Mastodon. This model belongs to the class of distributed element models (Iwan 1967) developed by Chiang and Beck (1994). The model captures the nonlinear hysteretic soil behavior using nested elasto-plastic surfaces and the model works for one, two and three-dimensional (1-D, 2-D and 3-D) wave propagation.

The distributed element model in 1-D can be schematically represented using a set of elastic-perfectly spring, s, as shown in Figure 10. Each spring has a Young's modulus (E_i) and a yield strength (σ_i) associated with it. If the total stress is less than the yield stress of all the springs, the material behaves like a linear elastic material. However, as the stress increases beyond the yield stress of a spring, that spring fails to provide any additional resistance, resulting in a reduction in the overall strength of the material. In the stress-strain space, this is same as dividing the experimentally obtained stress-strain curve into a set of linear elastic-plastic elements as shown in Figure 10. The total stress in the element is obtained as a summation of the stresses in each individual elastic-perfectly plastic element. Mastodon allows the user to define "n" number of nested surfaces. This allows the user to the flexibility to smooth out the stress-strain curve.
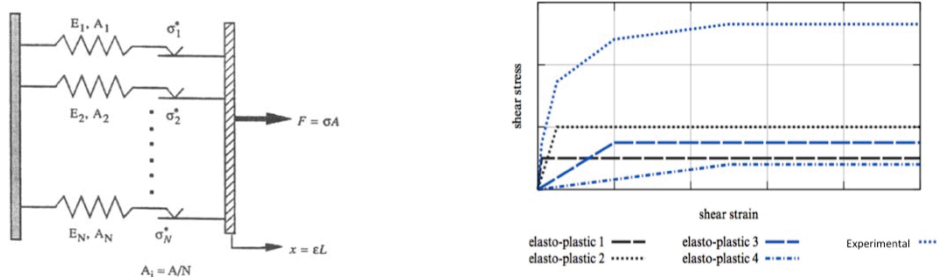
Figure 10. Schematic description (left) of the one-dimensional distributed element model (after Iwan 1967, Chiang and Beck 1994). Distributed element model (right) in the stress-strain space with the experimentally obtained stress-strain curve being divided into a set of elastic-perfectly plastic curves (LSTC 2013).

The three dimensional generalization of the model is achieved using von-Mises failure criteria for each elastic-perfectly plastic component. So, the yield surface is invariant in the 3D stress space for each component. However, when all the components are combined, the resulting yield surface looks similar to that of a material model with kinematic hardening. The hysteretic Masing behavior (Masing 1926) of this soil model can be seen in Figure 11.
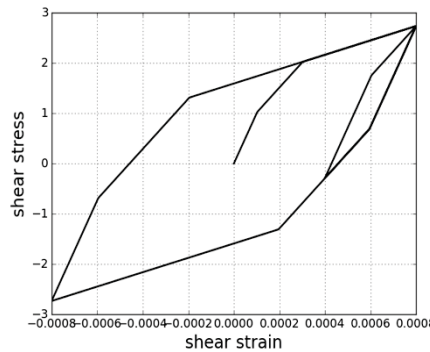
*Note: The unloading and reloading pattern shown
satisfies the Masing rules formulated for soils.*

Figure 11. Cyclic stress-strain behavior for the soil-HYS material model.

The backbone stress-strain curve required for this material model can either be provided by the user or be auto-generated using a set of empirical equations for commonly used soil types. These empirical equations are obtained from experiments conducted on soils. Darendeli (2001) and GQ/H (Groholski et al. 2015) backbone curves have been coded into Mastodon to auto-generate the stress-strain backbone curves.

The non-uniform shear beam example (Figure 9) was repeated using the soil-HYS material model with the backbone curve auto-generated using the GQ/H formulation. The acceleration response spectra obtained at the top of the soil column using Mastodon matches well with those obtained from implicit and explicit versions of LS-DYNA and DEEPSOIL (Figure 12).
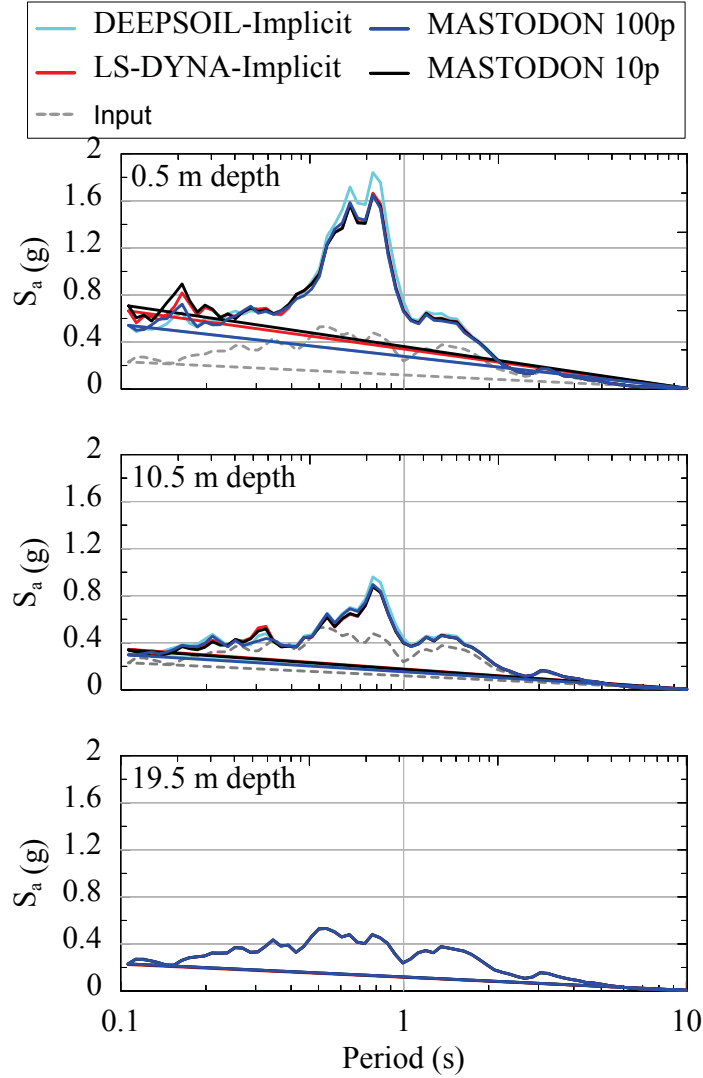
Note: The results obtained from Mastodon /MOOSE agree well with those obtained from LS-DYNA (implicit and explicit) and DEEPSOIL (implicit and explicit)

Figure 12.   The acceleration response spectra at the top of the soil column for a nonlinear non-uniform shear beam with 1-D vertically propagating shear wave.

In the above examples, the accelerations or displacements are prescribed (kinematic boundary conditions) at the bottom surface. This results in waves reflecting off the bottom boundary. In reality, soil domains are infinite. In order to model infinite soil domains, the kinematic boundary conditions have to be replaced with force/traction boundary conditions. Therefore, the seismic ground motion has to be transferred into a stress. For a 1-D wave propagating vertically in an infinite linear elastic soil domain, the stress at any location within the soil domain is given by:

$$\sigma = \rho V_p \dot{u}$$

Where σ is the stress, ρ is the density, $\dot{u}$ is the earthquake induced ground velocity and V_p is the P-wave velocity through the soil domain.

Another requirement for modeling wave propagation in infinite soil domains are non-reflecting or absorbing boundaries. In Mastodon, Lsymer dampers (Lysmer and Kuhlemeyer 1969) have been implemented to serve as absorbing boundaries. Lsymer dampers apply a stress at the truncated boundary. The magnitude of stress ($\sigma = \rho V_p \dot{u}$, where $\dot{u}$ is the particle velocity at that location) is calculated from 1-D wave propagation in a linear elastic infinite soil domain. So, if the soil domain is linear elastic and the waves are vertically incident on the truncated boundary, the Lysmer damper completely absorbs the incident wave. If the soil domain is nonlinear or if the waves are incident at an angle on the truncated boundary, then a small percentage of the waves are reflected back into the soil domain. However, placing Lysmer dampers sufficiently far from the region of interest and including other damping options such as Rayleigh damping or damping due to material nonlinearity can significantly reduce the effect of these reflected waves on the region of interest.

3.1.3   Soil-Structure Interaction

The next step is modeling the response of the soil-structure ensemble. Wave propagation in just soil or structure can be simulated using the techniques described in the preceding section. To model the response of the soil-structure ensemble, the contact between the structure and the soil needs to be modeled.

One option for modeling the soil-structure contact is by assuming a tied contact, i.e., assuming the structure and soil move together. This may not be realistic in most situations as the soil can be softer than the structure. The other option is to add a mechanical contact interface between the structure and the soil that accommodates relative movement (gapping and/or sliding) between the structure and the soil. In MOOSE/Mastodon, the mechanical contact is currently modeled using a kinematic formulation (stricter contact enforcement) in the normal direction and penalty formulation (flexible/soft contact) in the tangential direction. The robustness of this contact algorithm in simulating soil-structure interaction is yet to be explored.

Simulating soil-structure interaction problems with the soil domain extending from the source (earthquake fault rupture) till the structure for multiple structural parameters can be computational expensive. A computationally efficient Domain Reduction Method (Bielak et. al 2003) was implemented in Mastodon to overcome this issue. In this method, the problem is divided into two parts: (1) a linear elastic infinite soil domain with the earthquake fault rupture is simulated first to obtain the free field response of the soil, and (2) the structure and a small region of the soil around it is simulated next with input from the free-field response. The soil and structure material nonlinearity, gapping and sliding, and other nonlinear effects can be modeled in the second part of the problem. The advantage of this method is that only the second part of the problem needs to be re-run if the structural parameters are altered.

The domain reduction method and the wave propagation capabilities have been used to simulate the response of a nuclear containment building and the reactor pressure vessel to earthquake ground motion from an inclined fault rupture. In this scenario, the soil and structure are made of linear elastic material and the soil and the structure always move together (tied contact). This response of the pressure vessel was coupled with a fuel rod model created in BISON to simulate the thermal and mechanical response of the fuel rod when a scram is triggered due to the earthquake. See Figure 13 for a screenshot of the simulation.

Note: The image to the left shows the soil domain with the inclined earthquake.
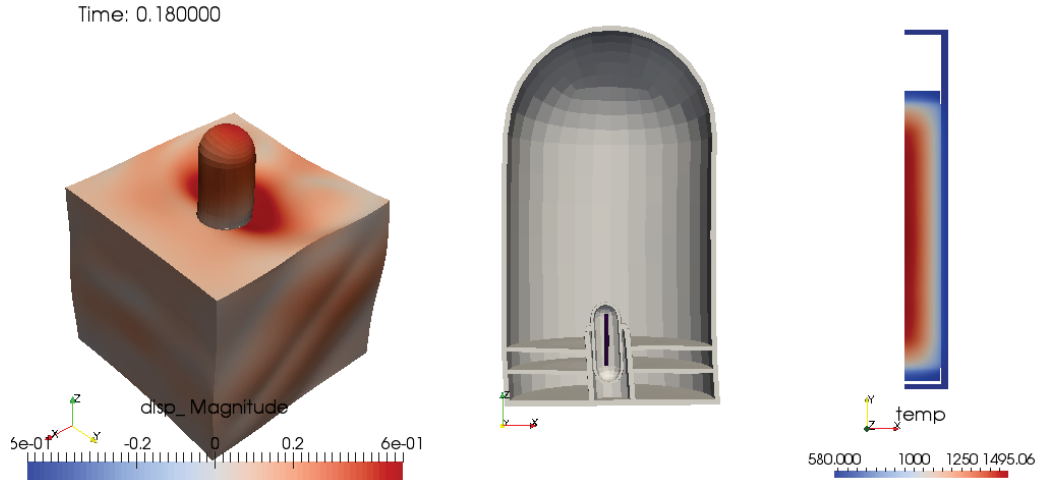
Figure 13.   Graphical representation of a coupled Mastodon/BISON simulation.

3.1.4   Stochastic Methods

There are many uncertainties when it comes to modeling response of soils to earthquake excitation. Variability in soil properties can be fit with a probability distribution. When one value is chosen for a soil parameter, only one realization of the problem is simulated. Stochastic methods have to be employed to evaluate the effect of the uncertainty in the input (soil parameters) on the final quantity of interest (say acceleration at a location inside the reactor). Two ways to accomplish this are:

- Monte-Carlo: A commonly used calculation. In this technique, multiple realizations of the problem are simulated and the output is obtained for each realization. This output from the multiple realizations can then be combined to obtain the probability density function, which characterizes the uncertainty in the output. Currently, RAVEN and Mastodon are being coupled to add this capability of automatically simulating multiple realizations of the problem to obtain uncertainty in the output.

- Stochastic finite element method: Used in other computation applications but new to seismic simulations in soils. Another method of estimating the uncertainty in the output is by introducing this quantity as a variable into the problem. In this method, the output uncertainty is automatically calculated by running just one simulation instead of the multiple simulations required in Monte-Carlo method. Efforts are underway to add this capability into Mastodon.

3.2   The Neutrino Tool

In order to simulate flooding events, a semi dynamic model, capable of adjusting parameters for an event, must be used. The format or content of this model is dependent upon the tool that is used to simulate the flooding event. Most simulation packages can import rigid body structures using many common formats. However, currently there is no standard toolset of capabilities needed to simulate real world scenarios and thus no common format can be used for adjusting parameters of the various simulation software packages.

3.2.1   Smooth Particle Hydrodynamics

Some recent development work on Neutrino provides an advanced tool set and capabilities needed for this task and to simulate other real world scenarios. The Neutrino software uses an IISPH solve engine which is faster than many similar tools, and still acceptably accurate for a flooding scenario. An advanced "Z Sorted Compact Hashing" method is used to accomplish quick nearest neighbor lookup when computing particle interactions (Sampath 2016).
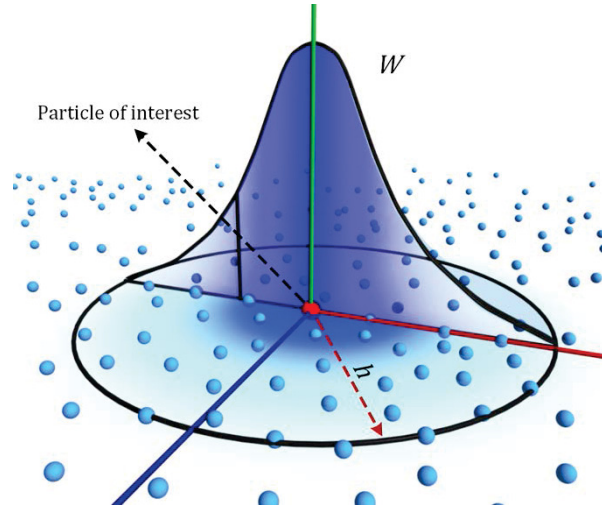
Note: W denotes a Gaussian-like shape kernel function and h is the support radius.

Figure 14.   Illustration of the smooth particle hydrodynamics interpolation.

3.2.2   Neutrino Capabilities

An advanced graphical user interface (GUI) for Neutrino makes it easy to visualize the model being worked on. The general practice is to import existing rigid body models and then add the dynamic components for the simulation. However, the GUI also allows creation of some rigid body items. A left side list has a scene inspector and shows the properties of selected items. The left tool bar also allows for easy movement of scene items. A bottom time bar allows for manual simulation of the scenario with real-time viewing of the in the main screen. See Figure 15.

Neutrino allows for different types of particle emitters attached to the solve engine. A flow rate particle emitter can be used to simulate water flow through a penetration or a pipe break with a specified location, orientation, and flow rate. A Toricelli emitter creates particles to match a given rainfall rate, surface area, and opening. A teleport emitter can move particles from one level to another simulating the flow through a pipe. Dike failure can event be simulated by a variable size and flow emitter and matching it to and erosion model. Other emitter options and validation tests are in development.

Measurement fields can be added to a model in order to determine contact, height, or force of dynamic particles on a given object. These measurement fields can be tied to events of concern needed outside the simulation. The measurement fields are shown by a bounding box around a component (see Figure 16).
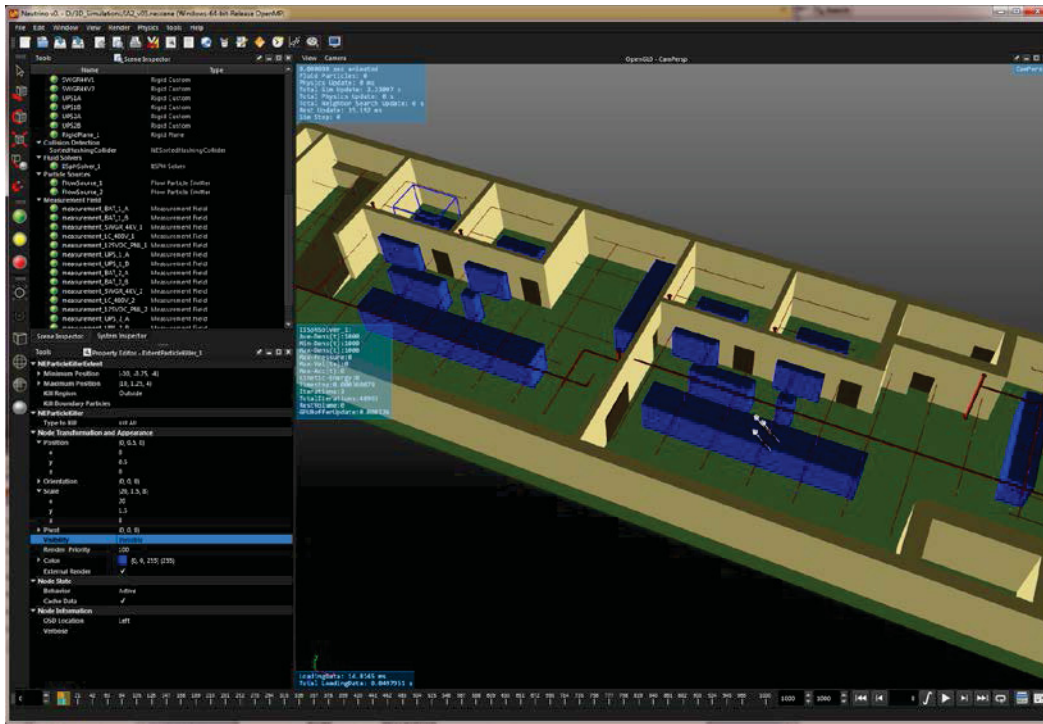
Figure 15.   User Interface for Neutrino and the IA2 switchgear rooms.

Another necessary feature is the dynamic communication with and external application through a port connection. Key simulation setup options and all item properties are adjustable though this network communication. For example, particle emitter flow rates, position, and direction can be set before a simulation and then changed during the simulation. Simulation start, pause, stop, reset, and end time options can also be set. Events from the measurement fields are also sent back to the connected application. All of this this allows for two way coupling between the 3-D simulation and an external tool such as the dynamic PRA tool EMRALD.
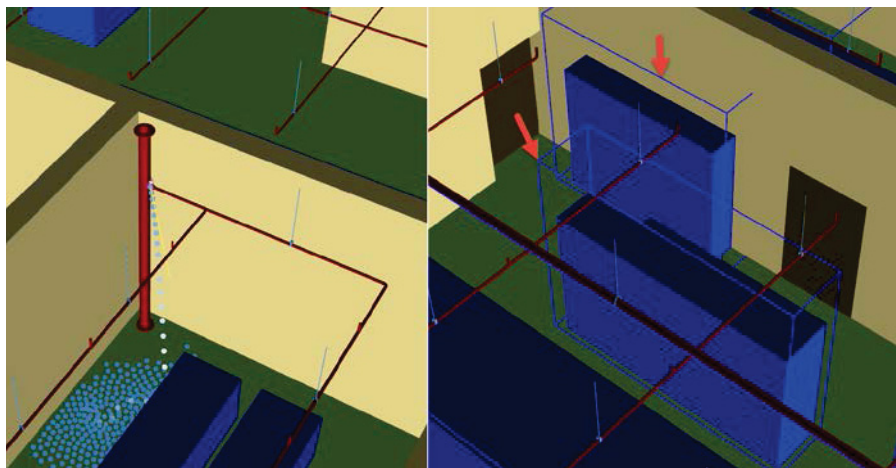
Figure 16.   Neutrino tools including variable flow particle emitter (left) and measurement fields (right).

3.3   The EMRALD Tool

EMRALD, is a dynamic PRA code based on three-phased discrete event simulation. These phases include the following:

0. Setup – Add initial start states.
1. If sifted to a new state do the following, else go to step 2.
    a. If terminal state, then quit.
    b. Execute the state's immediate actions.
    c. Process the state's event actions by adding conditional events to the lookup list or calculating the next occurrence of a probabilistic item and add it to the next event queue.
2. Execute any conditional events that have their criteria met, go to step 1 if any states changed.
3. Jump to the next event in the chronological event queue and process the events actions. Then go to step 1.

A model for EMRALD consists of States with immediate actions, and conditional event actions. Many different types of events and actions can be evaluated or executed, designed in a way for easy equivalents to items in traditional PRA such as basic events and fault trees. States can also be tagged as "key states" and are noted if a simulation run ends on that state. Through multiple runs of the simulation model, probabilities of each key state are derived, these are similar to end states results in SAPHIRE. In addition, heuristics can be made to show the path or cause of the key state and the times of those events. A traditional PRA model can be converted into an equivalent EMRALD model with statistically equivalent results.

In addition to the dynamic PRA, EMRALD is being used to couple the PRA with the piping failure analysis, the flooding simulation, and the RELAP5-3D simulations for this demonstration. Because it is time based, it can be coupled with other time based simulation methods. User defined and other specialized events and actions allow it to input and select defined piping failures, read component failures from NEUTRINO, and run RELAP5-3D then retrieve its results; using the data from the various tools to determine a final answer. See section 4 of INL-EXT-16-39353 for more details on EMRALD calling other analysis methods.
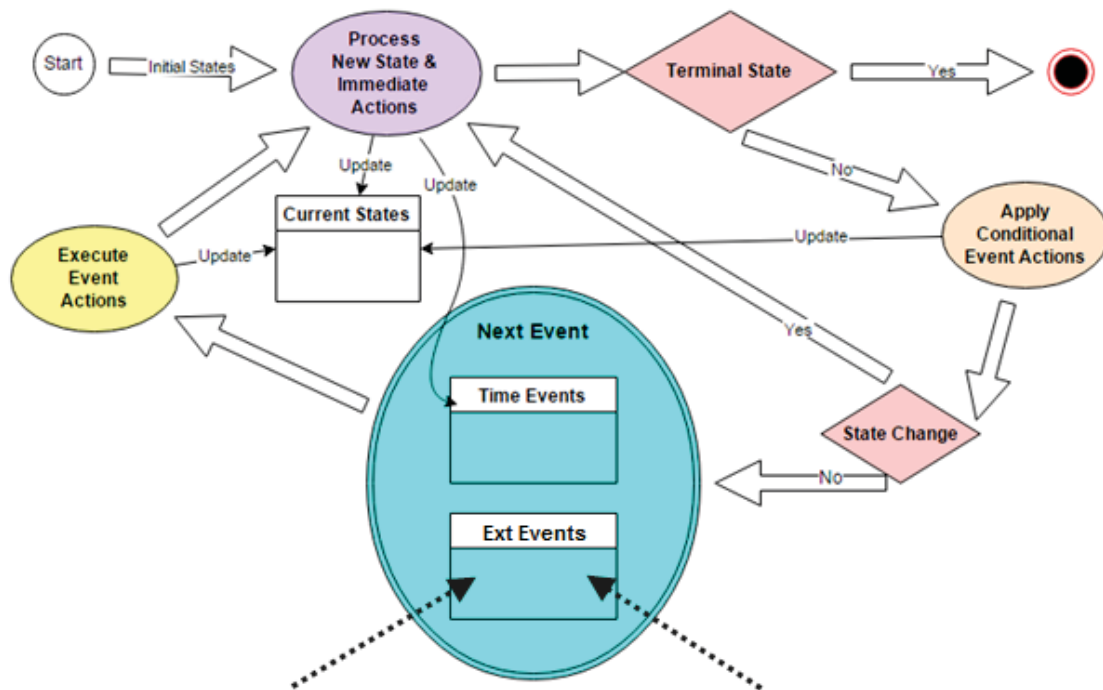
Figure 17. Flow diagram for processing an EMRALD Model.
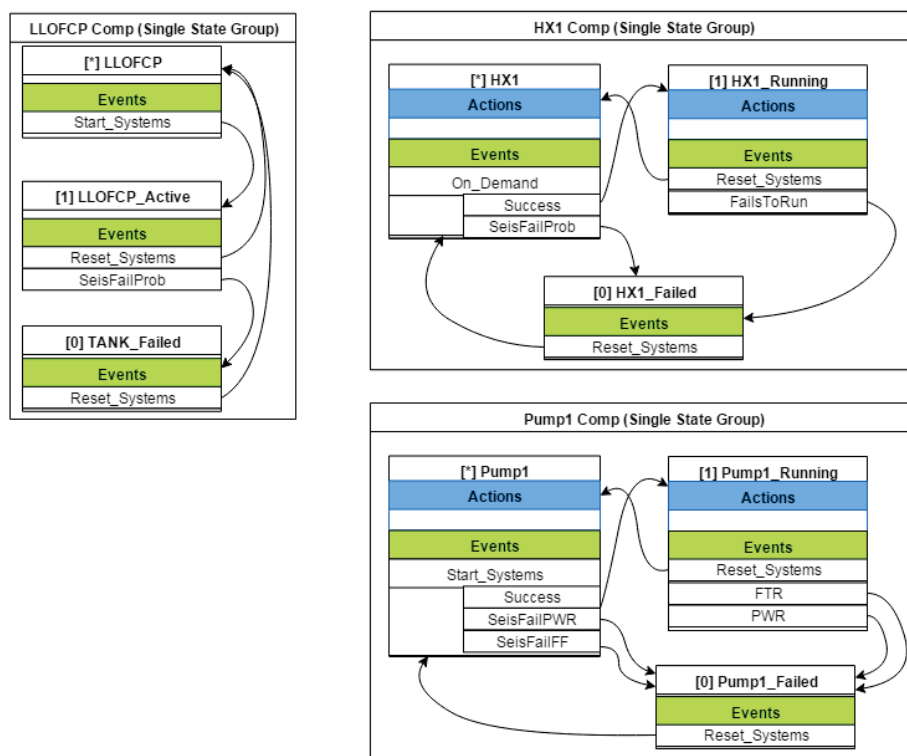
Figure 18. Example of EMRALD state diagrams for several components and their state changes.

4.   EXTERNAL HAZARDS ADVANCED PROBABILISTIC RISK ASSESSMENT DEMONSTRATIONS

4.1   Advanced Seismic Probabilistic Risk Assessment with Nonlinear Soil-Structure-Interaction Analysis

4.1.1   Background on Advanced Seismic Probabilistic Risk Assessment

As the understanding of local seismology at a nuclear facility site evolves, it often leads to updated site-specific seismic hazard estimates. These updates may result as improvements are made to seismic source characterization, ground motion prediction equations, and local site effects. As the seismic hazard changes, more intense input ground motions may be needed to numerically evaluate realistic nuclear facility response. Higher input ground motions result in larger soil strains, increased potential for gapping and sliding between the structure and soil, and larger in-structure responses. Therefore, as the intensity of ground motions increases, the importance of appropriately capturing nonlinear effects in numerical soil-structure-interaction (SSI) models increases.

The goal of this study is to compare the seismic structural fragilities obtained by a traditional NPP SPRA and an ASPRA that utilizes NLSSI analysis. Soil-structure interaction analysis in traditional SPRA ignores the geometric properties (soil and structure are glued together, namely, the soil undergoes tension when structure uplifts), and using linear soil properties and linear structure properties. The NLSSI analysis of this study will consider geometric nonlinearities, namely, gapping and sliding of the foundation.

The focus of the research task presented herein is integrating NLSSI into SPRA to improve the accuracy of in-structure response spectra (ISRS) and, in some cases, the impact to the structure itself. The specific nonlinear behavior included in the NLSSI calculation presented in this report is gapping and sliding. Other NLSSI effects are not included in the calculation. The commercial software program, LS-DYNA, is used for the NLSSI analyses.

4.1.1.1   Representative Soil Site and Nuclear Power Plant Structure

This study uses a soil profile representing basalt located under INL facilities. The soil properties listed in Table 3 are considered to be uniform with depth. The representative NPP structure used in the analysis is a pressurized water reactor building. It consists of a pre-stressed concrete containment structure and a reinforced concrete internal structure. The numerical model of this structure is obtained from the SASSI2000 user manual. The numerical models of both the containment and internal structures are idealized stick models illustrated in the left panel of Figure 19.

Median values of lumped masses and section properties of the stick models are presented in the right panel of Figure 19. These lumped masses include the masses of the stick elements apart from the masses of the non-structural components at each level. Therefore, a zero mass density is assigned for the concrete material in the internal and containment structures. A median elastic modulus of 6.9×10^5 ksf and a median shear modulus of 2.7×10^5 ksf are assumed for the concrete material. However, the concrete modulus of the internal structure is reduced by a factor of 0.5 to obtain a fundamental frequency near the peak of the uniform hazard spectrum (UHS), which amplifies the structural response. The CLASSI (Luco and Wong 1980) model of the representative NPP structure is identical to this SASSI2000 model.

Table 3.   Soil properties used in soil-structure-interaction model.

Property	Median	Lognormal Standard Deviation
Unit weight	159 lb/ft^3	-
Poisson's ratio	0.35	-
Shear-wave velocity	3720 ft/sec	0.27
Shear modulus	68,320 kip/ft^2	0.55
Damping	2%	0.4

Joint Properties			Member Properties			
Mass No.	M_{lg} (kips)		Location between Joint No.	Area (ft^2)	Shear Area (ft^2)	Moment of Inertia x 10^{-6} (ft^4)
base	20000	C				
1	46000	O	base to 1	1400	700	2.8
3	4200	N	1 to 2	1400	700	2.8
4	4200	T	3 to 4	1400	700	2.8
5	4200	A	4 to 5	1400	700	2.8
6	4200	I	5 to 6	1400	700	2.8
7	4610	N	6 to 7	1400	700	2.8
8	3020	M	7 to 8	990	500	1.9
9	2470	E	8 to 9	990	500	1.5
10	2120	N	9 to 10	990	500	0.8
11	190	T	10 to 11	990	500	0.2
12	2800	I	base to 12	2000	1320	1.1
13	2510	N	12 to 13	2560	1560	1.2
14	6290	T	13 to 14	2210	1460	1.2
15	3760	E	14 to 15	1960	730	1.3
16	8540	R	15 to 16	1740	600	0.9
17	1220	N	16 to 17	780	360	0.2
18	820	A	17 to 18	190	70	0.004

Figure 19.   Illustration of the representative nuclear power plant structures and the corresponding stick models (left) and section properties and lumped masses of the stick model (right) (from Ostadan 2006).

Table 4. Frequencies and percentages of total mass participation of significant modes.

Mode	Frequency (cycles/sec)	Mass participation (% of total)			Description
		UX	UY	UZ	
1, 2	5.27	45.6%	45.6%		1st horizontal mode for containment
3, 4	8.46	9.2%	9.2%		1st horizontal mode for internals
5, 6	12.37	20.4%	20.4%		2nd horizontal mode for internals
7	15.64			50.7%	1st vertical mode for containment
8, 9	16.24	9.4%	9.4%		2nd horizontal mode for containment
10	27.83			32.4%	1st vertical mode for internals
13, 14	32.89	7.9%	7.9%		3rd horizontal mode for internals

4.1.1.2 Seismic Hazard and Input Ground Motions

The earthquake ground motion is based on the seismic hazard for an existing NPP. Figure 20 shows the seismic hazard curve expressed in terms of the horizontal peak ground acceleration (PGA) and associated mean annual frequency of exceedance (MAFE). The reference earthquake for the traditional SPRA seismic fragility evaluation is nominally defined as the UHS at a horizontal PGA of 0.4g. This PGA corresponds to a MAFE of 1.0E-04. Figure 21 shows these 5% damped horizontal and vertical Reference Earthquake UHS. As a simplification for this study, the shape of the UHS is considered to be invariant with MAFE. This study uses a suite of thirty sets of earthquake ground motion time histories compatible with the Reference Earthquake UHS. The horizontal acceleration histories account for variability of the spectral acceleration in any arbitrary direction about the geometric mean of the two horizontal components. Figure 22 to Figure 24 show the 5% damped response spectra for the horizontal and vertical time histories and the target mean 1.0E-04 UHS.

INL performed a number of NLSSI analyses at multiple ground motion levels, expected to range from 3 to 5. Each ground motion intensity level is defined by a PGA, since the UHS shapes are assumed to be constant. The reference ground motion sets are scaled to generate multiple suites using the ratios of the ground motion level PGAs to the reference earthquake PGA.
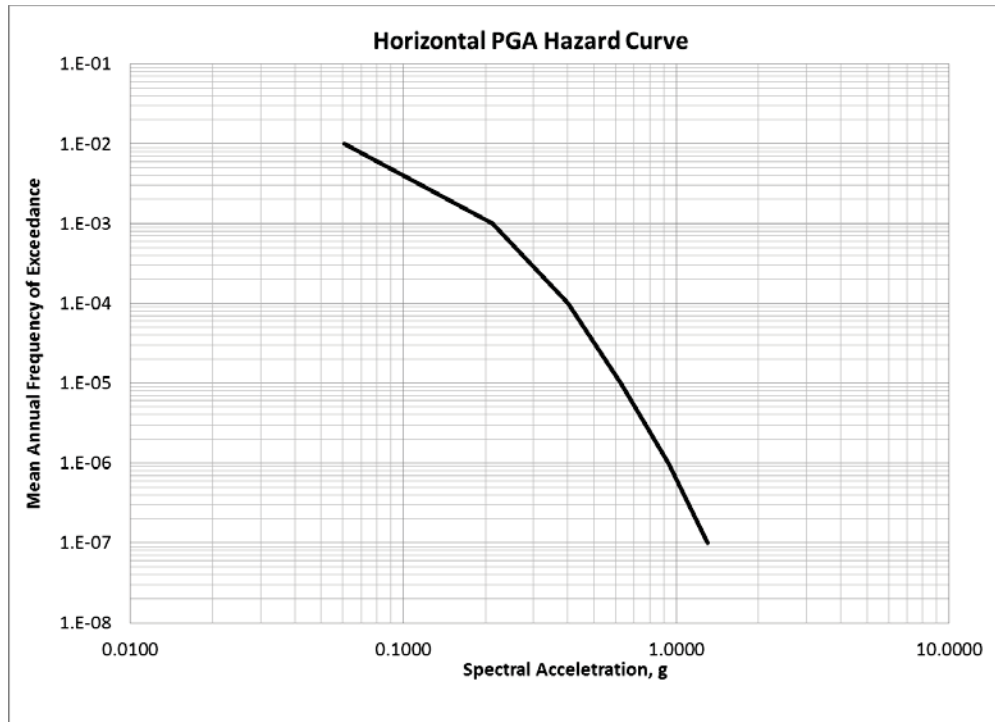
Figure 20.   Seismic hazard curve for horizontal peak ground acceleration.
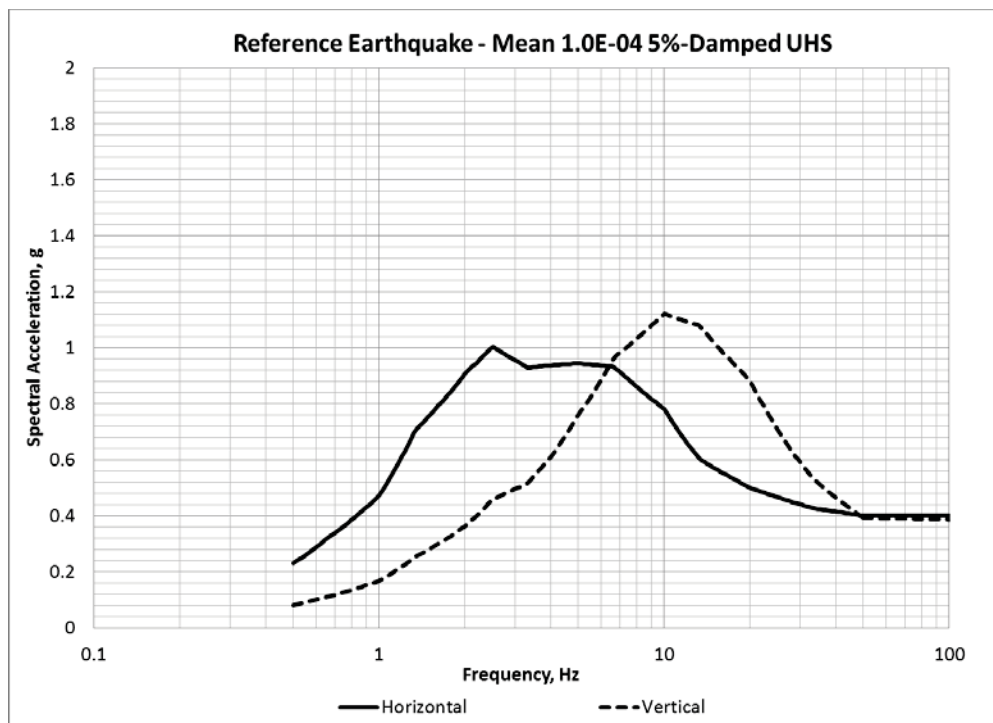
Figure 21.   Uniform hazard spectrum for mean annual frequency of exceedance of 1.0E-04.
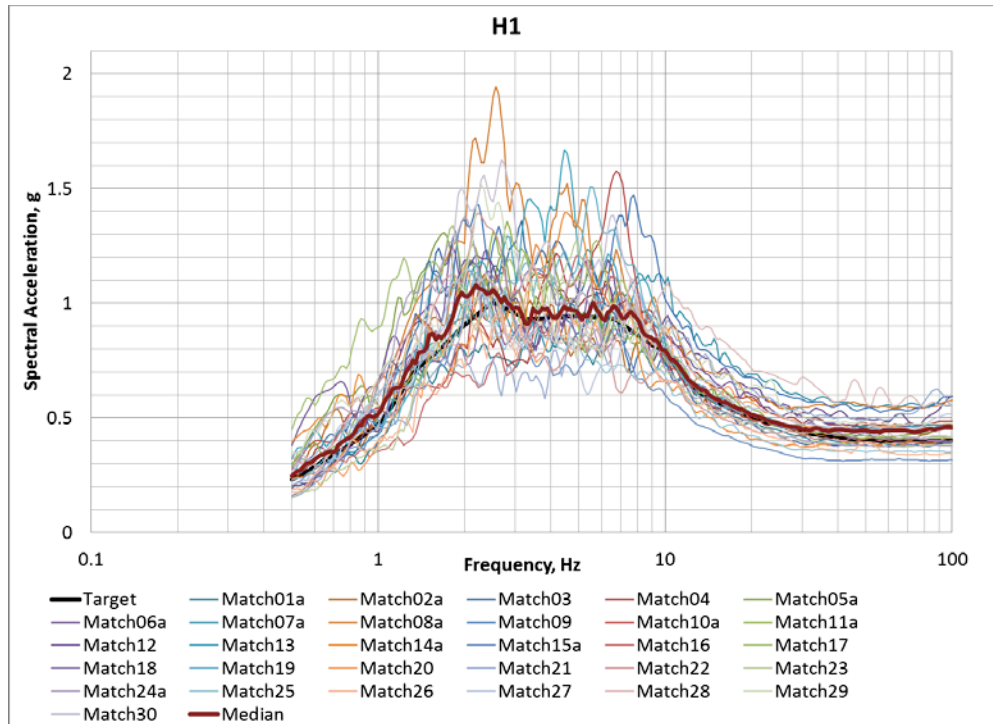
Figure 22. Response spectra (5% damping) for reference input ground motions (horizontal component H1).
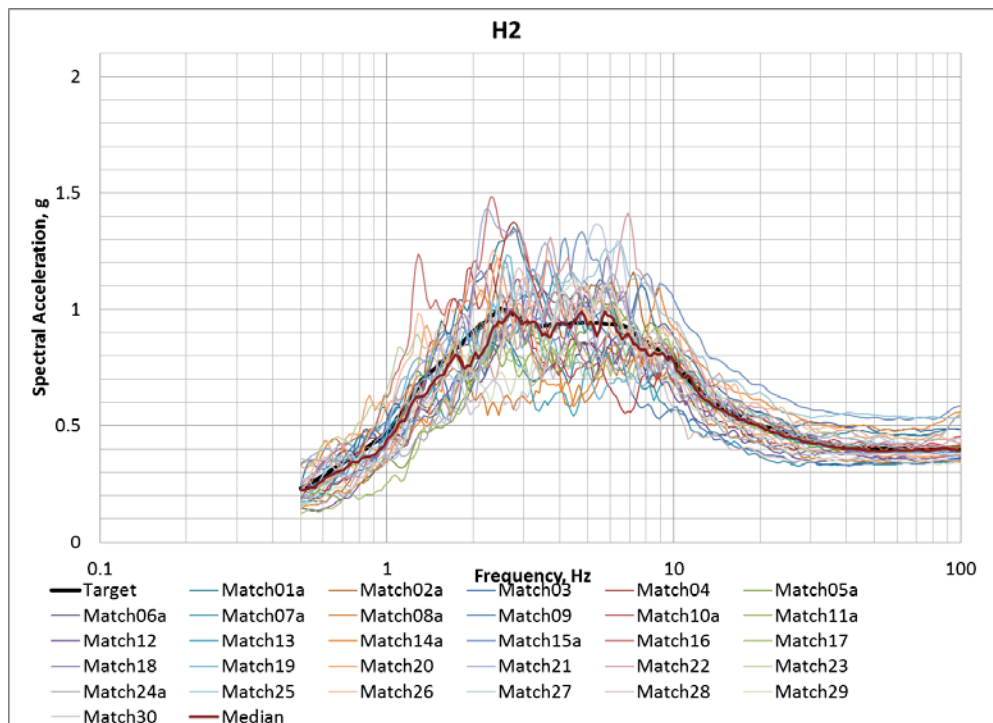
Figure 23. Response spectra (5% damping) for reference input ground motions at (horizontal component H2).
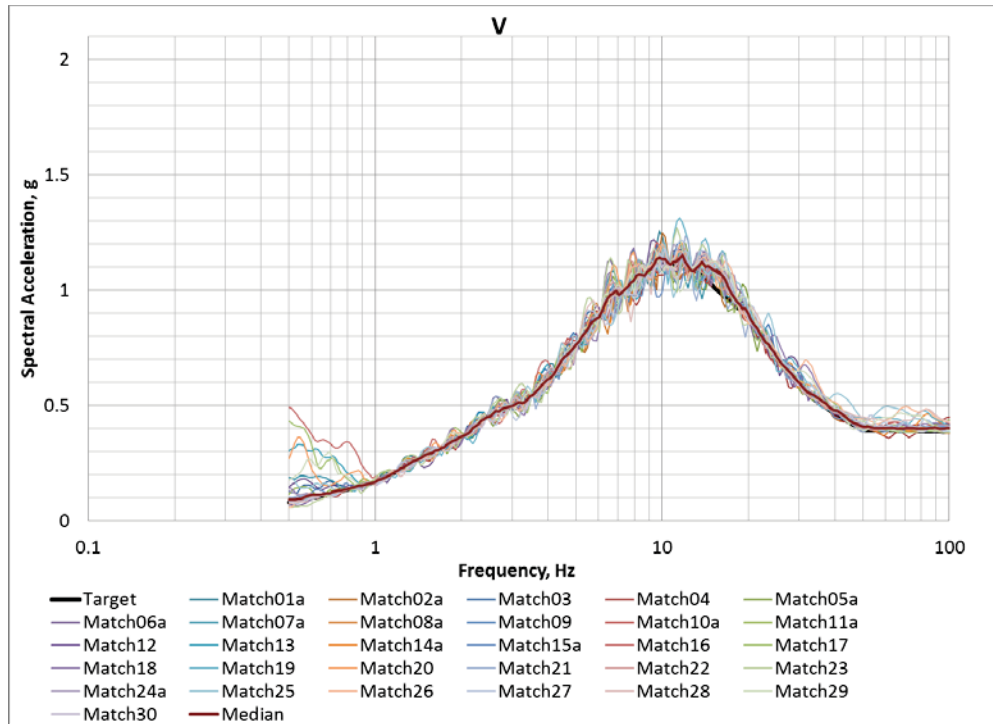
Figure 24. Response spectra (5% damping) for reference input ground motions (vertical component V).

4.1.1.3 Plant System Considered for Risk Assessment

4.1.1.3.1 Equipment Components

The plant system of interest is the Emergency Cooling Pump at the Advanced Test Reactor (ATR) at INL. This pump has an electric motor that is powered by Battery. The motor is started by associated control logic. The system consists of the following components:

- Emergency Cooling Pump (Figure 25)
- Battery (Figure 26)
- Distribution Panel (Figure 27); Circuit Breakers
- Medium Voltage Switchgear (Figure 28 shows similar switchgear with breakers removed); Primary Pump Relay

The actual system at ATR also includes Low Voltage Switchgear and Relay, Medium Voltage Switchgear and Primary Pump Relay, and Flow Indicator Switch. These components are excluded from the system model for this study for simplicity. The Concrete Block Wall is a seismic interaction hazard to Distribution Panel. The plant system components are all located on the internal structure. Battery and Medium Voltage Switchgear are located at Elevation 22ft. The remaining system components are located at Elevation 61ft.

4.1.1.3.2 System Logic Model

Panels a, b and c of Figure 29 show the progressive layers of single-top fault trees for the selected plant system. Figure 30 shows the event tree for one earthquake event or intensity level (PDS refers to Plant Damage State). Collapse of Concrete Block Wall will damage Distribution Panel. A sensitivity

study will be performed to understand its effect on the plant system risk. The seismic core damage frequency (CDF) was calculated both with and without the block wall.
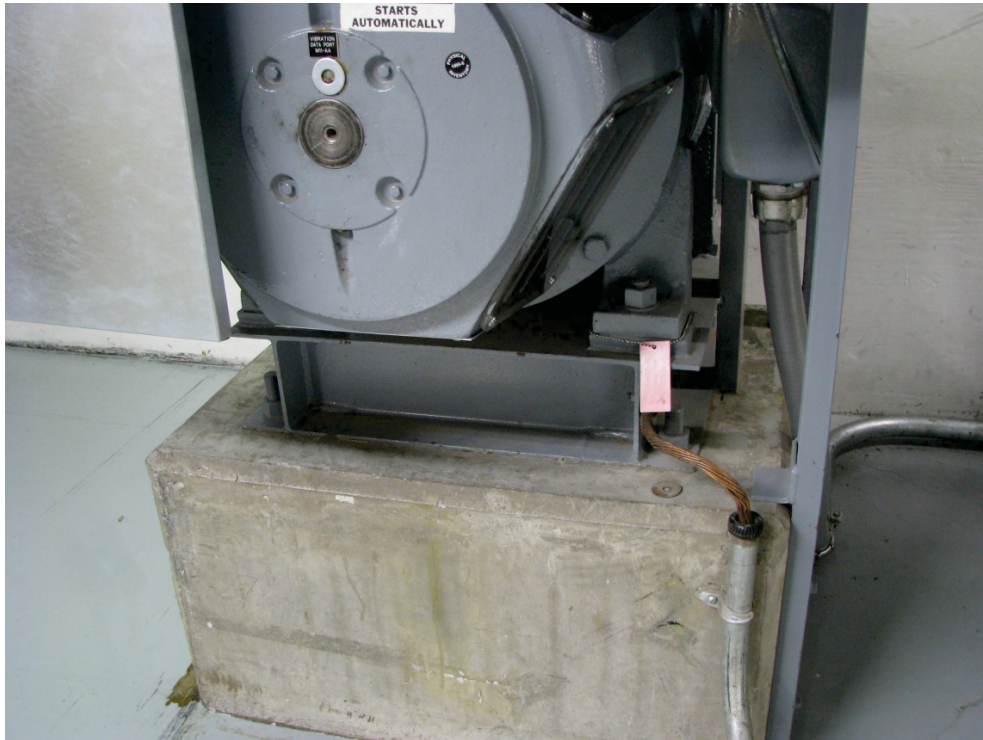
Figure 25.   Photograph of emergency cooling pump.

Figure 26.   Photograph of battery rack.

Figure 27.   Photograph of distribution panel.

Figure 28.   Photograph of medium voltage switchgear.

(a)

(b)

(c)
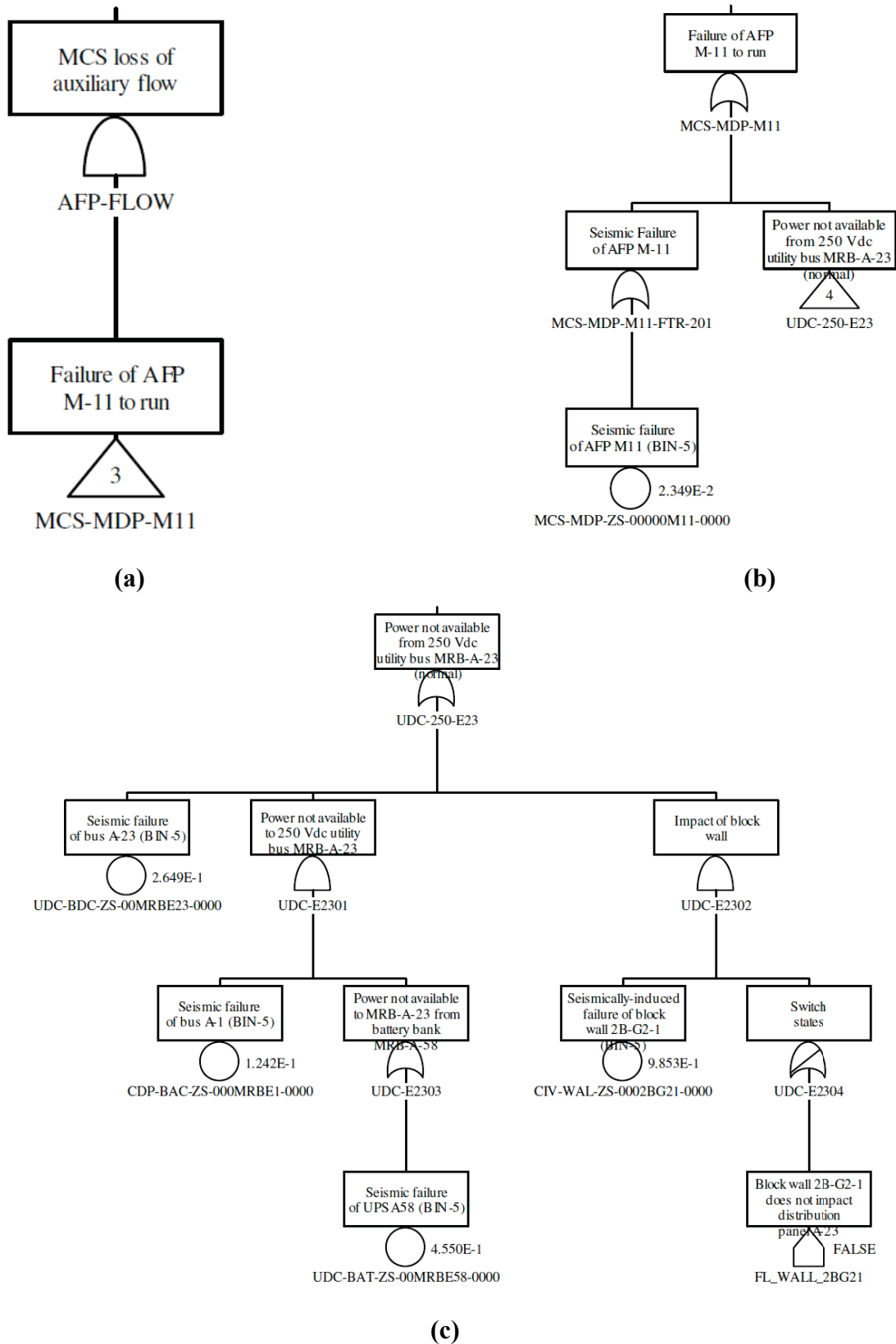
Figure 29. Demonstration problem system fault trees.
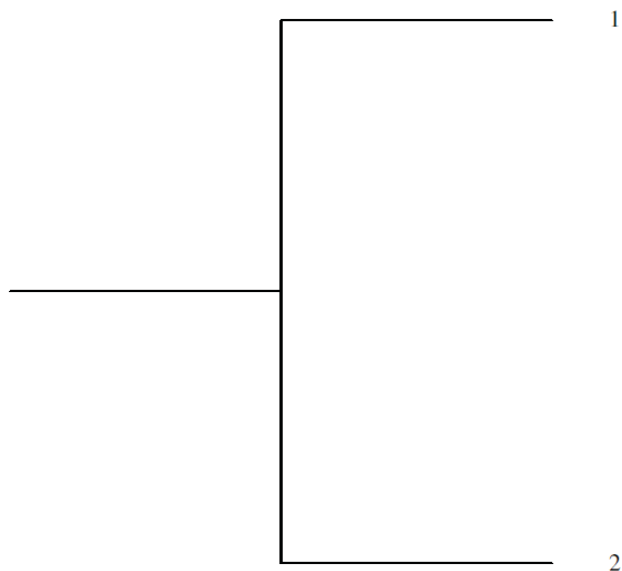
Seismic event occurs BIN-1	MCS loss of auxiliary flow		
IE-EQ-BIN-01	AFP-FLOW	#	END-STATE-NAMES

		1	OK
		2	PDS1

EQ-BIN-01 - 2015/01/22 Page 1

Figure 30. Demonstration problem event tree.

4.1.2 Traditional Seismic Probabilistic Risk Assessment

4.1.2.1 Probabilistic Seismic Response Assessment

We performed a probabilistic seismic response analysis of the representative NPP structure using methods typically implemented in a traditional SPRA. Probability distributions for ISRS at the locations of components of the selected plant system were generated. The analysis consisted of the following steps:

1. Ground motion input consisted of thirty sets of acceleration time histories.

2. The fixed-base Eigen solution and mass matrix were generated for the structure model with median properties using computer program SAP2000 (CSI 2011).

3. Foundation impedances for the median soil profile under the structure were generated using computer program CLASSI.

4. Probability distributions of the structure frequency, structure damping, soil stiffness, and soil material damping were represented by scale factors with median values of 1.0 and associated lognormal standard deviations. Representative lognormal standard deviations for structure frequency and damping of 0.15 and 0.35, respectively, were used. Lognormal standard deviations for soil shear modulus and damping of 0.55 and 0.4 were used (Table 5).

49

5. Probabilistic response analysis was performed by the Latin Hypercube Sampling approach for thirty simulations using computer program CLASSI. Stratified sampling was used to sample each of the scale factors representing the probability distributions for the variables considered (i.e., structure frequency and damping, soil stiffness and damping, earthquake acceleration time histories). Latin Hypercube experimental design was used to create the combinations of samples for the simulations.

6. Five percent damped median and 84% non-exceedance probability (NEP) ISRS were generated at the component locations. Three and a half percent damped median ISRS were also generated for use in the seismic fragility evaluations.

Table 5 lists the randomized property multiplier sets applied to the 30 computer models of the structure and soil. Figure 31 to Figure 33 show the median and 84% NEP ISRS at Elevation 22 ft in the X, Y, and Z directions for 5% damping. Figure 34 to Figure 36 show the median and 84% NEP ISRS at Elevation 61ft. Median and 84% NEP ISRS for 3.5% damping were also generated.

Table 5. Property randomization multipliers.

Model Number	Structure Frequency	Structure Damping	Soil Shear Modulus	Soil Damping	Soil-Foundation Coefficient of Friction[*]
1	0.9935	0.6741	1.0412	0.9213	0.75183
2	1.1629	1.5178	1.7367	0.5008	1.15056
3	1.0086	1.0574	1.6487	0.5621	1.01461
4	1.0244	0.5591	0.8781	1.1468	0.94767
5	0.9621	1.1275	0.8498	1.2324	0.87831
6	1.0601	0.4980	1.4524	0.6332	0.82448
7	1.2131	1.3758	1.1158	0.8500	0.84219
8	1.0730	0.9197	0.7247	1.4866	1.03097
9	0.8753	0.7066	1.0092	0.9651	1.17557
10	0.7446	1.3991	0.9720	1.0116	1.24079
11	1.0459	0.7308	2.0275	0.4317	1.13513
12	0.7734	2.2867	0.6451	1.7220	1.09008
13	0.8513	1.0819	1.3094	0.7189	1.2214
14	0.9399	1.2268	1.2243	0.7703	0.87656
15	0.9642	0.9893	0.8116	1.2879	0.92867
16	1.1905	1.3174	0.4520	4.2334	1.46668
17	0.9016	0.7988	1.0889	0.9035	0.80192
18	1.1399	1.7135	1.1820	0.8159	0.72579
19	0.8303	0.9575	0.6308	1.8682	1.35189
20	0.8856	1.1062	0.7680	1.4007	0.78486
21	0.9348	0.8889	0.9220	1.1124	0.91507

Model Number	Structure Frequency	Structure Damping	Soil Shear Modulus	Soil Damping	Soil-Foundation Coefficient of Friction[*]
22	0.9808	0.9059	1.3733	0.6686	0.99601
23	1.3215	1.6053	0.9365	1.0518	1.73369
24	1.0912	0.6113	0.6938	1.5944	0.5867
25	1.0369	1.1834	3.1721	0.3706	0.68318
26	1.2974	0.7767	0.5751	1.9937	1.31785
27	0.9202	0.8611	1.2611	0.7468	1.04394
28	1.1298	1.2376	0.7917	1.3364	0.96151
29	0.8165	0.8198	1.5447	0.5781	1.06556
30	1.1065	1.0263	0.5107	2.4194	1.41234

* Used in the NLSSI simulations; not used in linear SSI analysis
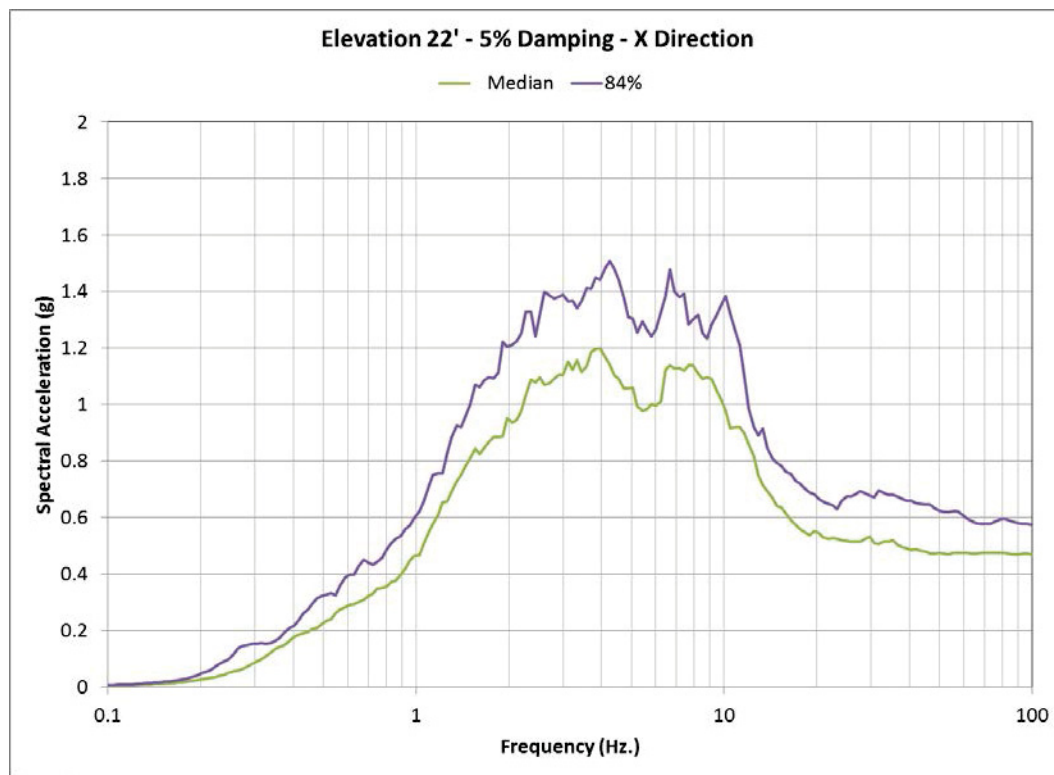
Figure 31.   Elevation 22ft, X-Direction Response Spectra, 5% Damping.
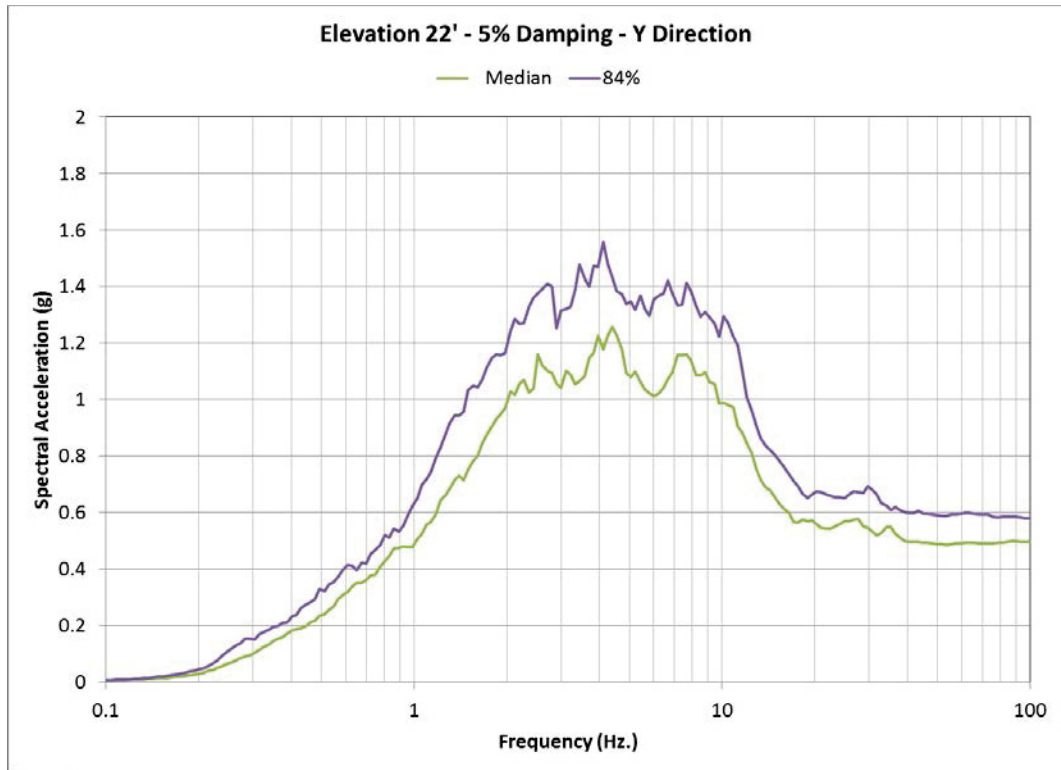
Figure 32.   Elevation 22ft, Y-Direction Response Spectra, 5% Damping.
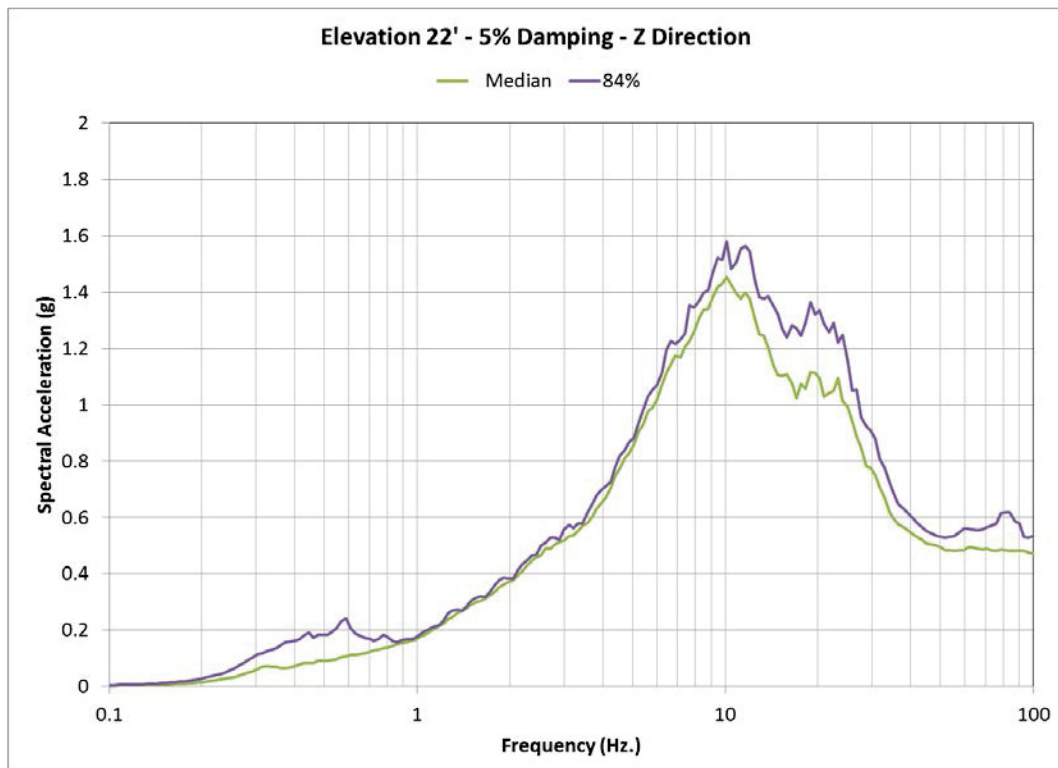
Figure 33.   Elevation 22ft, Vertical Response Spectra, 5% Damping.
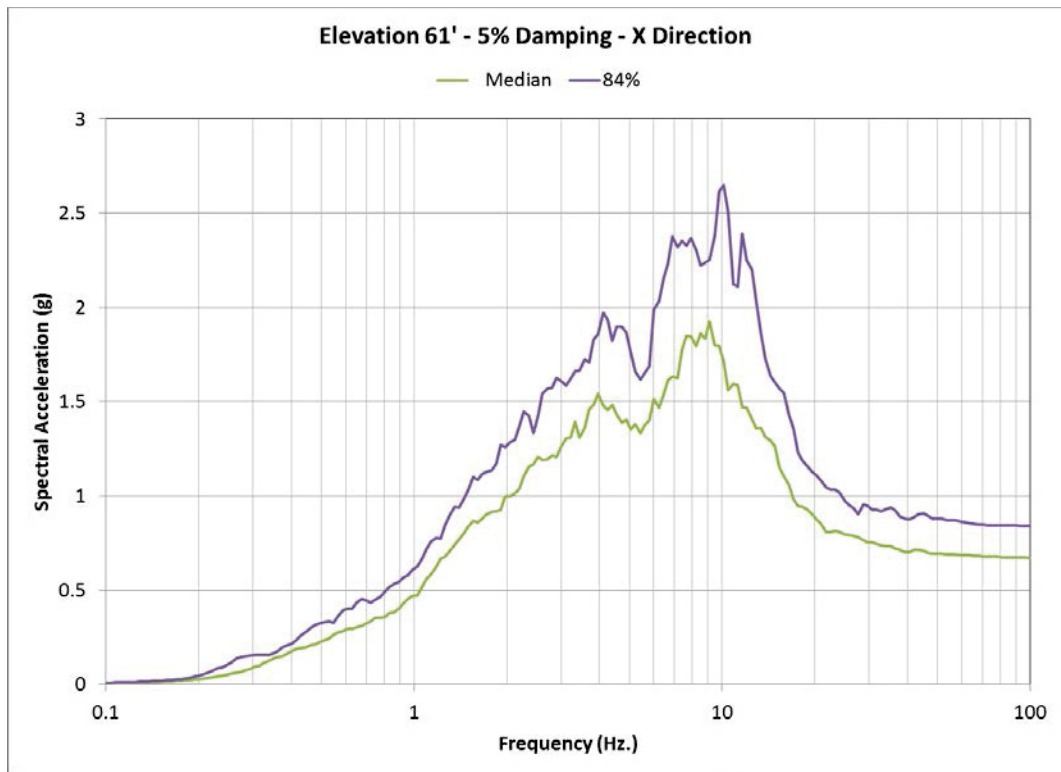
Figure 34.   Elevation 61ft, X-Direction Response Spectra, 5% Damping.
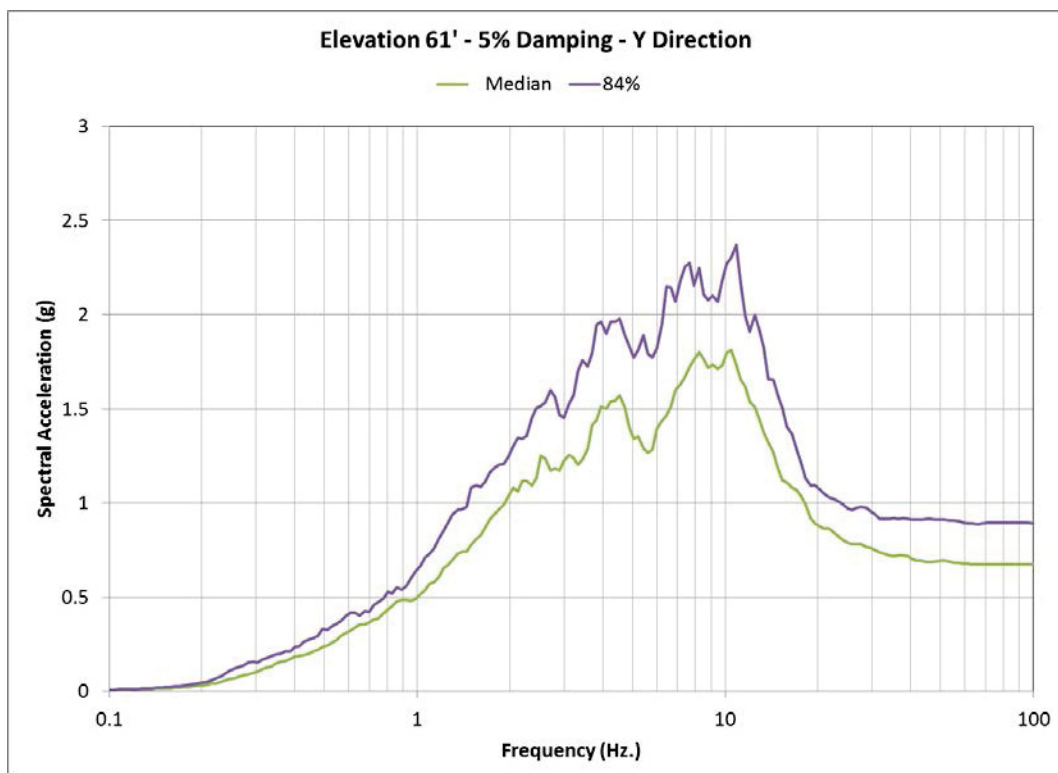
Figure 35.   Elevation 61ft, Y-Direction Response Spectra, 5% Damping.
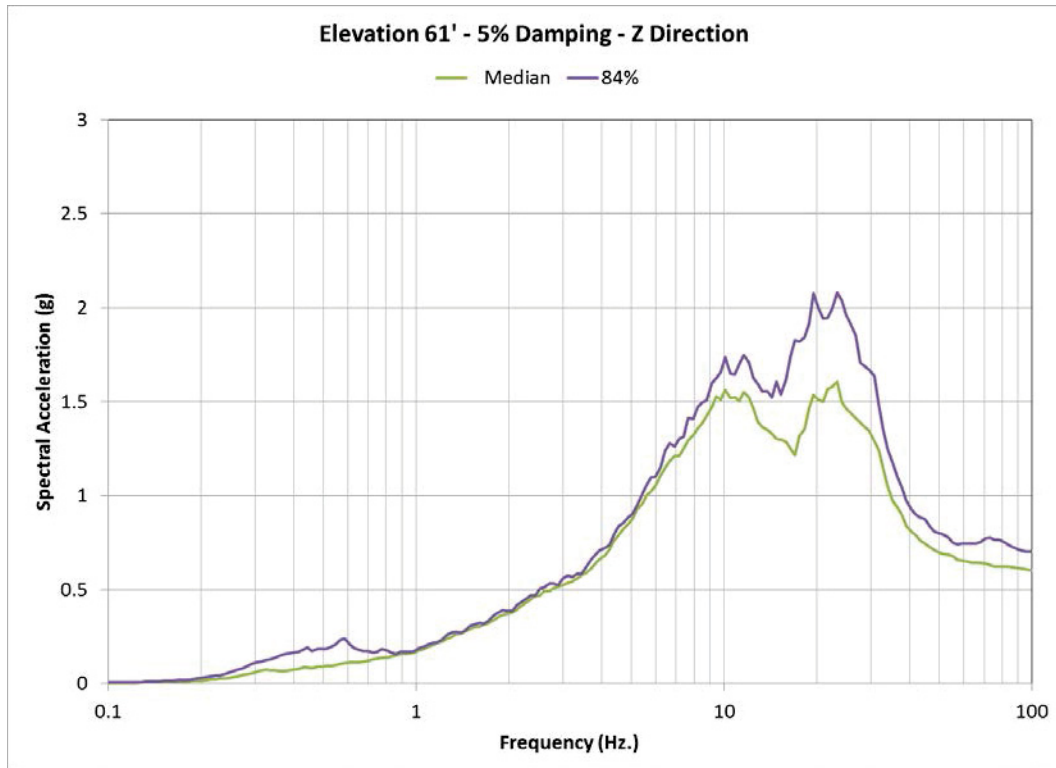
Figure 36.   Elevation 61ft, Vertical Response Spectra, 5% Damping.

4.1.2.2   Seismic Component Fragility Evaluation

The system logic model shown in Section 4.1.1.3.2 relies on five components of the Emergency Cooling Pump system. Seismic fragilities for these components are listed in Table 6. Their development is presented in detail in Bolisetti et al. (2015). A general approach is described below.

The seismic fragilities were calculated by the separation-of-variables method presented in EPRI TR-103959 (EPRI 1994) and supplemented by guidance in EPRI 1019200 (EPRI 2009). The seismic fragility was expressed as the probability of component failure conditional on the horizontal PGA. The seismic fragility evaluation used existing documentation developed in the previous ATR deterministic seismic evaluation and SPRA, such as DOE/EH-0545 (DOE 1997) Screening and Evaluation Worksheets and screening calculations, and seismic fragility calculations. Component and anchorage configurations were selectively adjusted from the actual configurations to achieve a mix of fragilities controlled by functional and anchorage failure.

Using the separation-of-variables method, the component fragilities were developed in terms of the following factors that contribute to seismic capacity:

- Component capacity: Strength, inelastic energy absorption

- Component response: Qualification method, damping, frequency, mode shape, mode combination, earthquake component combination

- Structure response: Ground motion (including earthquake response spectrum shape, horizontal earthquake peak response, and vertical component response), damping, modeling (including frequency and mode shape), mode combination, time history simulation, and foundation-structure

54

interaction (including ground motion incoherence, vertical spatial variation of ground motion, and SSI analysis)

For this study, variability was represented by the composite lognormal standard deviation without distinction between randomness and uncertainty.

Median component capacities, component responses, and associated variabilities were determined on a component-specific basis. Median component responses were determined for the median ISRS obtained by the probabilistic structure seismic response analysis for median component frequencies and damping. Structure response variability was determined based on the differences between the median and 84% NEP ISRS for the median component frequencies and damping.

Table 6. Component seismic fragilities.

Component	Floor	A_m	β_c	HCLPF
Pump	EL 61ft	3.40g	0.41	1.31g
Battery	EL 22ft	1.14g	0.28	0.59g
Distribution Panel	EL 61ft	1.60g	0.59	0.40g
Switchgear	EL 22ft	1.90g	0.47	0.64g
Block Wall	EL 61ft	0.60g	0.28	0.31g

4.1.3 Demonstration of Advanced Seismic Probabilistic Risk Assessment Using Nonlinear Soil-Structure-Interaction Analysis

The NLSSI was performed using the commercial time-domain code, LS-DYNA. LS-DYNA is a commercial finite-element program, currently developed and maintained by the Livermore Software Technology Corporation (LSTC). It is predominantly used for solving structural mechanics problems using the explicit integration algorithm, which makes it suitable for applications involving sudden loads (crash and blast simulations) and contact problems. The implicit integration algorithm is also implemented in LS-DYNA, but with limited capabilities. LS-DYNA includes a large database of material models for simulating soil and structure (especially steel and concrete), contact interfaces and seismic isolators. LS-DYNA has seen increasing usage in the civil engineering industry with applications in nonlinear site-response, and SSI analyses of buildings, bridges and LNG tanks (Willford et al. 2010). LS-DYNA is therefore considered a suitable choice for nonlinear SSI analysis of this study.

Nonlinear response in SSI analyses is a result of several factors. These include, nonlinear site response, which affects the foundation-level input motion to the structure, hysteretic response of the soil at the vicinity of the foundation, which results in foundation flexibility and hysteretic energy dissipation at the foundation and gapping and sliding of the foundation. The nonlinear SSI analyses in this report are performed considering only the geometric nonlinearities at the foundation-soil interface, which are of primary interest in this study. The ISRS at the locations of selected components are calculated and used in the seismic fragility calculations. The seismic fragilities for each component are then compared with those calculated using the traditional SPRA process described in Section 4.1.2.

4.1.3.1   The Nonlinear Soil-Structure-Interaction Methodology

Spears and Coleman (2014) proposed a methodology to perform nonlinear soil-structure interaction analysis in the time domain. This methodology, referred to as the NLSSI methodology, is a series of steps that an analyst of reviewer can follow to perform a fully nonlinear SSI analysis in the time domain including nonlinear site response, nonlinear hysteretic soil behavior at the foundation vicinity, geometric nonlinearities at the foundation including gapping and sliding and nonlinear behavior of the structure such as concrete cracking. The NLSSI methodology (illustrated in Figure 37) is used to perform the nonlinear SSI analyses in this project. As shown in the flowchart, building an NLSSI model involves building the structural model, building the soil domain model, building the interface model, and specifying the input. Each of these models should be independently verified for the desired properties before assembling the NLSSI model and performing the analysis to calculate the output.

The nonlinear SSI analyses of this study are performed along the lines of the NLSSI methodology. The description of structural modeling, soil domain modeling and input specification, interface modeling, and the NLSSI model assembly are presented in Bolisetti et al. (2015), which also presents the benchmarking and verification of the NLSSI model.
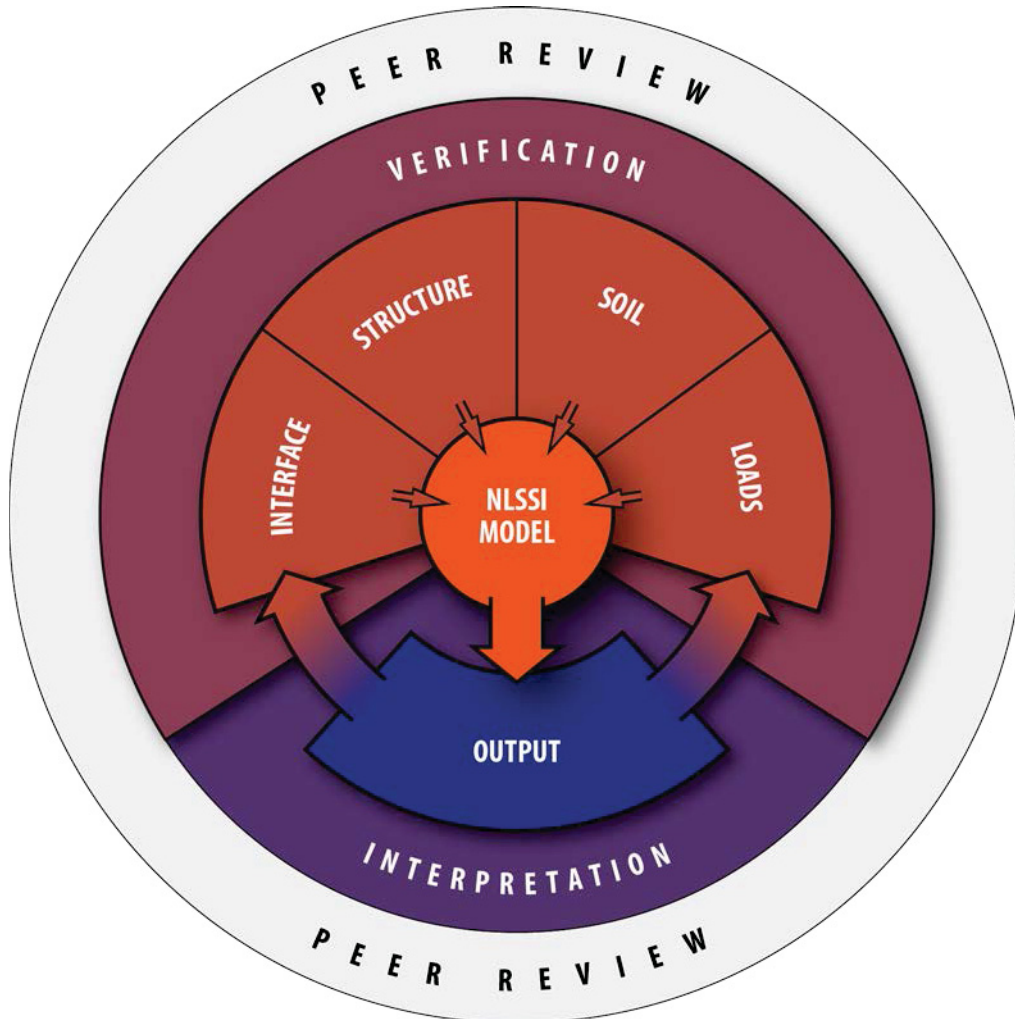
Figure 37.   The nonlinear soil-structure-interaction methodology (from Coleman et al. 2015).

4.1.3.2   Nonlinear Soil-Structure-Interaction Modeling

Soil-structure interaction in the time domain is typically performed using the direct method (Bolisetti and Whittaker 2015, Spears and Coleman 2014). In the direct method, the whole soil-structure system is analyzed in a single step thereby circumventing the use of superposition, which is extensively used in traditional SSI analysis methods (including SASSI and CLASSI) and is restricted to linear analyses. This enables a more realistic simulation with the use of nonlinear material models for the soil and structure, and contact models that simulate separation and sliding at the foundation-soil interface. Soil-structure interaction analysis using the direct method can be performed using most commercial finite-element codes such as ABAQUS (Dassault Systèmes 2005), ANSYS (ANSYS Inc. 2013), LS-DYNA, or the open source finite-element code, OpenSees (Mazzoni et al. 2009). Figure 38 presents a sample finite-element model for SSI analysis using the direct method in LS-DYNA.
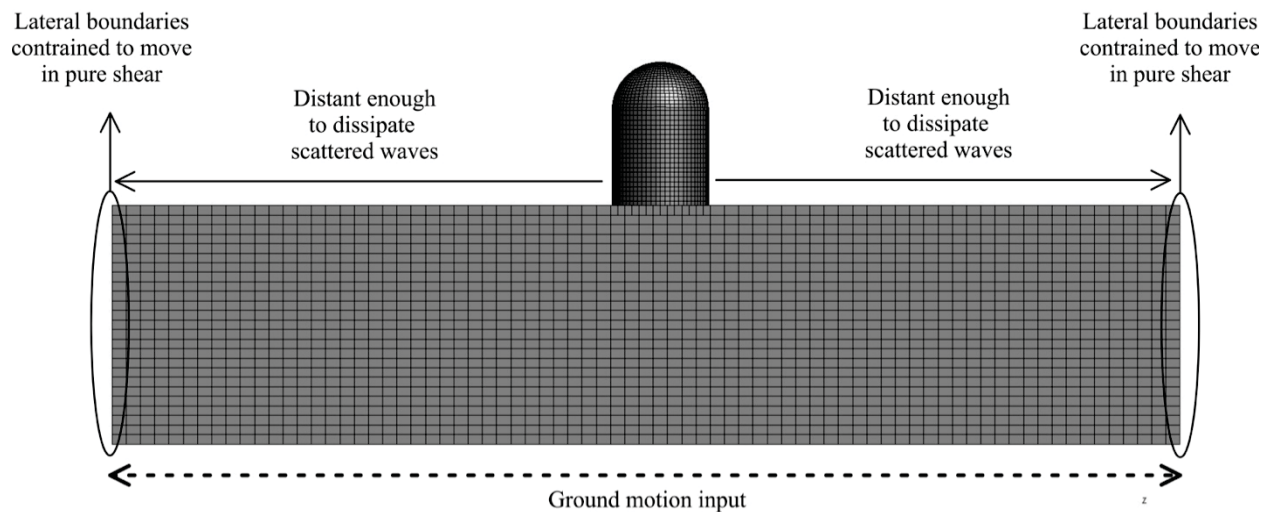
Figure 38.   Description of a finite-element model for soil-structure interaction analysis using the direct method (from Bolisetti, Whittaker and Coleman 2016).

The finite domain in the direct method needs to satisfy the following conditions in order to simulate an infinite domain: (1) effective damping of the waves radiating away from the structure so that they do not reflect back into the soil domain from the lateral boundaries, and (2) stress equilibrium at the lateral boundaries to account for the rest of the soil domain that is not included in the finite domain model. The former is achieved by building a large soil domain with sufficient plan dimensions to dissipate the radiating waves before they reach the lateral boundaries. In this approach, the radiating waves are dissipated through hysteresis and viscous damping in the soil. The plan dimensions of the domain can be determined by a trial-and-error procedure, ensuring that the acceleration responses at the boundaries of the soil domain are equal to the free-field acceleration, which is calculated from a separate site-response analysis, and also by verifying that the structural response does not change with a further increase in the domain size. Stress equilibrium at the lateral boundaries can be obtained by constraining the boundary nodes at each elevation to move together in each direction. This enables the elements at the boundaries to move in pure shear, thus simulating a free-field condition (assuming that the input comprises vertically propagating shear waves), as shown in Figure 38.

The LS-DYNA numerical model for the SSI analysis of the representative NPP structure is presented in Figure 39. As illustrated in the figure, the soil domain of this model is 665 ft ✕ 665 ft in plan (about 5 times the size of the basemat, which is 131 ft in diameter), and 214 ft deep. The dimensions of the soil domain are chosen after trying two soil domain sizes. The chosen dimensions are verified by

comparing the surface response at the edge of the soil domain to the free-field response from a separate one-dimensional site-response analysis. The soil domain is built with about 192,000 solid elements that have an almost uniform size of 8ft in all directions. This element size allows the propagation of frequencies up to about 40Hz, assuming 10 elements per wavelength. The base of the soil domain is modeled as a transmitting boundary using the *BOUNDARY_NON_REFLECTING option in LS-DYNA. The ground motion input in the CLASSI analysis is applied at the free field, which is not possible in the direct method. However, given that soil domain is completely uniform, it can be assumed that the ground motion recorded at the free field is caused purely by the incident waves from the soil domain. These incident waves can be applied as an outcrop input to the LS-DYNA soil domain at any depth, in order to achieve the same free-field ground motion as CLASSI. The outcrop input is applied as a shear force history as shown in Figure 40. This creates an incident wave that is reflected back into the soil domain at the surface. The dampers shown in Figure 40 absorb the reflected wave, simulating an infinite soil domain. To verify that the input excitation in CLASSI and LS-DYNA are equivalent, the free-field response from LS-DYNA (which is the surface response of the soil at the edge of the domain far from the structure) is compared with the free-field input in the CLASSI simulations. Figure 41 presents the spectral accelerations of the free-field input in CLASSI and the free-field response in LS-DYNA in X, Y and Z directions. The figure clearly shows that the responses are almost similar, except that the LS-DYNA response is slightly smaller in the higher frequencies. This can be attributed to finite domain effects and difference in the damping formulations in the two codes.
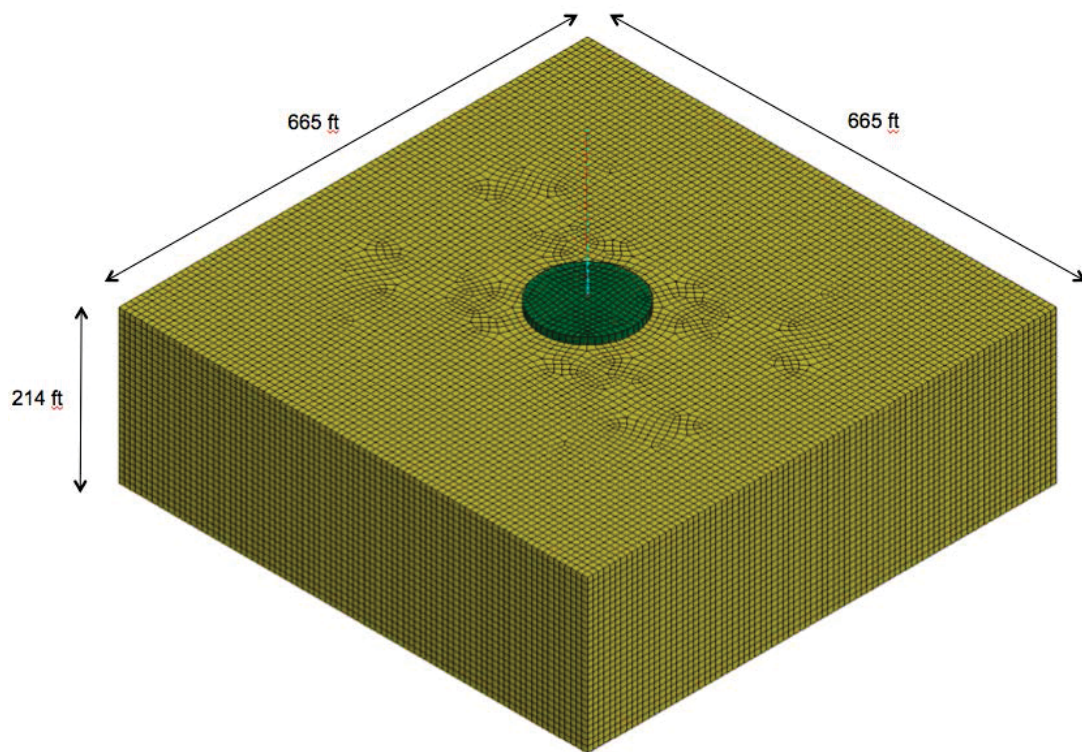
Figure 39.   Finite-element model for the SSI analysis of the representative nuclear power plant structure (oblique view).
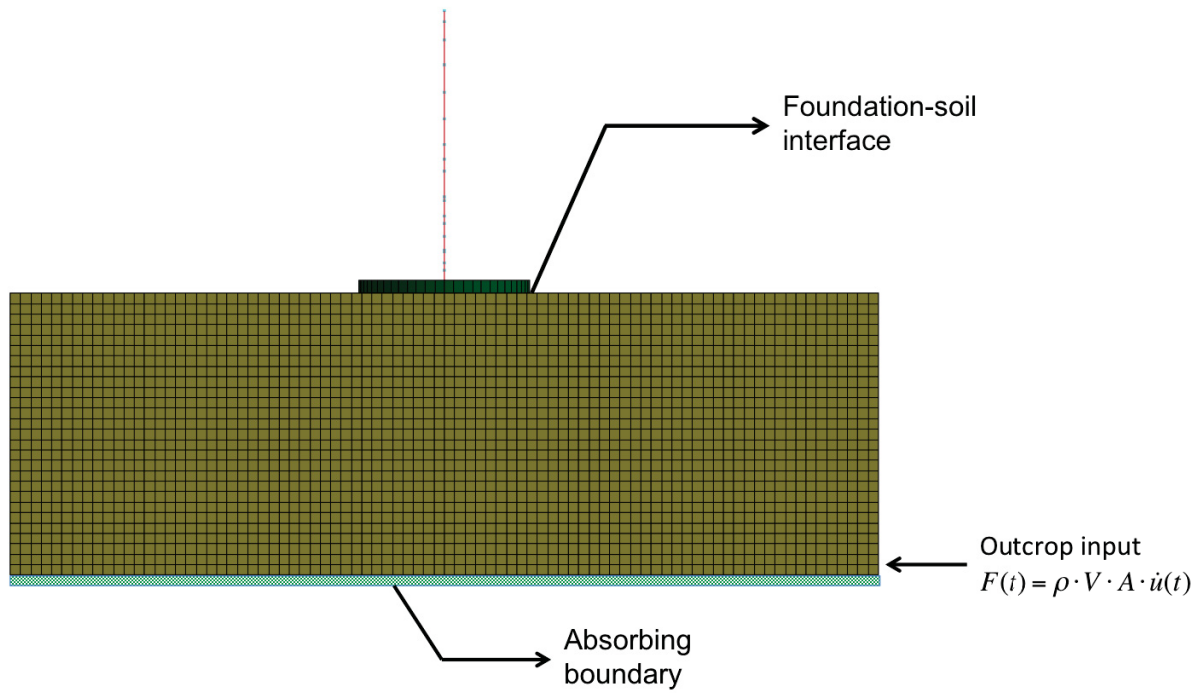
Figure 40.   Finite-element model for the SSI analysis of the representative nuclear power plant structure (side view).
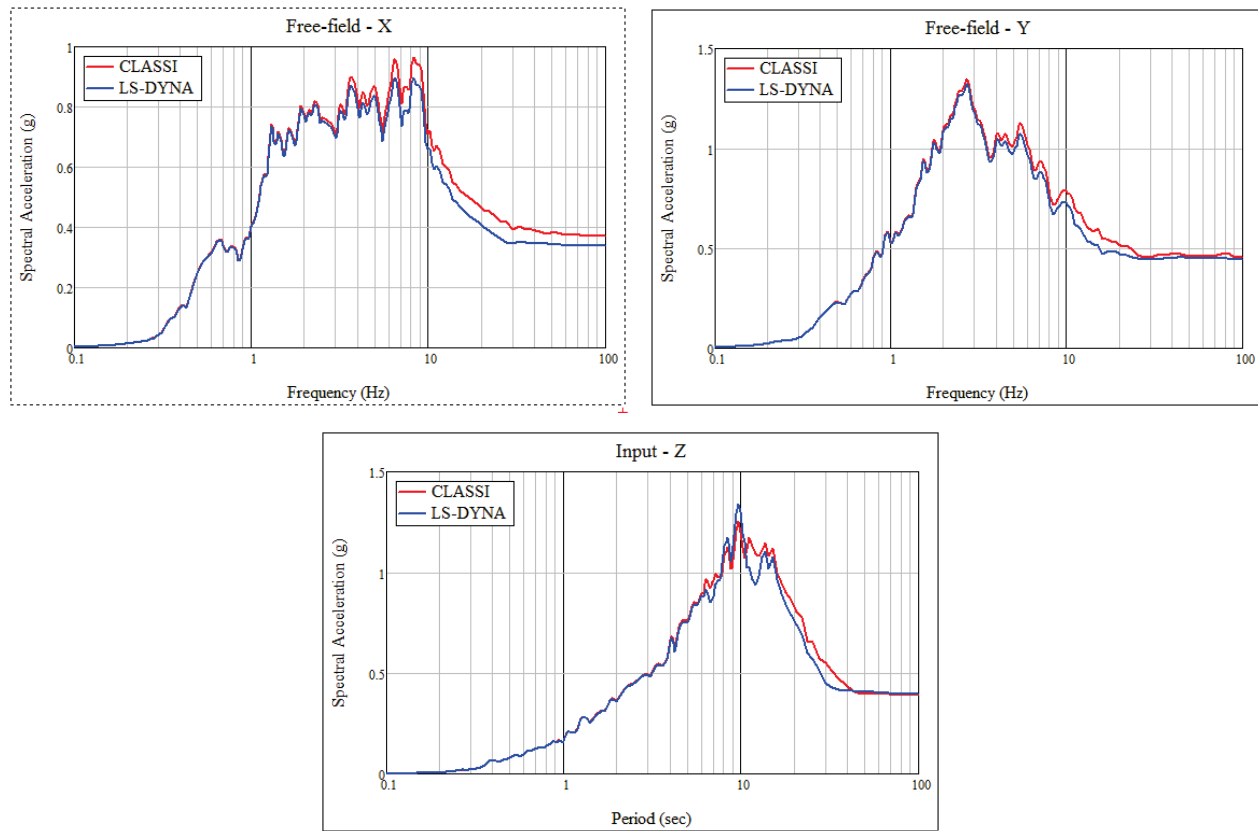
Figure 41.   Response spectra (5% damped) of the free-field input acceleration in CLASSI and the free-field acceleration calculated using LS-DYNA.

4.1.3.3   Seismic Component Capacity Distributions

The component capacity distribution describes the conditional probability of failure given the in-structure spectral acceleration. The spectral acceleration capacity distributions listed in Table 7 were derived from the component seismic fragilities (Section 4.1.2.2). The median spectral acceleration capacity represents the 5% damped in-structure spectral acceleration in the controlling direction of motion at the median component frequency for which, the net median demand on the controlling element equals its median capacity. The variability is represented by the lognormal standard deviation for component capacity.

Table 7.   Component spectral acceleration capacity distributions.

Component	Floor	Direction	Frequency (Hz)	SA_m	β_c
Pump	EL 61'	X	20	7.46g	0.16
Battery	EL 22'	Y	8.3	3.10g	0.10
Distribution Panel	EL 61'	X	7.5	6.24g	0.42
Block Wall	EL 22'	Y	0.89	0.73g	0.17
Switchgear	EL 61'	Y	5 - 10	4.8g	0.42

60

4.1.3.4   Seismic Component Demand Distributions

The seismic demand distributions at the locations of the components are calculated from probabilistic analyses in LS-DYNA, similar to the traditional probabilistic assessment described in Section 4.1.2. The properties listed in Table 7 are also randomized in the nonlinear SSI analyses, and the thirty ground motion sets used in the CLASSI simulations are used here. However, since the responses calculated from the nonlinear analyses do not scale linearly with ground motion intensity, the nonlinear SSI analyses are performed separately for four different ground motion intensities, corresponding to the PGAs of 0.4g, 0.6g, 0.9g and 1.2g. Therefore, 120 nonlinear SSI analyses are performed in total.

Results are calculated in terms of spectral accelerations at the locations of components in the controlling direction of motion as listed in Table 7. These results are presented in Figure 42 to Figure 45. Each of the figures presents the LS-DYNA spectral accelerations for thirty ground motions (gray lines), LS-DYNA median responses (green solid lines), and LS-DYNA 84th percentile responses (green dashed lines). The median response calculated using CLASSI (red solid lines) is also presented to enable comparison. The responses for all PGA levels, from 0.4g at top left to 1.2g at bottom right, are presented.
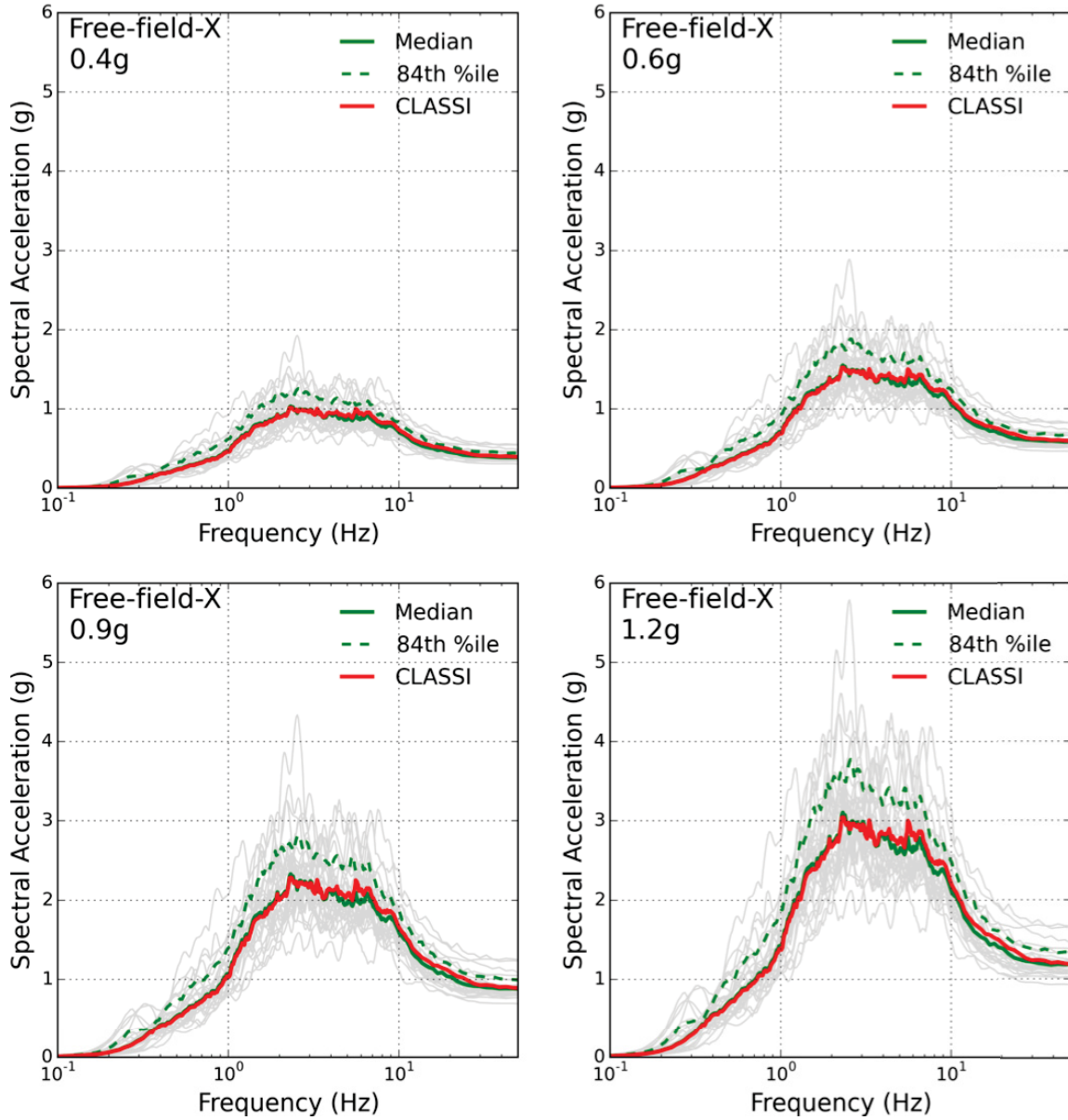
Figure 42.   Acceleration response spectra (5% damped) at the free field in X direction calculated using LS-DYNA, and the corresponding median response in CLASSI.
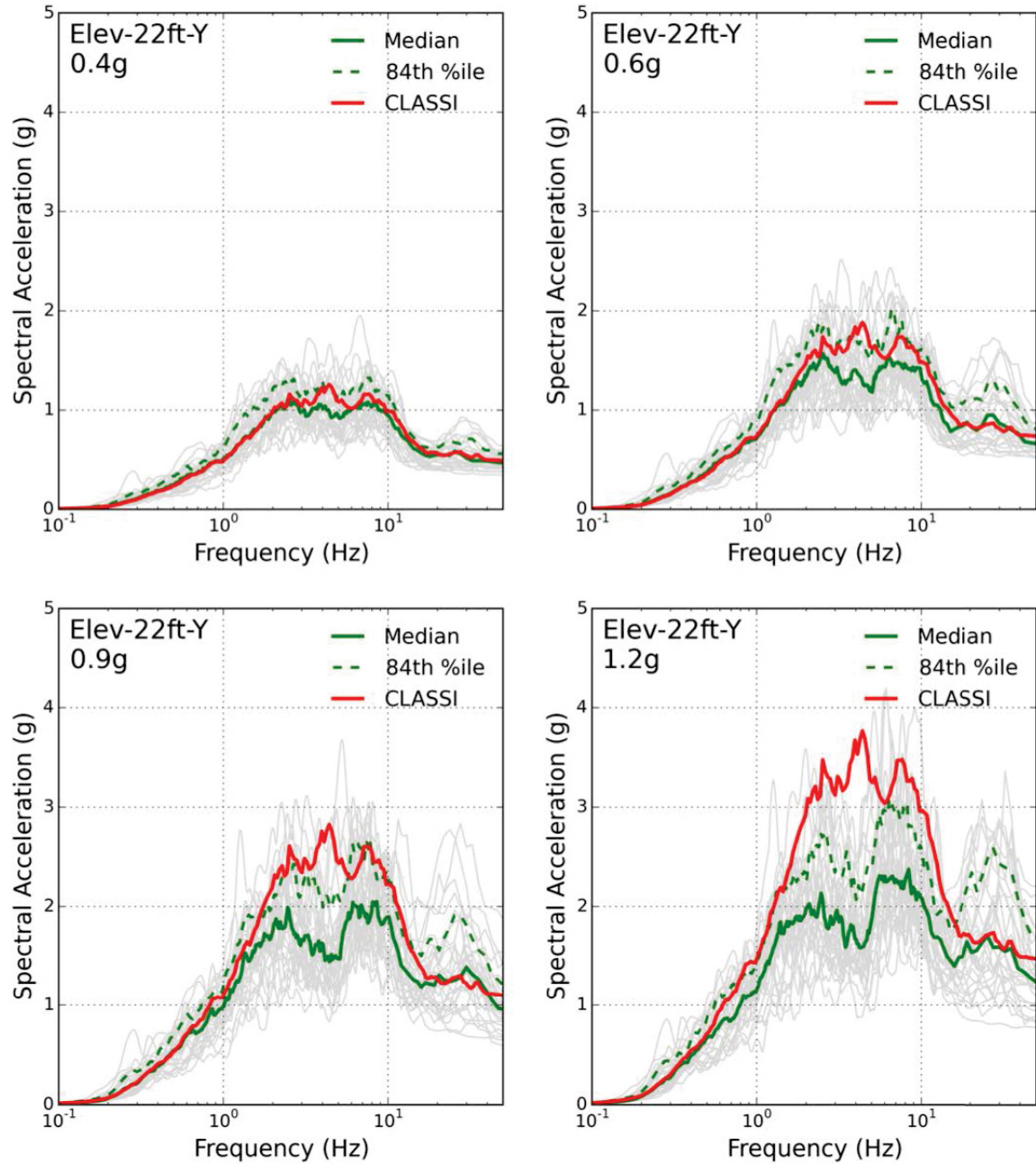
Figure 43. Acceleration response spectra (5% damped) in the Y direction in the internal structure at 22' elevation calculated using LS-DYNA, and the corresponding median response in CLASSI.
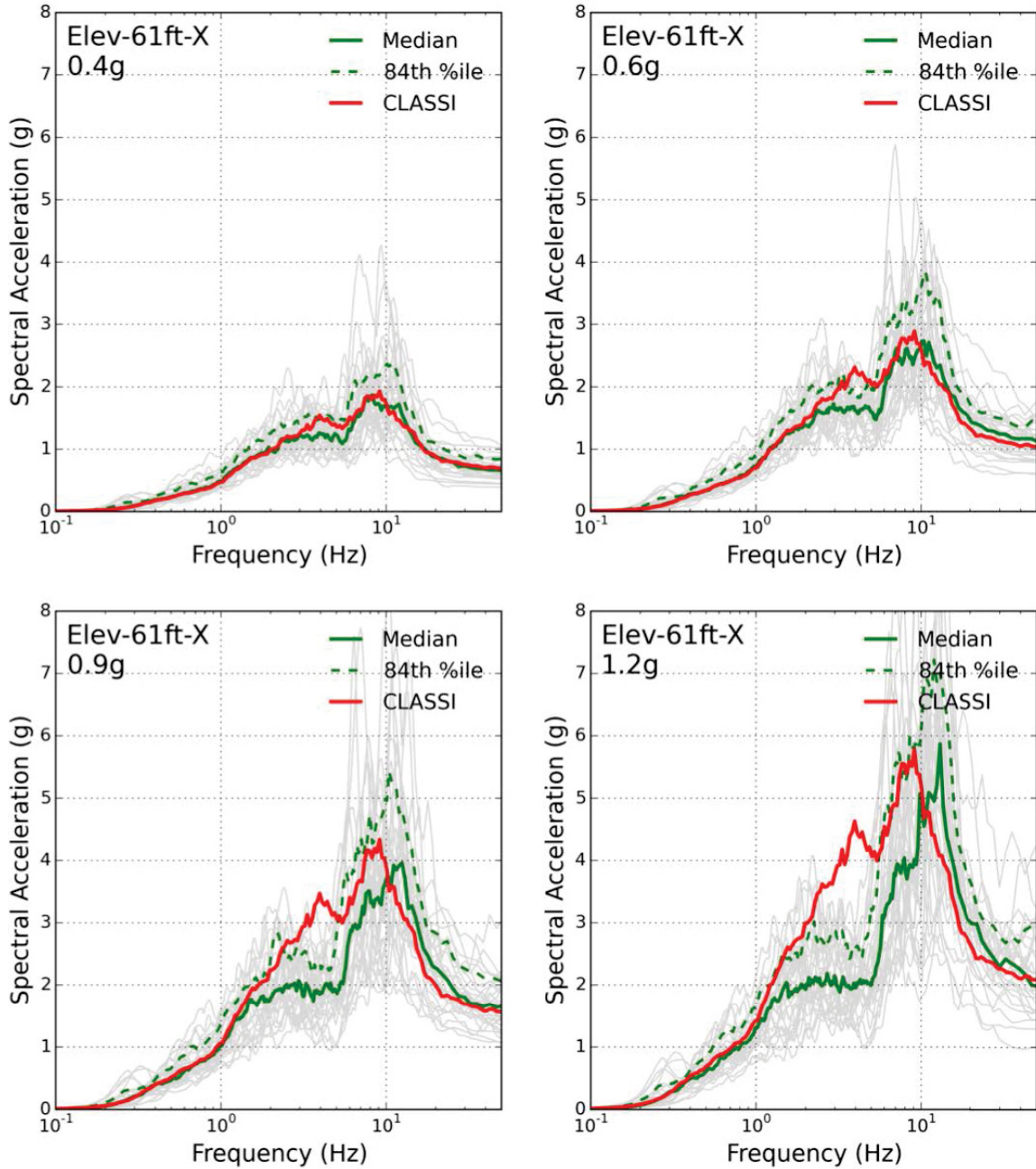
Figure 44.   Acceleration response spectra (5% damped) in the X direction in the internal structure at 61' elevation calculated using LS-DYNA, and the corresponding median response in CLASSI.
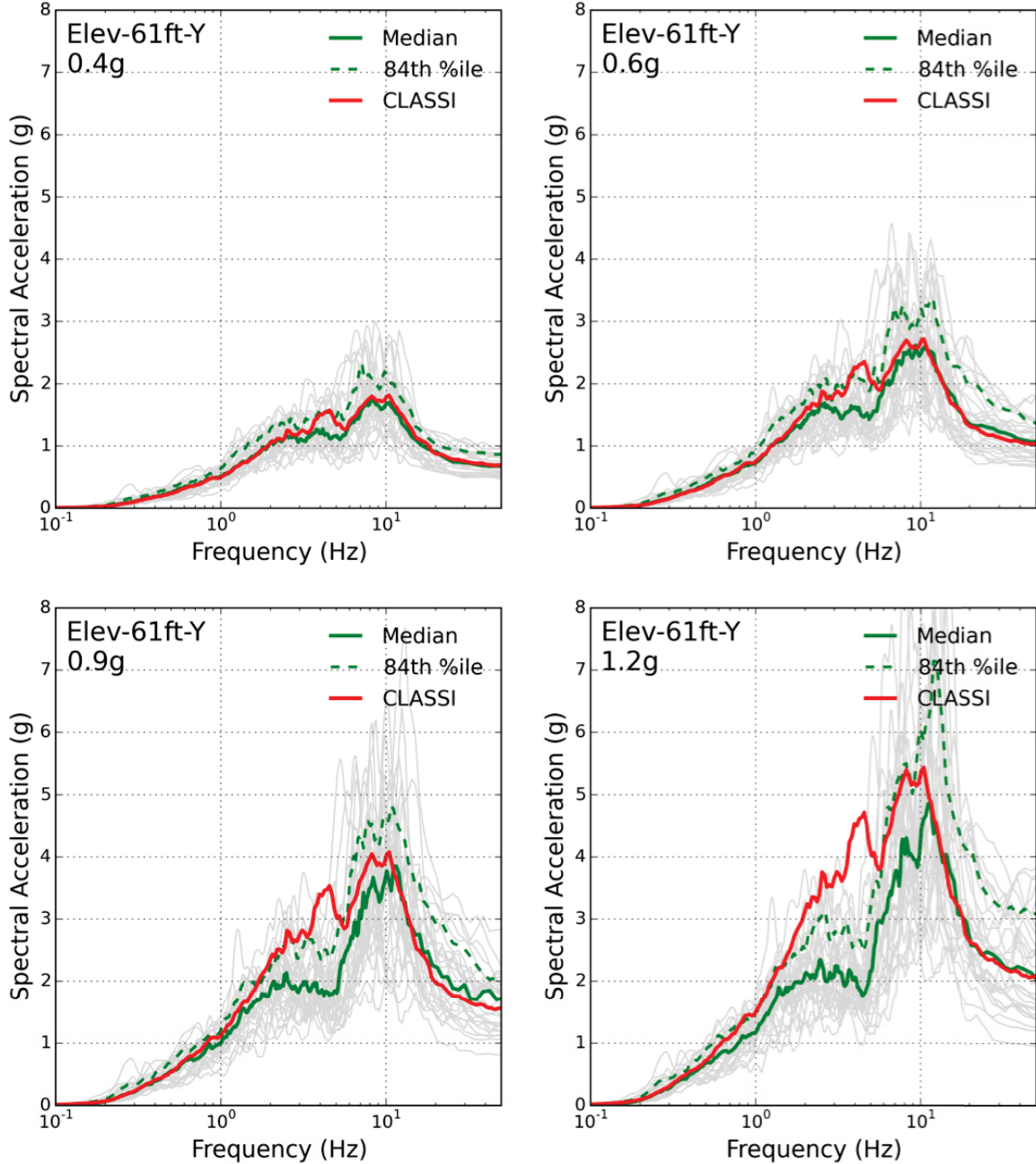
Figure 45. Acceleration response spectra (5% damped) in the Y direction in the internal structure at 61' elevation calculated using LS-DYNA, and the corresponding median response in CLASSI.

Figure 42 shows that the median free-field responses calculated using LS-DYNA are almost identical to the free-field inputs provided in CLASSI for all PGA levels. This provides further verification for the ground motion input procedure (described in Bolisetti et al. 2015) and enables an unbiased comparison between the ISRS calculated using CLASSI and LS-DYNA.

The ISRS presented in Figure 43 show that the LS-DYNA median responses are increasingly different from the corresponding CLASSI responses with an increasing PGA level. The median responses are very similar for a 0.4g PGA. For larger PGA levels, the LS-DYNA median spectral accelerations are considerably smaller for most frequencies than the CLASSI spectral accelerations. This demonstrates that

the geometric nonlinearities at the foundation-soil interface can result in significant energy dissipation and damp the in-structure response at most frequencies. Figure 44 and Figure 45 also show that the LS-DYNA median responses are larger than those calculated using CLASSI at frequencies greater than 10 Hz. This is a result of impact between the foundation and soil due to gapping, which can introduce high-frequency responses in the superstructure. Note that gapping is dominant in this structure because it is founded above the surface. However, nuclear structures are always built with at least a partial embedment, which can significantly reduce the degree of gapping. Therefore, this increase in in-structure spectral accelerations at higher frequencies due to geometric nonlinearities cannot be generalized to all nuclear structures.

The demand distribution parameters are calculated from the in-structure demands calculated from the LS-DYNA simulations as a median and a lognormal standard deviation. The median demand of a component is defined as the median of 30 5% damped ISRS at the component median frequency identified in Table 7. The medians and variabilities of the demand are calculated through component specific calculations and account for the variabilities in the component frequency, structural response, component damping, earthquake mode combination, component mode shape and other factors. A detailed description of the calculation of demand parameters is presented by Bolisetti et al. (2015). The demand distributions so calculated are presented in Table 8, below.

Table 8.   Component demand distribution summary.

Component	Median demand SA$_D$ (g) for PGA				Composite lognormal standard deviation. β$_D$ for PGA			
	0.4g	0.6g	0.9g	1.2g	0.4g	0.6g	0.9g	1.2g
Pump	0.86	1.42	2.21	2.97	0.36	0.34	0.36	0.35
Battery	1.03	1.43	1.93	2.23	0.34	0.32	0.35	0.34
Dist. Panel	1.51	2.16	3.02	3.54	0.24	0.27	0.31	0.35
Block Wall	0.49	0.71	0.94	1.12	0.37	0.39	0.42	0.48
Switchgear	1.03	1.41	1.87	2.20	0.25	0.27	0.31	0.32

4.1.3.5   Seismic Component Conditional Probabilities of Failure

The conditional probabilities of component failure are calculated by convolving the component capacity and demand distributions at each PGA level. Specifically, they are calculated as the probability that the demand is greater than capacity, given the capacity and demand distributions. Table 9 presents the conditional probabilities of failure of all components at the PGA levels considered in this study.

In order to perform a systems analysis, the component probabilities of failure need to be calculated at more than four PGA levels for a reasonable calculation of the system risk. This can be done using linear interpolation and extrapolation of the existing points or fitting a probability distribution in the points where the probability of failure is calculated. In this study, a lognormal fit is calculated for each component. This fit is calculated using the least squares method and the maximum likelihood estimate (MLE) method suggested by Baker (2015).

Table 9.   Conditional probabilities of failure the components.

Component	Conditional Probability of Failure P_f at PGA			
	0.4g	0.6g	0.9g	1.2g
Pump	0.000	0.000	0.001	0.007
Battery	0.000	0.004	0.073	0.183
Distribution Panel	0.006	0.032	0.111	0.187
Block Wall	0.094	0.465	0.763	0.881
Switchgear	0.001	0.009	0.035	0.072

The resulting fragilities are presented in Figure 46. The solid lines in this figure correspond to the fragilities calculated using linear analysis; the square markers denote the conditional probabilities of failure calculated using the nonlinear analyses and the dotted lines correspond to the lognormal fits. The acronym LS in the legend of the figure corresponds to the least squares fit and Baker MLE corresponds to the MLE fit.

Figure 46 shows that the fragilities calculated using nonlinear SSI analyses show generally smaller conditional probabilities of failure than those calculated using the linear analyses, especially at PGA greater than about 0.6g. However, note that the fragility fits show larger conditional probabilities of failure at smaller PGA values, especially for the block wall and switchgear. This is only a consequence of fitting the lognormal curve and it is safe to assume that the conditional probabilities from linear and nonlinear analyses are equal at PGA values smaller than 0.4g since the model was essentially linear (Bolisetti et al. 2015).

The figure also shows that the NLSSI failure probabilities are larger for the pump. This is mainly due to larger spectral accelerations at higher frequencies resulting from impact between the foundation and soil due to gapping. However, note that these probabilities are very low compared to the failure probabilities of other components and therefore may not significantly affect the system risk.

In contrast to the pump fragility, the fragility of the block wall shows high probabilities of failure in comparison with other components. This is due to the low spectral acceleration capacity of the block wall. The high probability of failure is likely going to have a considerable effect on the system risk as seen in the next section.
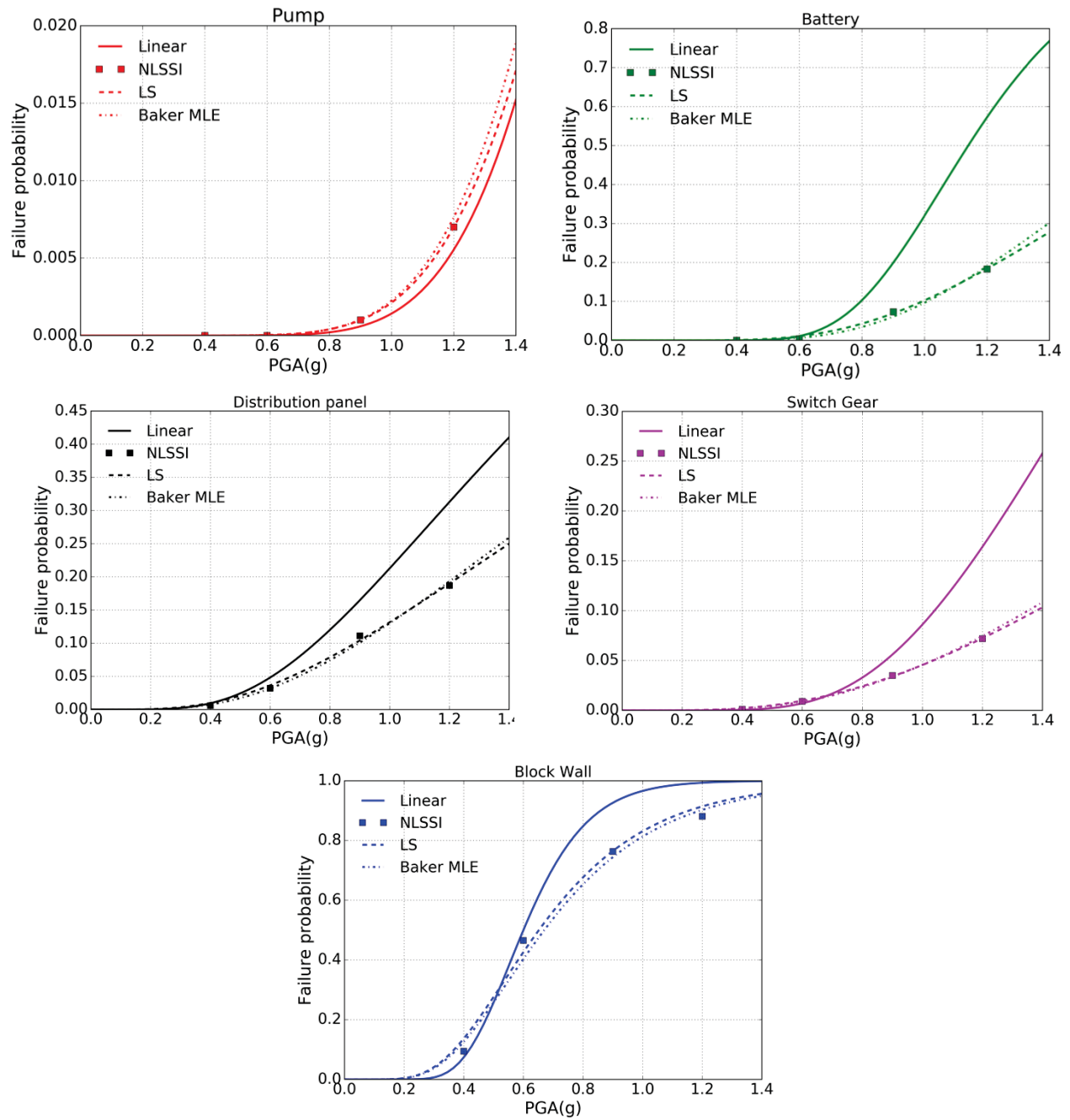
Figure 46.   Component fragilities calculated using linear SSI analyses and nonlinear SSI analyses.

4.1.3.6   Systems Analysis and Calculation of Risk

The component fragilities calculated in the previous section are used along with the fault tree and event tree, illustrated in Figure 29 and Figure 30, respectively, to calculate the system probability of failure, namely the system fragility. The system fragility is then convolved with the hazard curve to calculate the final risk. This is done in the following steps:

1. The component fragility curves and the seismic hazard curve are divided into 15 PGA bins. The mid-point of each bin is assumed to be the PGA of the bin and the corresponding probabilities from the component fragilities are assumed to be the probabilities of failure for that bin.

2. The system probability of failure is calculated for each PGA bin by propagating the component failure probabilities through the system fault tree and even tree using Boolean logic. This calculation is made for all the bins to calculate the final system fragility curve.

3. The system fragility curve is then convolved with the seismic hazard curve to calculate the final risk. This convolution integration is performed in a discrete fashion using the equation below

$$Risk = \sum_{All\ bins} \Delta MAFE \cdot P(f)$$

where ΔMAFE is the mean annual frequency of the PGA being in the specific bin, and *P(f)* system probability of failure in that bin.

These calculations are performed for the fragilities from linear SSI analyses, nonlinear SSI analyses with least squares fragility fit, and nonlinear SSI analyses with MLE fragility fit. Prior to performing these calculations, the component fragility curves are corrected such that the linear and nonlinear fragilities are equal until a PGA of 0.4g. This correction is made to avoid errors in the risk calculations since lower PGAs can contribute significantly to the risk. Figure 47 presents the original and corrected fragilities for the switchgear. The original fragilities in the figure clearly show that the nonlinear fragilities are higher than the linear fragilities. The nonlinear fragilities are changed to be equal to the linear fragilities for all bins up to around 0.4g PGA and no changes are made to the bins beyond this PGA.

Figure 48 presents the system fragilities calculated using the modified component fragilities for the cases with block wall and without block wall. The figure shows smaller probabilities of failure when nonlinear SSI is employed, which is expected from the component fragilities. The system failure probabilities calculated using nonlinear SSI analyses are at most 20% smaller than those calculated from linear analyses for the case with block wall included (top panel) and at most 40% smaller when the block wall is excluded. The figure also shows that the different fitting methods used for the nonlinear case result in almost the same fragilities. Comparison of the fragilities in the top and bottom panels of the figure shows that the block wall dominates the system probability of failure. When the block wall is included in the fault tree, the failure probability of the system is more than twice the failure probability when the block wall is excluded. Table 10 presents the final values of risk and the percentage reduction in risk due to nonlinearities. Expectedly, there are significantly smaller values of risk when the block wall is excluded from the calculation. The reduction in risk from nonlinear SSI analysis is around 5-10% when the block wall is included and 10-20% when the block wall is excluded.

Figure 49 presents the risk contributions from various PGA levels. The figure shows that the PGA bins close to the DBE level shaking contribute to the risk the most for all cases. The risk calculated using nonlinear analyses has a slightly smaller contribution than that from the linear case in the beyond-design basis. This is because of the smaller failure probabilities in the beyond-design basis PGA values.

4.1.4   Sensitivity of System Risk to the Seismic Hazard Curve

The results of the previous section show a reduction in seismic risk assessed values when nonlinear SSI analysis used in the PRA calculations. However, this reduction is not significant, even when the block wall is not considered. This is likely because of the unrealistically steep slope of the hazard curve, which results in most of the risk being concentrated around the DBE shaking.

This section examines the change in the system risk when the slope of the hazard curve is reduced. For this exercise, a second hazard curve is developed by making the following modification to the hazard curve used in the previous calculations. The slope of the original hazard curve (termed curve 1) in log scale is halved by multiplying the PGA values of curve 1 (in log scale) by two. The curve is then anchored at the design basis PGA (0.4g and MAFE of 1.00E-04) by subtracting 0.4 from each of the PGAs. The resultant seismic hazard curve (termed curve 2) is presented in Figure 50, along with the original hazard curve used in the calculations of the previous sections.
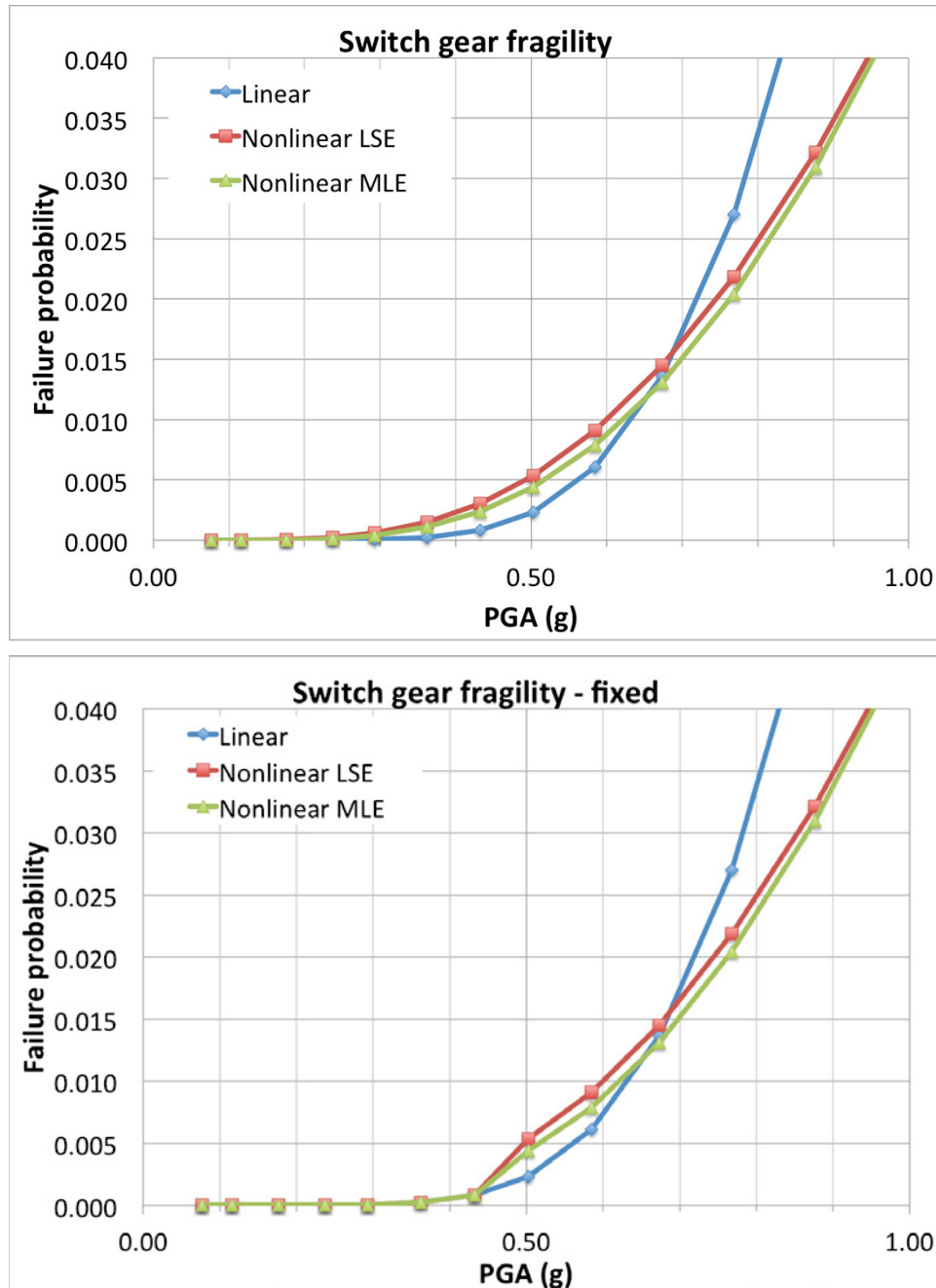
Note: Nonlinear fragility fits are corrected to be equal to the linear fragilities for all bins below 0.4g PGA.

Figure 47. Original (top) and corrected (bottom) fragility of the switchgear.

Figure 48. System fragility including the block wall in the fault tree (top) and excluding the block wall in the fault tree (bottom).

Table 10. System risk calculated using seismic hazard curve 1.

	With Block Wall		Without Block Wall	
	Risk	**% change from linear**	**Risk**	**% change from linear**
Linear SSI analysis	3.48E-05	-	4.62E-06	-
Nonlinear SSI analysis (LS fit)	3.32E-05	5	4.03E-06	13
Nonlinear SSI analysis (MLE fit)	3.20E-05	8	3.81E-06	17
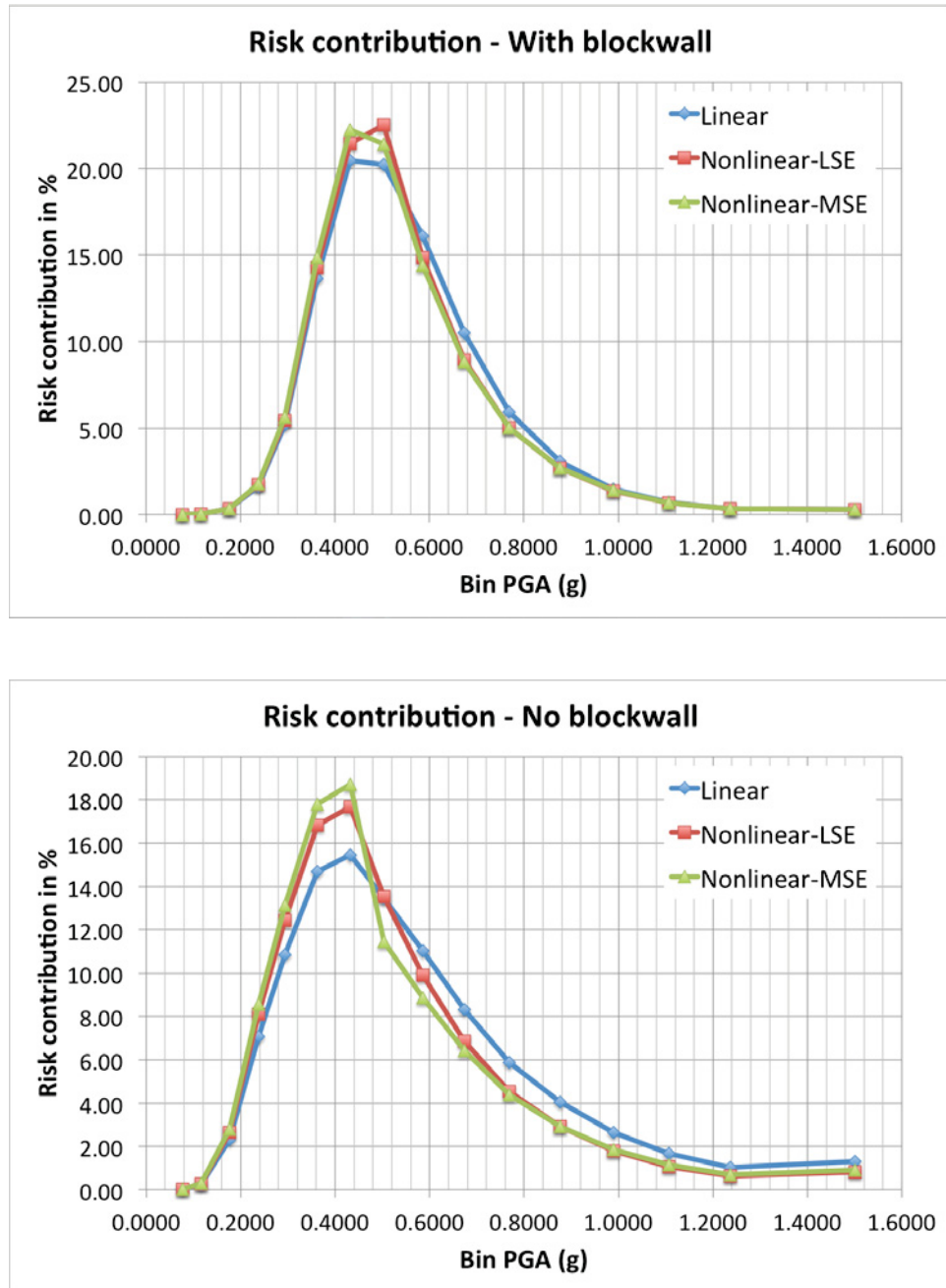
Figure 49. Risk contributions from the PGA bins when including the block wall in the fault tree (top) and excluding the block wall from the fault tree (bottom).
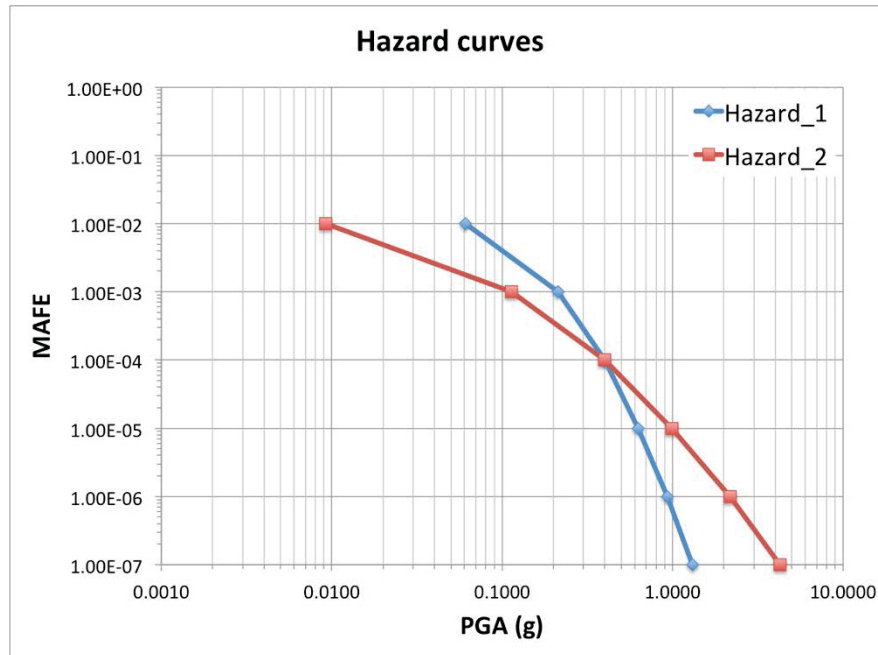
Figure 50.   Seismic hazard curves considered in this study.

Figure 51 presents the system fragilities calculated using hazard curve 2. Similar to the results calculated using curve 1, the fragilities calculated using nonlinear analyses show smaller failure probabilities. Also the failure probabilities are much higher when the block wall is included in the calculations. Additionally, the failure probabilities for the case with the block wall excluded range until a value of 1, unlike in the calculations of the previous section, because curve 2 spans a much larger range of PGA.

Table 11 presents the seismic risk calculated for all cases using hazard curve 2. The reduction in risk as a result of nonlinear analysis is around 10% when the block wall is included and around 30% when the block wall is excluded. While the reduction in risk is not significant for the case with the block wall (because the block wall dominates the risk and the nonlinear effects in the block wall response are small), it is significant when the block wall is not considered. This change from the calculations in the previous section is mainly because the beyond-design portion of the seismic hazard curve contributes more to the risk, where the nonlinear effects are significant. This is evident from the risk contributions presented in Figure 52.
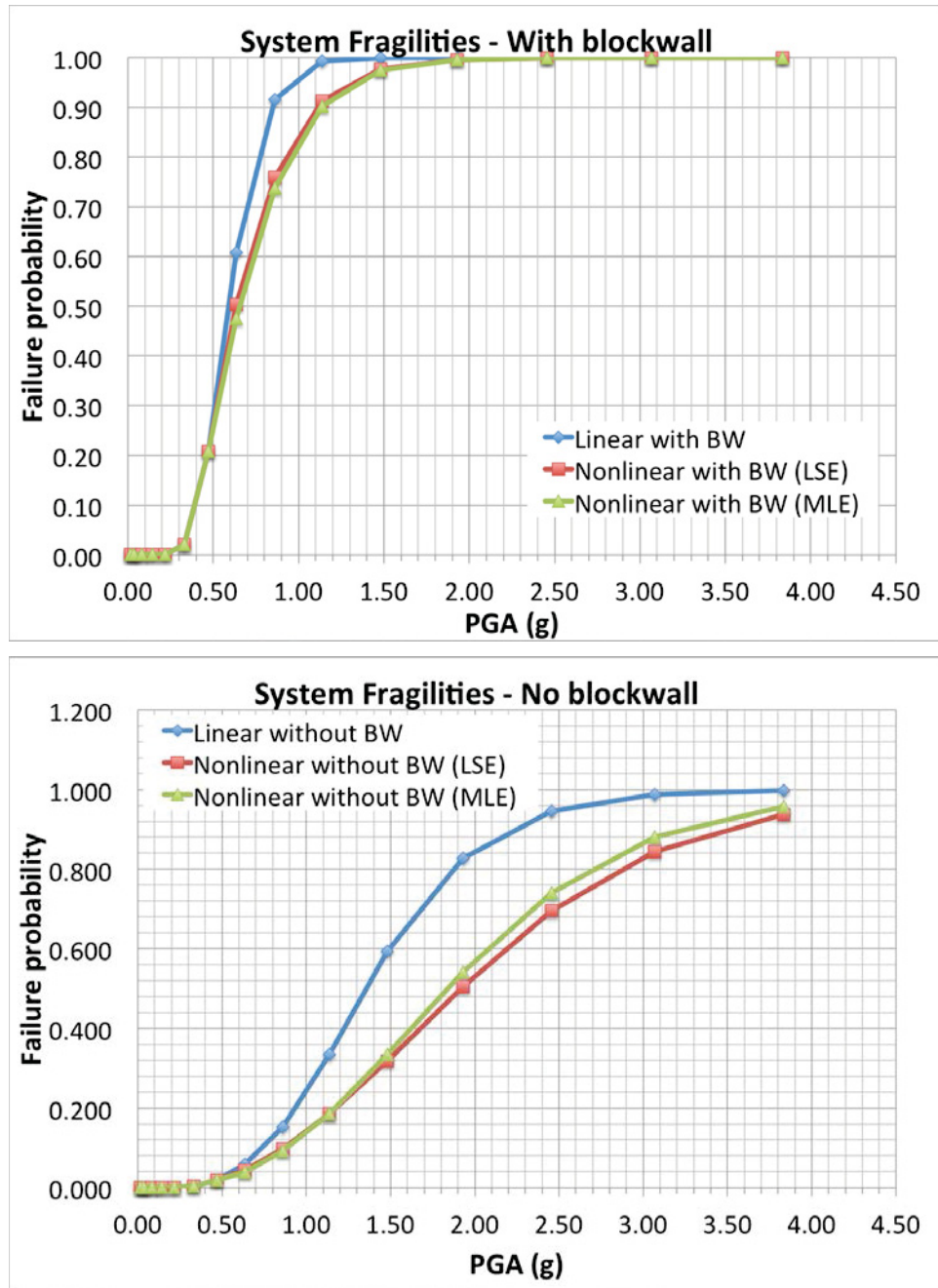
Figure 51. System fragilities calculated using seismic hazard curve 2 while including the block wall in the fault tree (top) and excluding the block wall in the fault tree (bottom).

Table 11. System risk calculated using seismic hazard curve 2.

	With block wall		Without block wall	
	Risk	**% change from linear**	**Risk**	**% change from linear**
Linear SSI analysis	4.93E-05	-	9.98E-06	-
Nonlinear SSI analysis (LS fit)	4.44E-05	10	6.93E-06	31
Nonlinear SSI analysis (MLE fit)	4.34E-05	12	6.85E-06	31

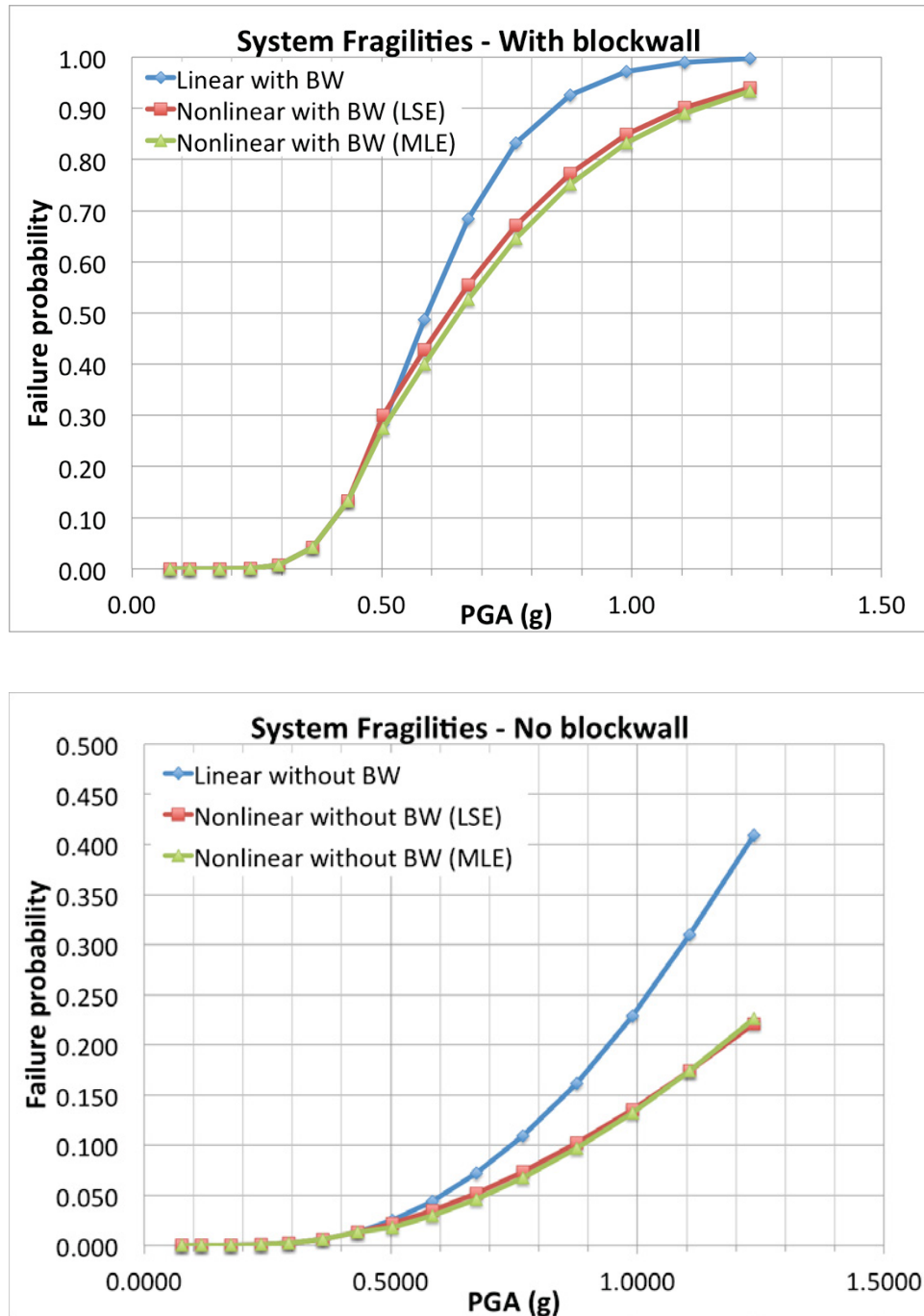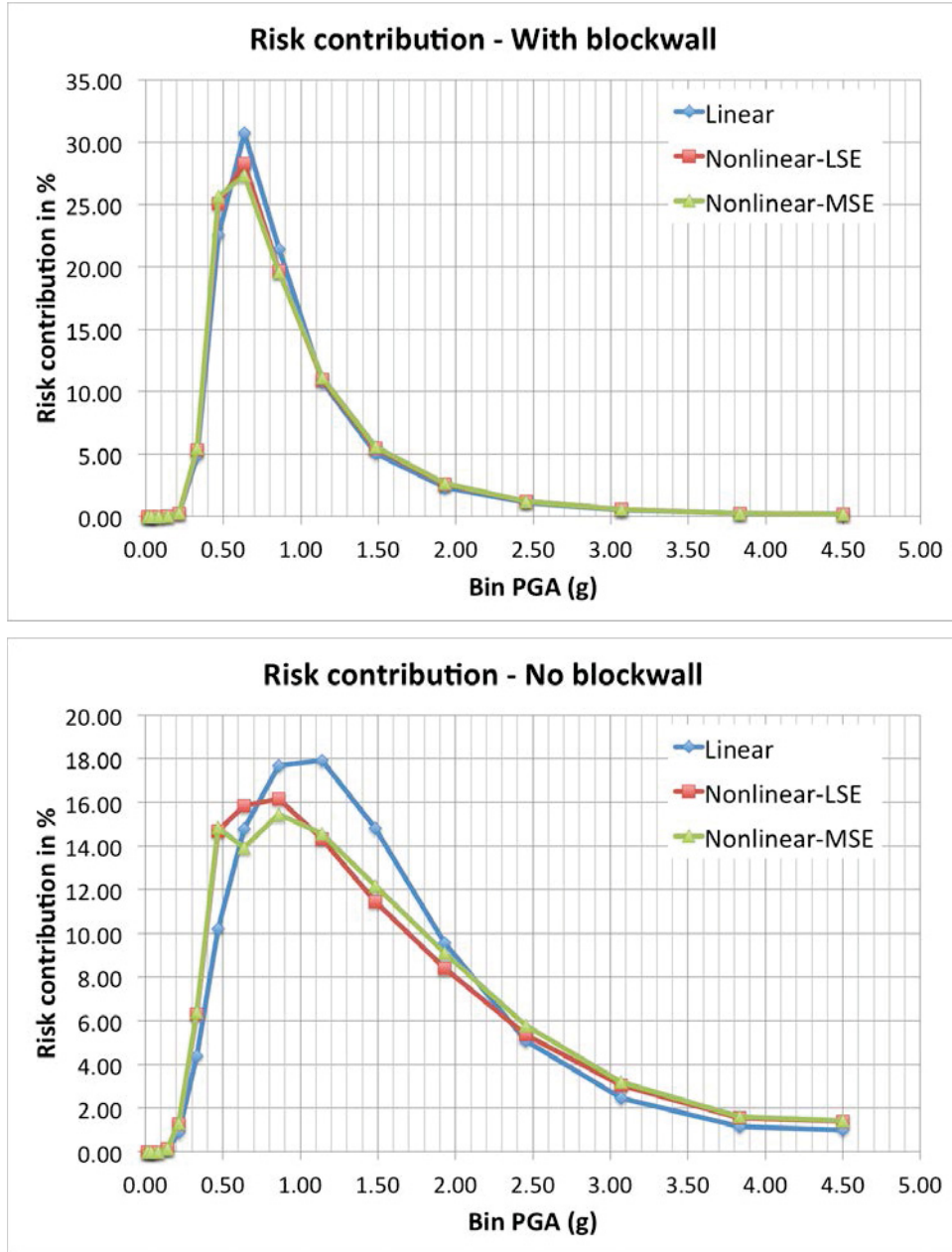Figure 52.   Risk contributions from the PGA bins calculated using seismic hazard curve 2 while including the block wall in the fault tree (top) and excluding the block wall in the fault tree (bottom).

4.2   Seismic-Flooding-Thermalhydraulic Dynamic Probabilistic Risk Assessment Demonstration

4.2.1   Introduction

In the previous section we presented the methodology for the determining seismic effects on the NPP auxiliary building through NLSSI. Results of applying the methodology were also presented. In this section, those results will be used for:

- Determining piping stresses and strains on the sprinkler system located in the auxiliary building. A failure probability versus earthquake intensity is then derived for the nodes with the highest stress value.

- Informing a simplified PRA model for a station black-out (SBO) event. Failure probabilities versus seismic motion intensity are assigned for some relevant components located in the auxiliary building, [e.g. batteries, Turbine Driven Auxiliary Feed-Water (TD-AFW), and sprinkler piping].

  Other sets of deterministic calculations being performed are:

- Flooding calculations using the Neutrino code for the sprinkler nodes subjected to higher stresses during an assessed seismic event. Neutrino is, thus, determining if a particular sprinkler pipe failure leads to component damage (e.g., switchgear, battery charger, battery, etc.)

- System thermal-hydraulic calculations by RELAP5-3D code, for determining the NPP dynamic during the SBO event. RELAP5-3D is calculating the FOM of the SBO event (peak cladding temperature (PCT) or coping time (CT). RELAP5-3D results are informed by the UQ analysis performed using the RAVEN code.

  The EMRALD tool manages the entire process described above.

4.2.2   Piping Analysis

4.2.2.1   Introduction

A three dimensional (3-D) spatial model of the fire suppression system in a sample plant service building was developed by SC Solutions. This model was developed to allow evaluation of seismically-induced piping failures for assessment of internal flooding scenarios. The spatial model was developed in SolidWorks software.

The spatial model of the building represents two switchgear rooms and adjacent battery rooms in the service building of a representative/generic 3-loop pressurized water reactor (PWR). The switchgear rooms and adjacent battery rooms contain critical and sensitive electrical equipment that provide DC power to safety systems required for safe shutdown following a seismic event. This critical equipment may be affected by either direct spray or water accumulation.

Center for Nuclear Energy Facilities and Structures (CNEFS) at NC State University converted the spatial model of fire suppression system provided by SC Solutions to an analytical nonlinear FE model in Open System for Earthquake Engineering Simulation in order to perform the seismic fragility analysis of the fire suppression system. A key component of the model is the modelling of the threaded joints as nonlinear rotational springs. The moment -rotation relationships at these joints are available from existing experimental data. Previous research at CNEFS in conjunction with MCEER-Buffalo had focused on conducting experimental tests on piping T-Joint components of different diameters. The T-joints were observed to undergo cyclic degradation in strength and stiffness under cyclic loading.

4.2.2.2   Fire Suppression Piping System

The spatial model for the fire suppression system provided by SC Solutions consisted of piping in the switchgear and battery rooms for the service building. These systems together comprise 6-inch vertical water supply standpipes, overhead 4 inch main lines that convey water to the smaller 1.5-inch and 1.25-inch branch lines.

The sprinkler-heads are located on the branch lines. The fire suppression system for the two adjacent switchgear rooms is an integrated system and is supplied by three standpipes. The fire suppression system is supported by 3ft. long hanger supports attached to the ceiling slab. The placement of the hangar supports is generally at every 16 ft. along the 4-inch main line, at the location of each sprinkler-head unless sufficiently close to hangers on the main line, and where intersecting lines or long unsupported spans warrant additional hanger supports.

The pipes are of varying schedules, including Schedule 40, Schedule 80 and Schedule 160.

For the switchgear rooms, there is one main 4-inch line running along their length. The span length of the smaller branch lines coming off the main 4-inch line is between 8 – 18 ft.

4.2.2.3 Key Observations/Points in Modelling of the Fire Suppression System

- Each of the battery rooms has its own standpipe and piping and sprinkler system. This system is not connected to the main fire suppression system in any way, and thus, is essentially decoupled. Thus, the main piping system and battery room piping system are modelled separately.

- Since the experimental data (moment-rotation relationships at the threaded T – Joints) is available for only the 1, 2 and 4-inch Schedule 40 pipes, all the 1.25-inch and 1.5-inch pipes are converted to 1-inch and 2-inch piles, respectively.

- The three vertical water supply standpipes are connected at the top as well as the bottom floor slabs. Hence, they are considered to be anchored – fixed in all 6 degrees of freedom, at these locations.

- Connections at the joints have been modelled as nonlinear rotational springs. Thus, connections at every T-Joint have been modelled by 3 nonlinear rotational springs and the connections at every 4-way cross, have been modelled by 4 nonlinear rotational springs. This model is valid for bending of the pipes in the horizontal plane only.

- The rotational springs for hysteretic behavior are characterized by models in *OpenSees*. The hysteretic behavior of nonlinear springs for 1 inch piping is characterized by yield strength M_y, initial stiffness K_1, hardening stiffness K_2, and parameter R, which controls the transition from elastic to plastic branches, as shown in Figure 53. The isotropic hardening parameter defines the increase of the compression or tension yield envelope as a proportion of yield strength after a plastic strain. The material model used is *Giuffré-Menegotto-Pinto Model* [2X].

- The hysteretic behavior of T-joint connections in 2 inch and 4-inch piping is characterized by a material that represents a "pinched" moment-rotation response which is modelled using a moment-rotation envelope [3X]. Figure 54shows the experimental v/s analytical results under cyclic loading condition, for a 2-inch T-joint, exhibiting the "pinched" behavior. The cyclic strength and stiffness degradation properties are determined in this model by considering stiffness degradation during unloading and reloading and strength degradation from the test data.

    The pipe connections to walls are modelled as anchors (fixed in all 6 degrees of freedom).

- Modal analysis after the completion of the modelling indicates that the piping system is very flexible. This is due to the absence of any lateral restraints at the locations where the hangers are meeting the piping system. Usually, the braces in a piping system offer lateral restraints, but this piping system is not braced at any location as provided in the spatial model. The frequencies of the first 10 modes of the piping system are given in Table 12which shows that the natural frequencies are relatively very small and the piping is extremely flexible which is unlike typical piping in nuclear plants.

- Lateral restraints are added in the piping system as an improvement of the spatial model which in turn help to increase the natural frequencies and bring them closer to the typical values observed in nuclear plants. These lateral restraints are added at all the hanger locations. In principle, each hanger is replaced by a bracing that provides lateral as well as vertical restraint. Figure 55 shows the location of these lateral restraints.

- As expected, the piping system becomes stiffer after the addition of these lateral restraints, with the natural frequencies given in Table 13.
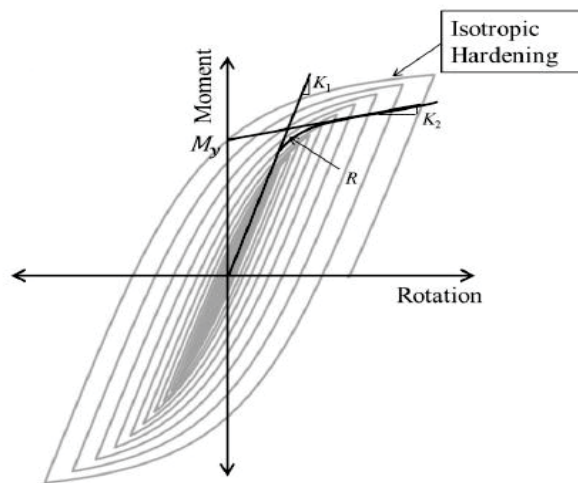
Figure 53.   One-Inch Rotational Spring Model.
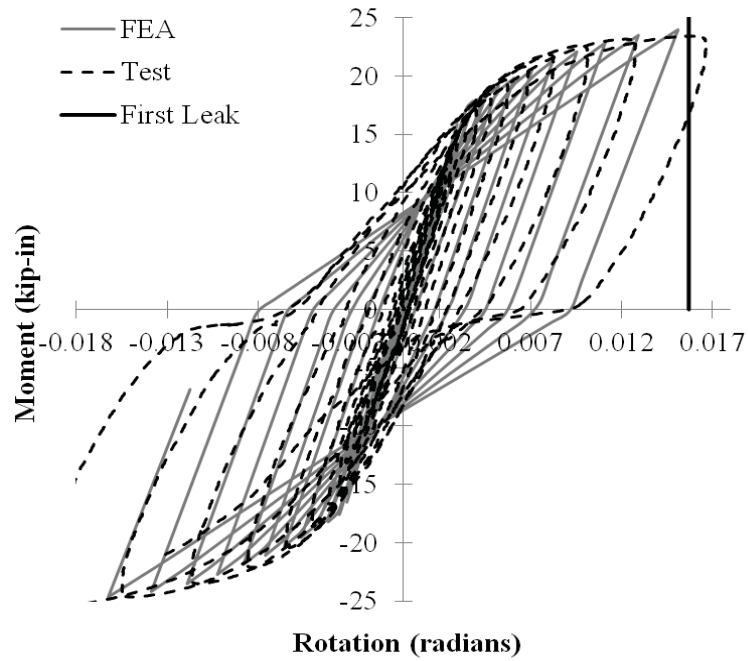
Figure 54. Experimental versus analytical results under cyclic loading condition

Table 12. Frequencies of the piping system without lateral restraints.

Mode	Frequency (Hertz)
1	0.122
2	0.1255
3	0.4521
4	0.4803
5	0.635
6	0.677
7	0.77126
8	0.787
9	1.09
10	1.14
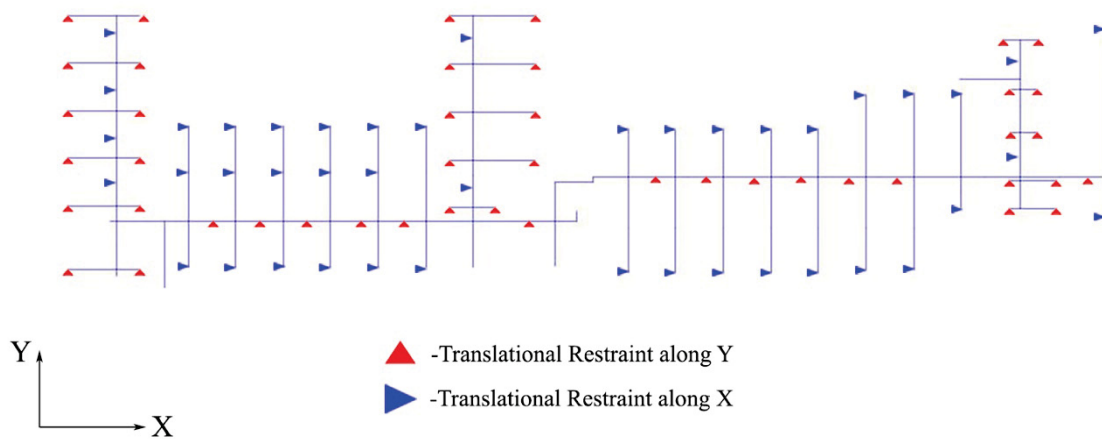
Figure 55.   Lateral restraints on the piping system.

Table 13. Frequencies of piping system with lateral restraints

Mode	Frequency (Hertz)
1	2.415
2	3.413
3	3.433
4	3.472
5	3.631
6	4.144
7	4.979
8	5.076
9	5.385
10	5.896

4.2.2.4   Leakage locations on piping system

Leakage locations on piping system for sample runs

The piping system is analyzed for earthquake time history runs normalized to increasing values of PGA in the X direction, to determine the leakage locations. The details of the earthquake record chosen are as shown in Table 14.

Table 14. Input earthquake station and record information.

Category	Record data
Location	Parkfield

Date	6/28/1966
Station	Cholame - Shandon Array #12
Direction	Horizontal, 50 degrees
Units of acceleration	9.81 m/s^2
Number of points	4430
Time interval	0.01s

The locations of damages at different PGA levels are indicated in Figure 56 to Figure 58.
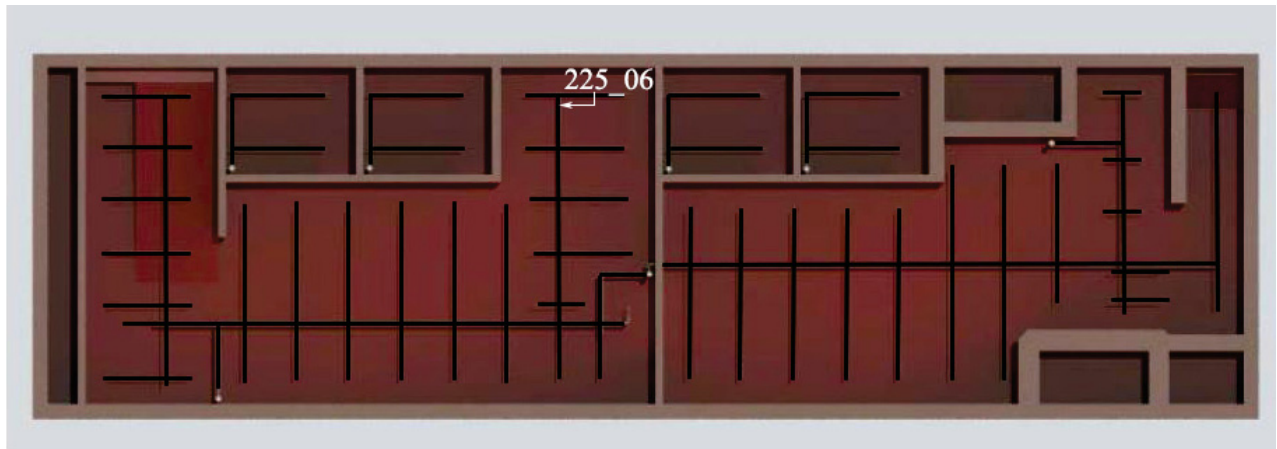
Figure 56.   Damage locations for Parkfield earthquake record at 0.3g.
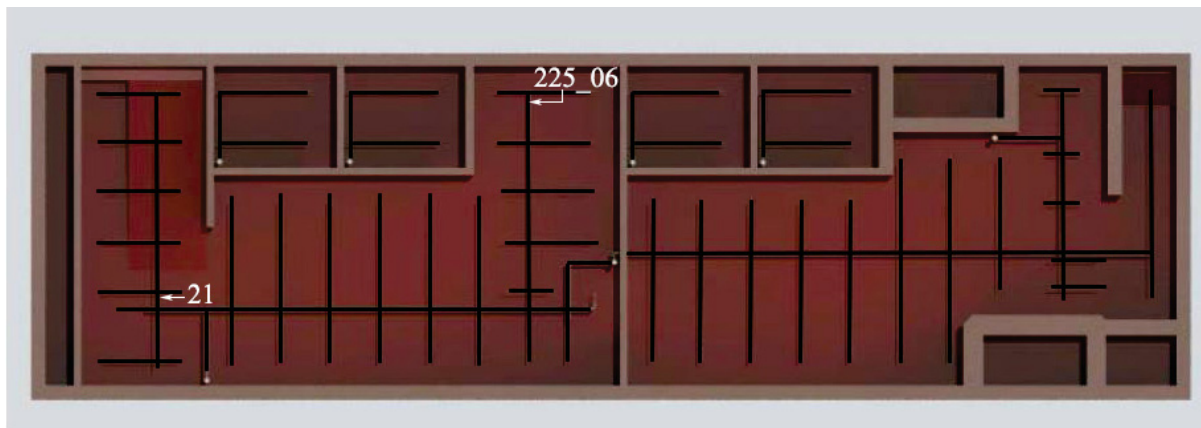
Figure 57.   Damage locations for Parkfield earthquake record at 0.5g.
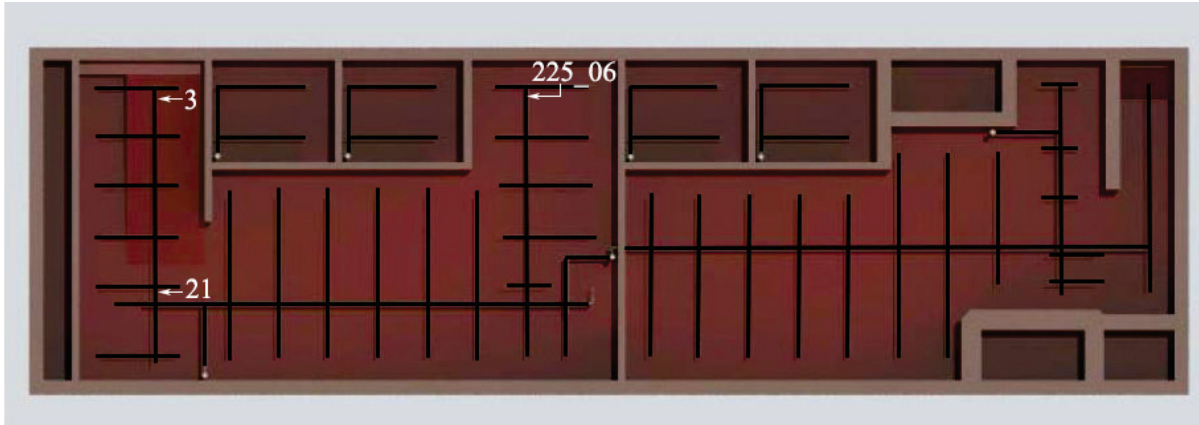
Figure 58.   Damage locations for Parkfield earthquake record at 1.0g.

Leakage locations on piping system for the acceleration records provided by INL

After the completion of the sample runs, the piping system is analyzed for the time histories provided by INL, both in the X and Y directions. The PGAs are normalized from 0.3g to 1.5g at intervals of 0.1g. There were a total of 32 time histories in X and Y directions respectively, implying a total of 416 runs in each direction. For the first time history in the X direction, the first damage is observed at a PGA of 0.297g. The locations of damage are increasing in number with the increasing values of PGA. All the damages are for 1-in. pipes. Figure 59 indicates the locations of damages for PGA levels up to 1.5g, for input in X direction. For the time history runs in the Y direction, two locations of damage are identified for a PGA level up to 1.5 g. The damages are for 2-in. pipes. Figure 60 indicates the locations of damages for PGA levels up to 1.5g, for input in the Y direction.
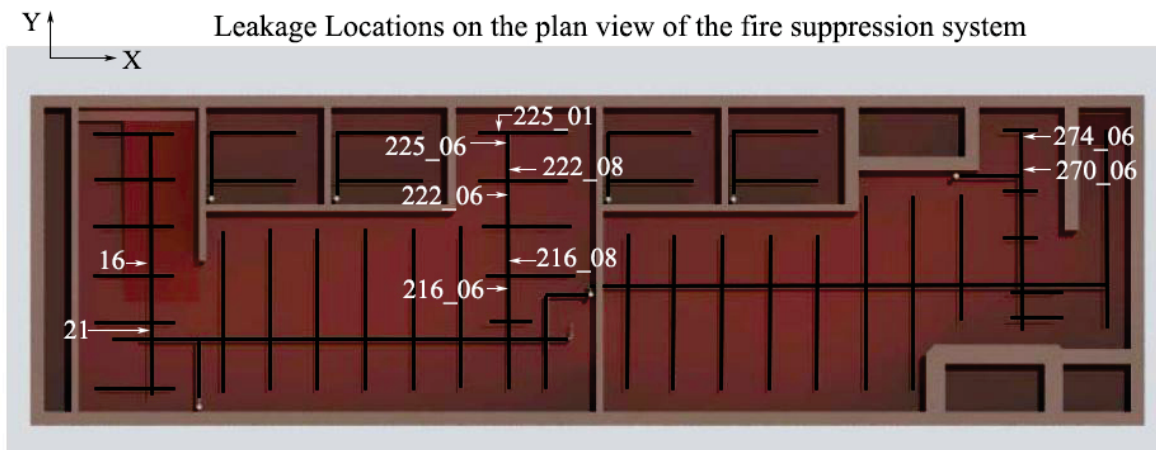
Figure 59.   Leakage locations for PGA levels up to 1.5g with X direction input.
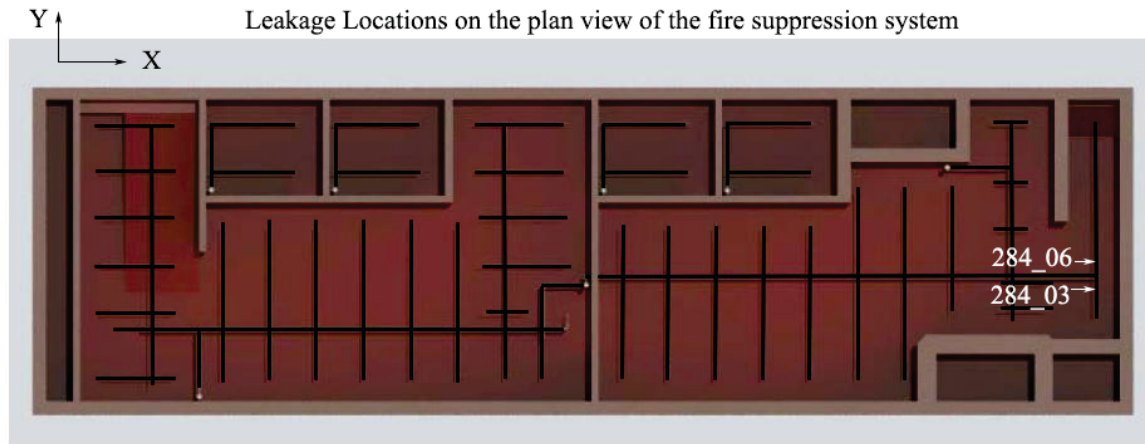
Figure 60. Leakage locations for PGA levels up to 1.5g with Y direction input

4.2.2.5 *Damage States Considered for Seismic Fragility Assessment*

After the identification of locations of failures, seismic fragility analysis is carried out, in order to generate the seismic fragility curves at the failure locations. Figure 61 gives the ASME criteria for characterization of limit state. Figure 61 and Table 15 indicates the three damage states considered for seismic fragility assessment.
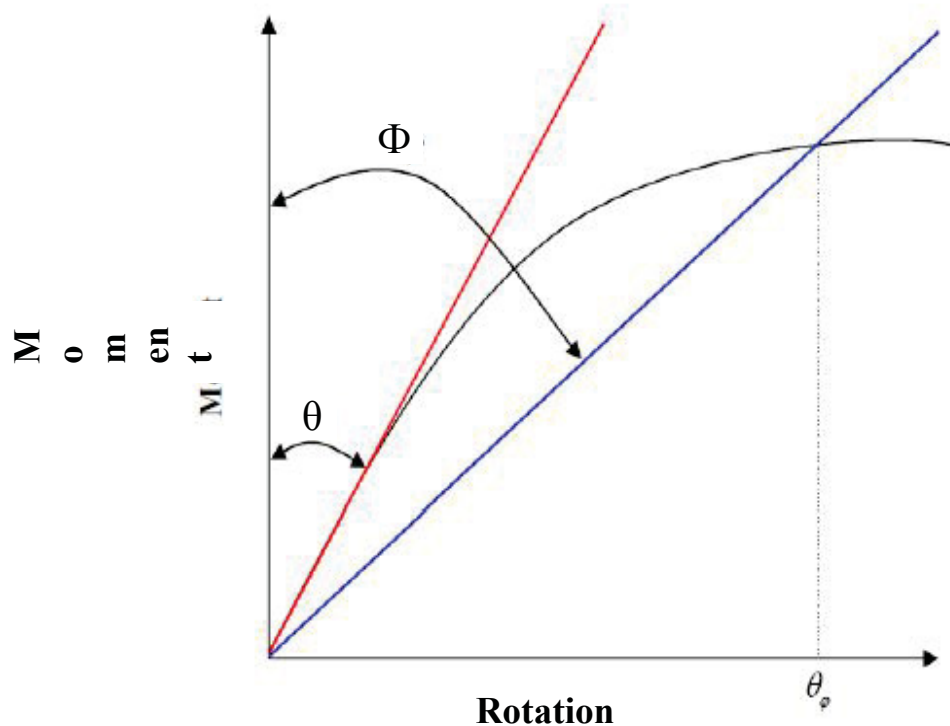
Figure 61. ASME criteria for characterization of limit state.

Table 15. Damage states for fragility assessment.

Damage State	Criteria
Minor	$\Phi=2\theta$
Moderate	$\Phi=2.5\theta$
Severe	$\Phi=3\theta$

4.2.2.6   Seismic Fragility Curves

Figure 62, Figure 63 and Figure 64 show the seismic fragility curves for minor (first leak), moderate, and severe damage in the X direction, respectively. Table 16, Table 17, and Table 18 provide the fragility function parameters for minor, moderate, and severe damage, respectively, for loading in the X direction.

Figure 62.   Seismic fragility curves for first leak with X direction input.

Figure 63.   Seismic fragility curves for moderate damage for X direction input.

Figure 64.   Seismic fragility curves for severe damage for X direction input.

Table 16. Parameters of the fragility curves for first leak with X direction input.

Joint Number	Median	Lognormal Standard Deviation
225_06	0.4196	0.1653
21	0.6296	0.1480
222_08	0.7226	0.1353
225_01	0.7827	0.1397
222_06	0.8424	0.1053
16	0.9392	0.1167
216_08	0.8212	0.1356
216_06	0.7590	0.1850
270_06	1.2037	0.1429
274_06	1.2009	0.1345

Table 17. Parameters of the fragility curves for moderate damage with X direction input.

Joint Number	Median	Lognormal Standard Deviation
225_06	0.5928	0.1432
21	0.8022	0.1235
222_08	0.9916	0.0906
225_01	1.2059	0.128
222_06	1.1675	0.1277
16	1.1821	0.0869
216_08	1.1154	0.1004
216_06	1.0873	0.2072
270_06	1.3918	0.1476
274_06	1.3715	0.1241

Table 18. Parameters of the fragility curves for severe damage with X direction input.

Joint Number	Median	Lognormal Standard Deviation
225_06	0.7361	0.1474
21	0.9697	0.1545
222_08	1.184	0.1216
225_01	1.6601	0.1093
222_06	1.4924	0.1344
16	1.5305	0.0531
216_08	1.4592	0.1494
216_06	1.4218	0.1995
270_06	1.5105	0.1643
274_06	1.5105	0.1643

Seismic fragility curves for loading in the Y direction

Figure 65, Figure 66, and Figure 67 show the seismic fragility curves for minor, moderate, and severe damage in the Y direction, respectively. Table 19, Table 20, and Table 21 provide the fragility function parameters for minor, moderate, and severe damage, respectively, for loading in the Y direction.
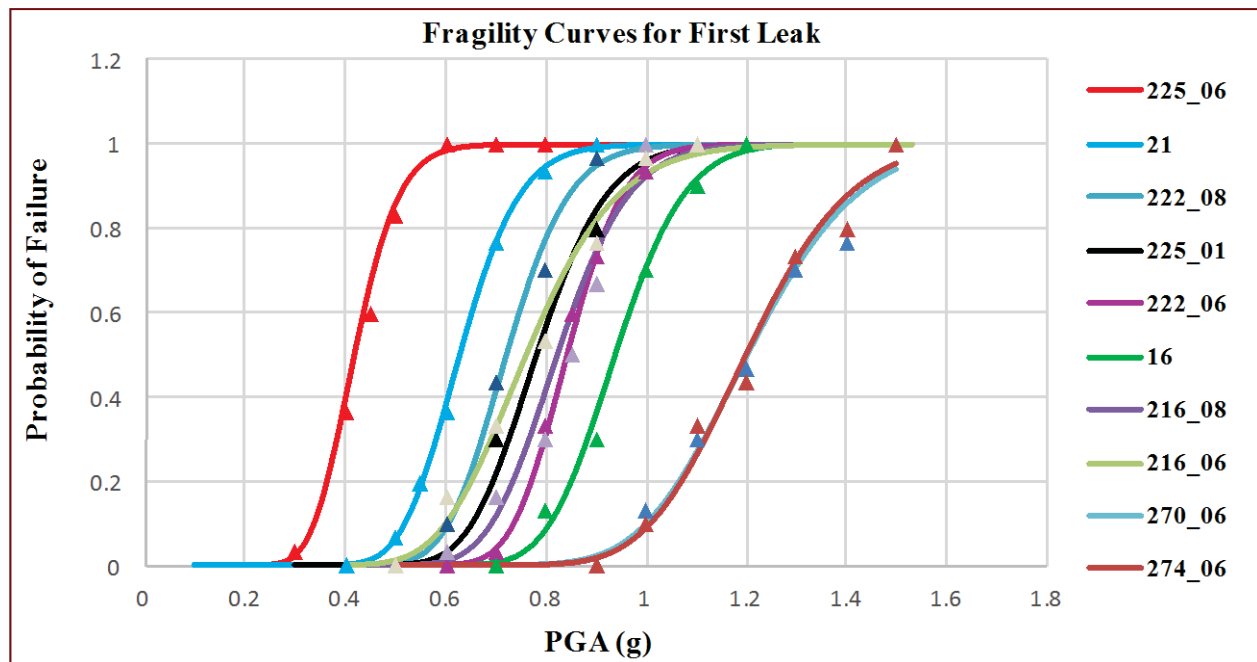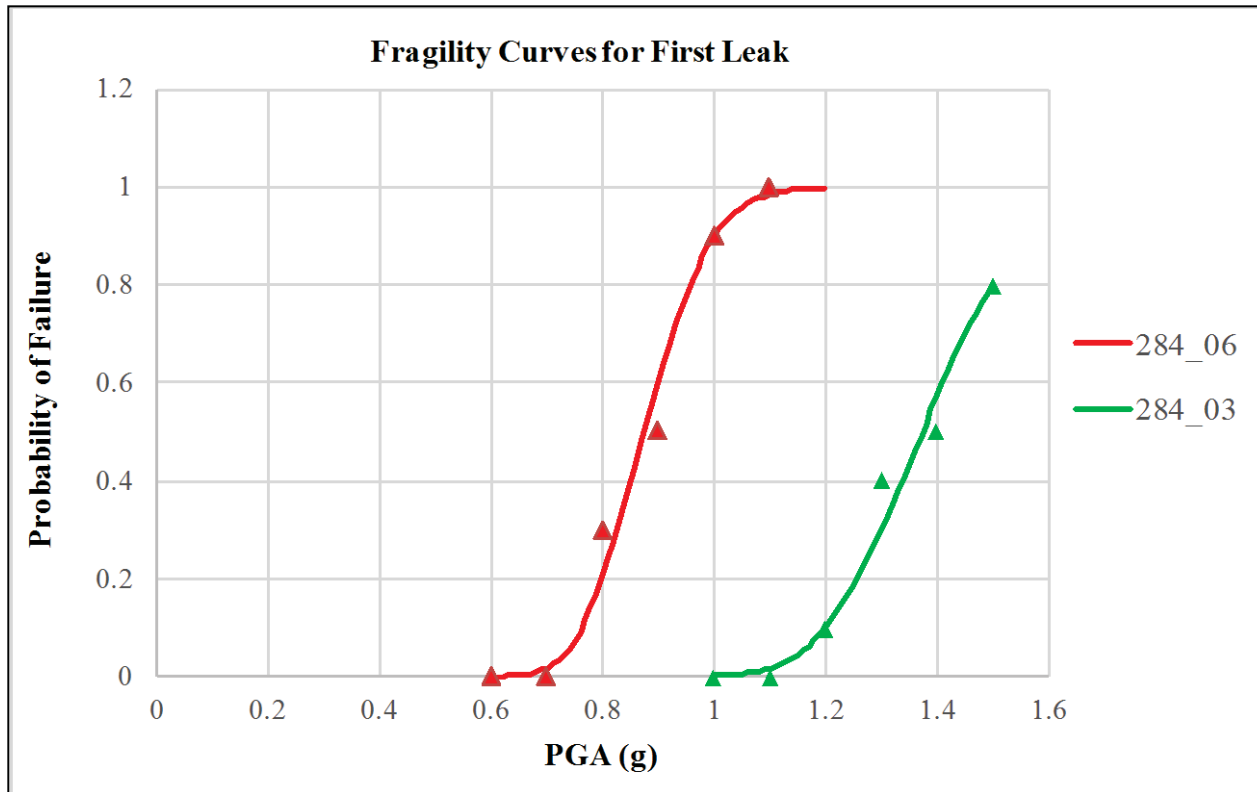
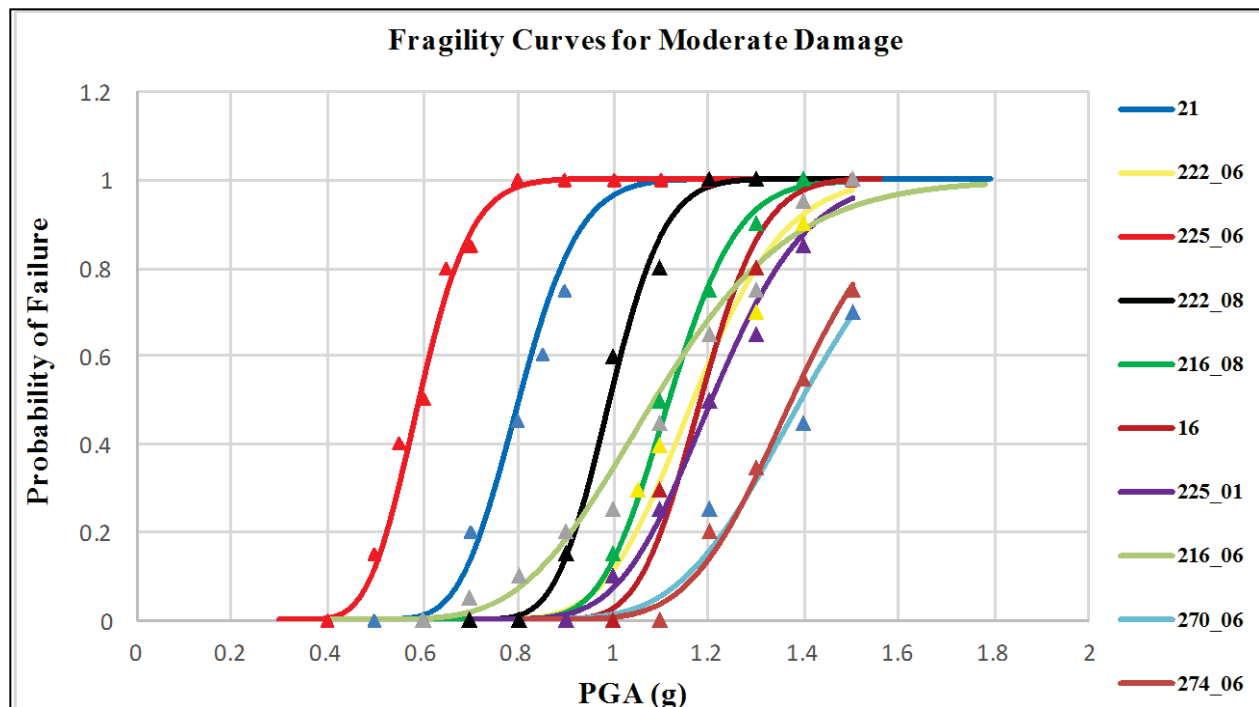Figure 65.   Seismic fragility curves for minor damage for Y direction input.
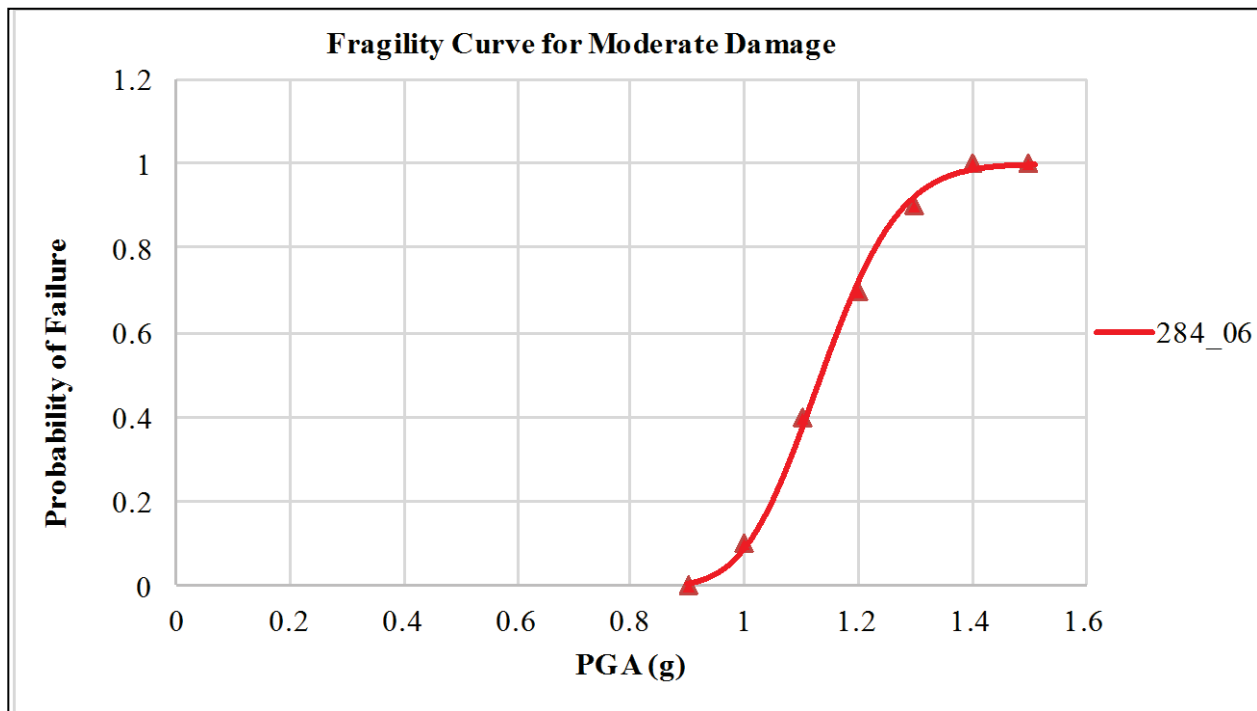
Figure 66.   Seismic fragility curves for moderate damage for Y direction input.
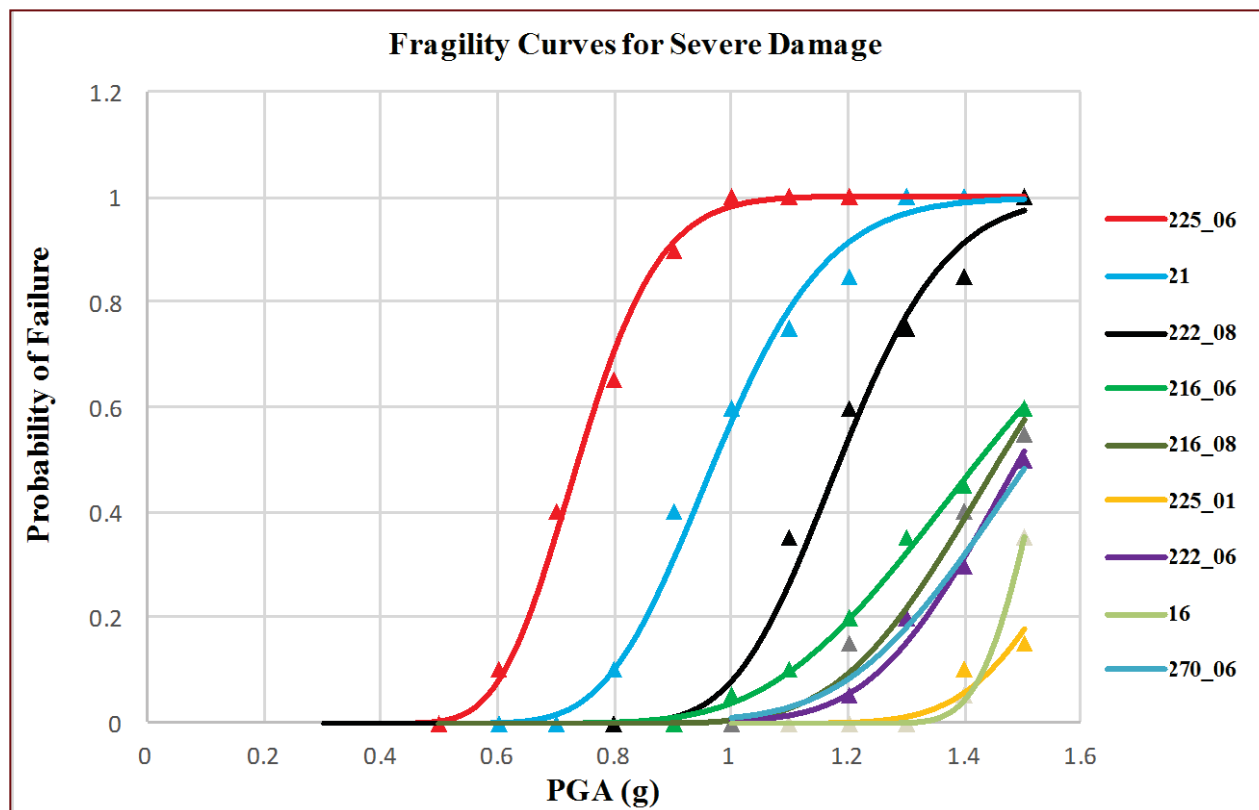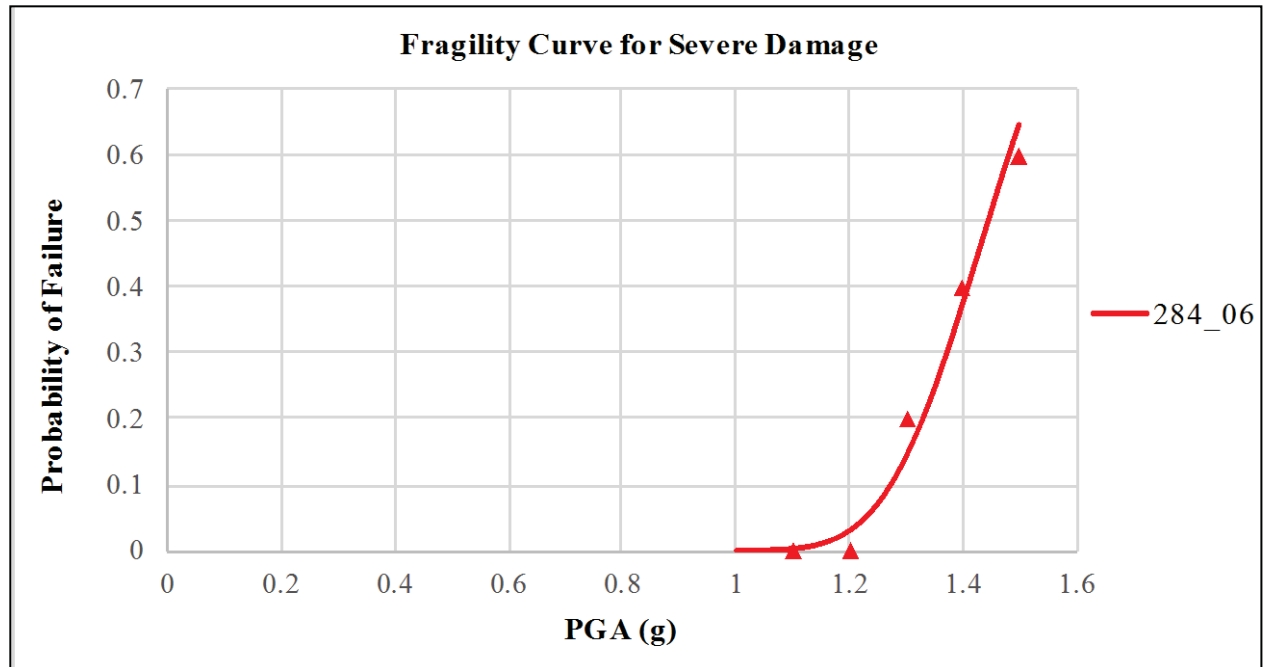
Figure 67.   Seismic fragility curves for severe damage for Y direction input.

Table 19. Parameters of the fragility curves for minor damage with Y direction input.

Joint Number	Median	Lognormal Standard Deviation
284_06	0.8744	0.1063
284_03	1.3733	0.1052

Table 20. Parameters of the fragility curves for moderate damage with Y direction input.

Joint Number	Median	Lognormal Standard Deviation
284_06	1.135	0.0943

Table 21. Parameters of the fragility curves for severe damage with Y direction input.

Joint Number	Median	Lognormal Standard Deviation
284_06	1.4458	0.0991

Either of the two formulations can be used in Excel, to get a probability of failure corresponding to a PGA value (both give the same results):

- LOGNORM.DIST(pga, ln(Median), Lognormal Standard Deviation, TRUE)

93

- NORM.DIST(ln(pga), ln(Median), Lognormal Standard Deviation, TRUE)

4.2.2.7   Explanation of Failures

The response spectra and the mean spectra of the response of the piping system for the 32 earthquake records in the X direction is shown in Figure 68. The peak of the repose spectra for the 32 time histories occurs in the range of 2.5 – 3.2 Hz. The first two modes of the piping system occur at 2.415 and 3.413 Hz, respectively, in the vicinity of the peak of response spectra. The modal participation factor in the X direction for first two modes is also high (0.28 and 0.369, respectively). It is in these first two modes that we observe the excitation of the branch containing the maximum amount of failure locations (see Figure 69 and Figure 70). The failure at the joints 225_06, 222_06, 222_06, 222_08, 216_06 and 216_08 can be attributed to bending of the pipe branch in the X direction, which is causing large rotations at the joints. Fragilty surfaces for these joints are provided in Appendix C.
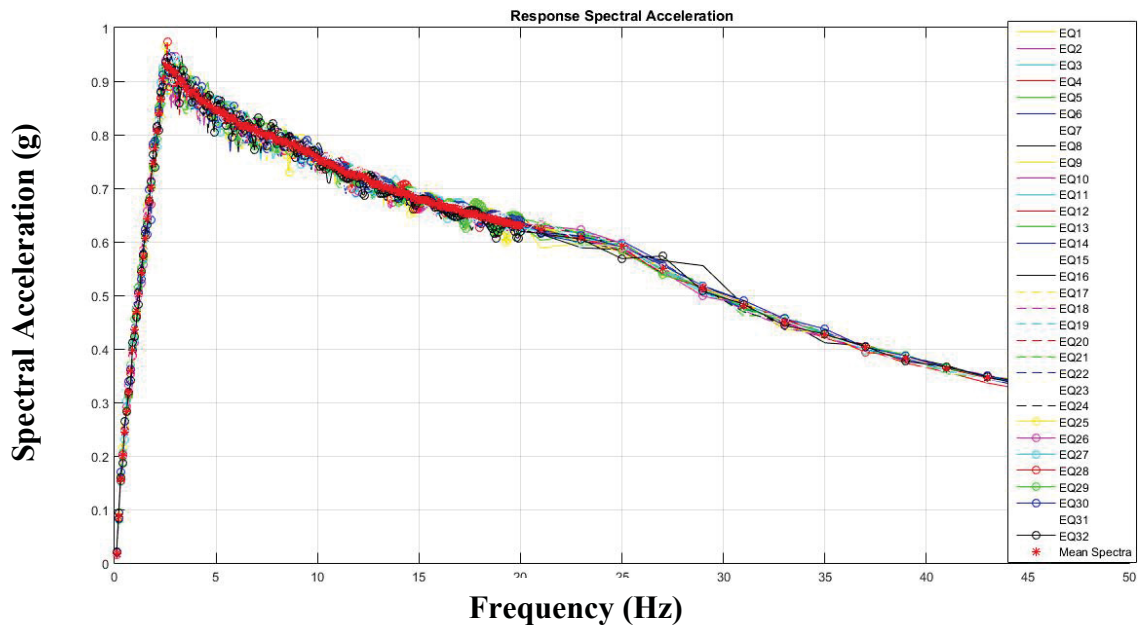
Figure 68.   Response Spectra of the 32 time histories in the X Direction.
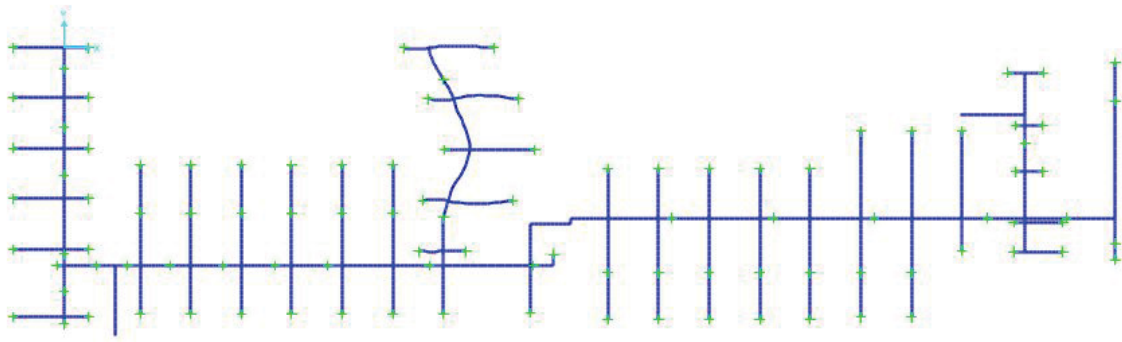
Figure 69. Mode 1 of piping system – Excitation of branch containing the maximum number of failure locations.
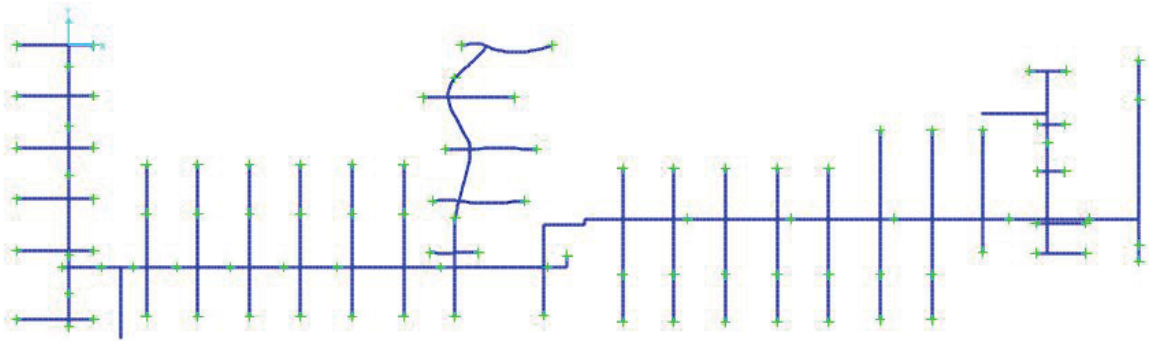
Figure 70. Mode 2 of piping system – Excitation of branch containing the maximum number of failure locations.

4.2.2.8   Effect of Time of Failure on Fragilities

Figure 71. Layout of the piping system.

Up to now, fragility analyses have been conducted without considering the effect of the time of failure on fragilities. However, the layout of the piping system encourages evaluation of the impact of the time of failures of the joints. Results of the seismic fragility analysis indicate that Joint 225_06 is more fragile than Joint 216_08 (Figure 25). However, for a certain earthquake scenario, Joint 216_08 may fail at an earlier time, which would lead to no leakage at Joint 225_06. Thus, Joint 225_06 may fail, but will not leak under such a scenario. As a result, the flooding simulation scenario is altered. Hence, it is important to consider the effect of time on fragilities. Figure 72 illustrates the difference between a time-dependent and time-independent fragility curve for a joint.

Figure 73 illustrates the fragility surfaces for an analyzed joint. It can be observed that as we proceed along the time axis, the probability of failure increases. The values of probability of failure reach values corresponding to a time-independent fragility curve towards the end of the time axis. Fragility surfaces for a number of joints analyzed are provided in Appendix C.
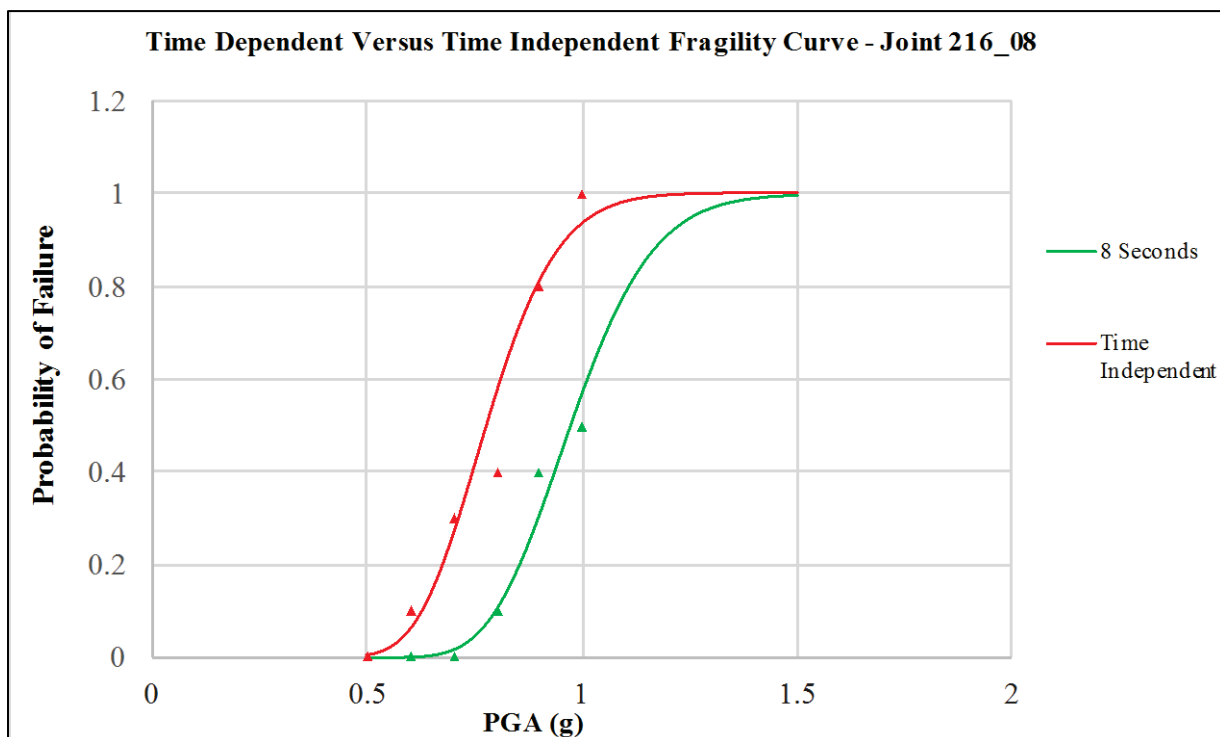
Figure 72.   Comparison of time-dependent versus time-independent fragility curves.

225_06
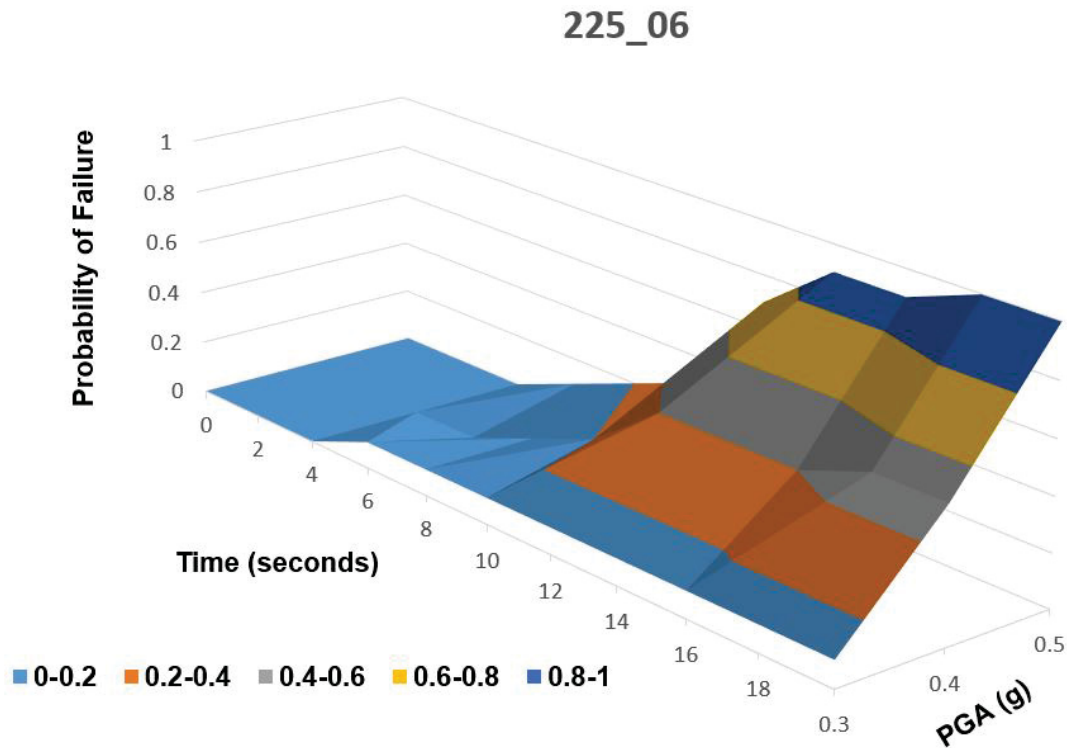
Figure 73.   Example time-dependent fragility surface

4.2.2.9   Next Steps/Future Work

The next steps in the project include the following:

- Generating time histories at different floor levels from the building model.
- Generating time independent fragility curves for time histories at different floor levels, and exploring the effect of the location of the piping system at different floor levels, on the fragilities.
- Exploring different ageing and degradation models and incorporating the same in the current model of the piping system.
- Generating time dependent fragility curves and fragility surfaces, for the time histories at different floor levels.
- Investigating the effect of ageing on fragilities.

4.2.3   Probabilistic Risk Assessment

Two probabilistic models were used in this development: a traditional SAPHIRE PRA model and a dynamic PRA model implemented in EMRALD.

4.2.3.1 Sampling Method for Seismic Motions Used for Probabilistic Risk Assessment Demonstration

The peak ground acceleration (PGA) is sampled from a seismic hazard curve, which gives the annual frequency of exceedance as a function of the PGA. The seismic hazard curve used in Section 4.4 for ASPRA (referred to as hazard curve 2) is used for sampling. This hazard curve is reproduced in Figure 74, below.
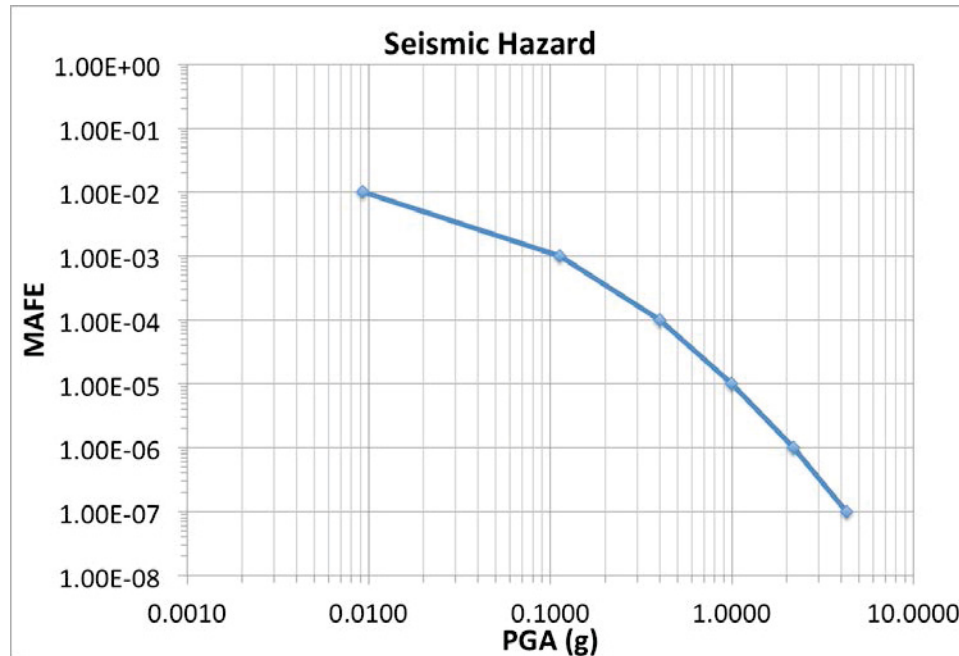
Figure 74.   Seismic hazard curve used for sampling.

Figure 74 shows that the seismic hazard curve ranges between PGA values of 0.01g and 4.3g, which correspond to annual frequencies of exceedance of 1E-02 and 1E-07, respectively. The PGA is sampled randomly using a uniform sampler as follows:

- The Y axis of the seismic hazard curve above is first converted to annual frequency of non-exceedance, so that the resultant curve represents a cumulative probability distribution. This distribution ranges from 0.99 (1E-02) to 0.999999 (1E-07) for the same range of PGA values.

- A random number is then picked between these probabilities of non-exceedance using a uniform distribution based sampler. For each such random number the corresponding PGA is calculated from the cumulative probability distribution through linear interpolation.

- This value of PGA is used as the random PGA sample.

This method then is verified by first calculating several samples of the PGA, and then calculating the frequency of non-exceedance of each sample. The frequencies of non-exceedance when plotted against the PGA samples, should match with the cumulative probability distribution calculated from the seismic hazard curve. Figure 75 presents two such verification examples for 100 samples and 1000 samples. The figure clearly shows that the frequencies of non-exceedance of these samples match exactly with those calculated from the seismic hazard curve.

| a. 10,000 samples | b. 1,000,000 samples |
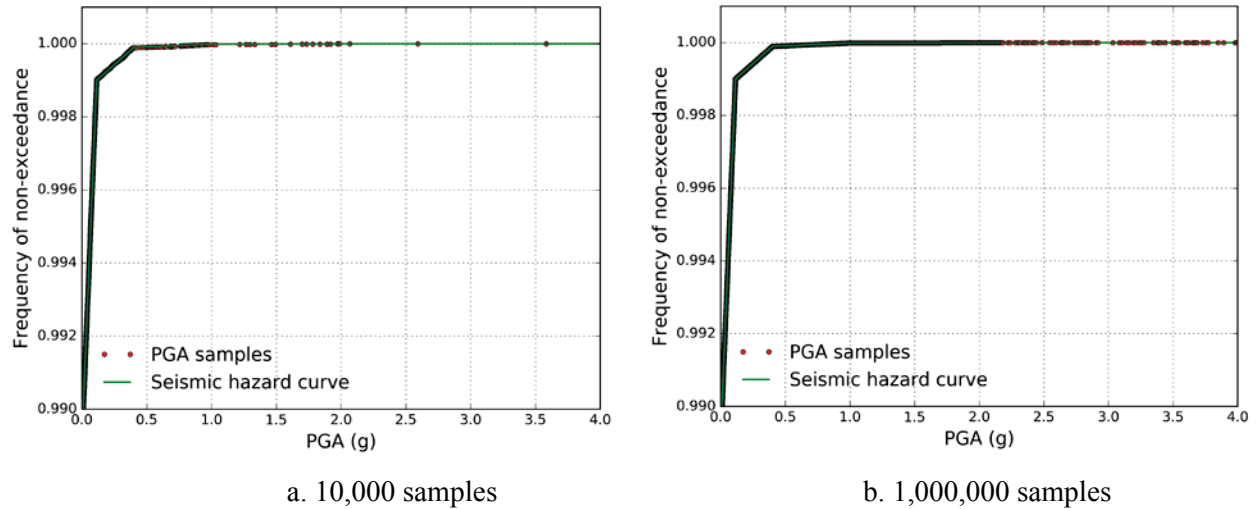
Figure 75.   Verification of the peak ground acceleration sampling method

4.2.3.2   SAPHIRE Model

A basic generic PRA model was developed using SAPHIRE. This model contains only a few systems necessary for analyzing those areas affected by the seismic or flooding scenario and the main components/systems analyzed in the TH simulation. Other required systems are stubbed out with a general overall failure rate that can be expanded to full systems in the future. This model contains the failure methods and rates for key components and results provide a baseline to verify the dynamic model. The fault trees listed in Table 22 are the main systems in the SAPHIRE model.

Table 22. SAPHIRE model for the main systems.

Name	Description
AFW	Loss of auxiliary feed-water (AFW)
DGEN	Loss of diesel power
HPI	HPI flow insufficient
LOOP-LOCA	Conditional loss of offsite power given LOCA
MFW	Loss of MFW
NLOSP	Seismic Loss of Site Power
OEP	Loss of offsite power
PASS	Pass-through for transients
RHR	Residual heat removal
RHR-L	Long-term RHR flow - large LOCA
RHR-S	Long-term RHR flow - small LOCA
RPS	Reactor S/D

Name	Description
SEC	Secondary cool-down SG_PORV
SVC	Safety valves close
SVO	Safety valves open
UDC-CTRLPWR-1	DC control power train 1
UDC-CTRLPWR-2	DC control power train 2
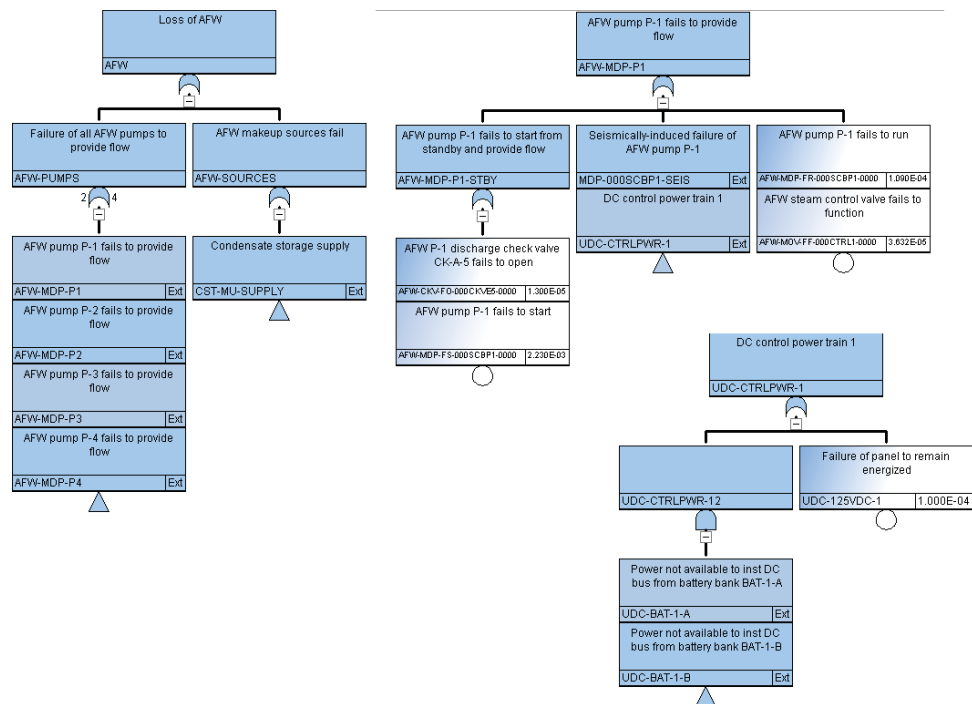
Figure 76.   Main fault trees in the SAPHIRE model.

Seismic capabilities for susceptible components have been added using a sub tree containing bin and flag set combinations. For each seismic bin, a basic event with an appropriate failure rate is combined with a house event that is triggered by a flag set (see Figure 77). When solving for a given seismic input, the correct failure rate propagates up the sub tree, contributing to the overall failure rate. The SAPHIRE model contains 10 different seismic bins, other pieces of this test only contain 3 bins, in these cases, failure values from bins 2, 5, and 8 will be used.
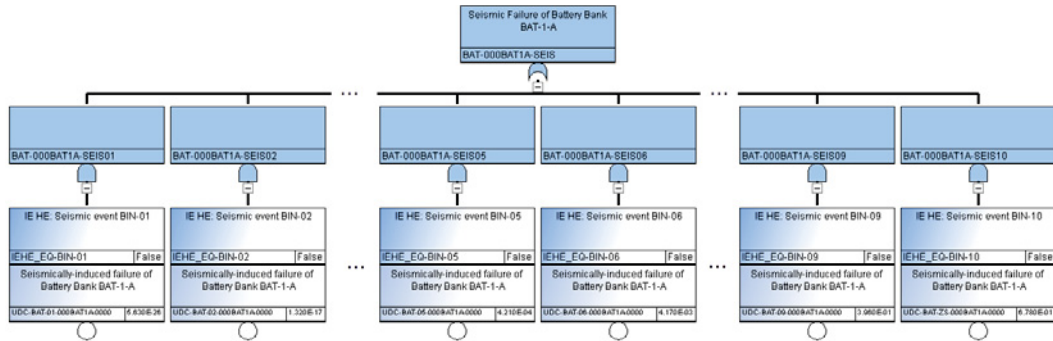
Figure 77.   Example of varying seismic failure rates by using a flagset

Because there is very little empirical data for component failure rates due to seismic events, arbitrary but logical values are used. This will due for demonstration purposes, and as more data is compiled, more accurate values can be applied.

Three main event trees are modeled including loss of off-site power (LOOP), SBO, and Transient.   Sequences are either OK or lead to core damage (CD).   In most cases if CD is reached then RELAP will be used for further calculations. A combination LOOP and SBO are used to develop the plant response diagram for the dynamic PRA model.
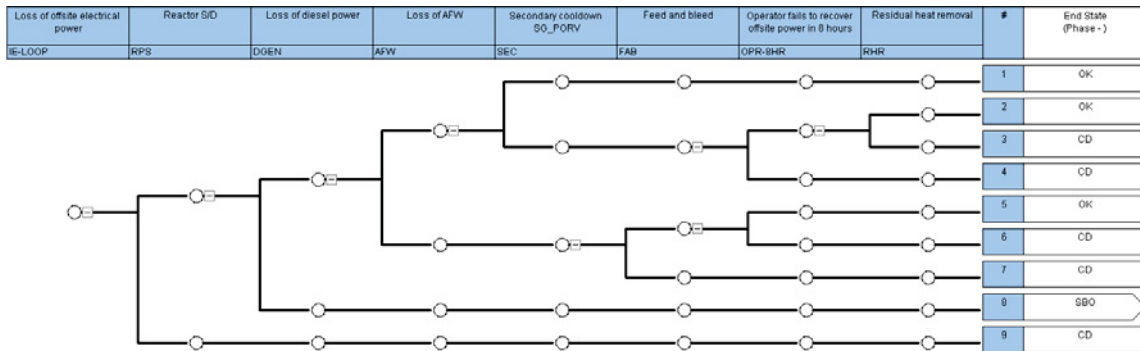
Figure 78.   Loss of off-site power event tree.
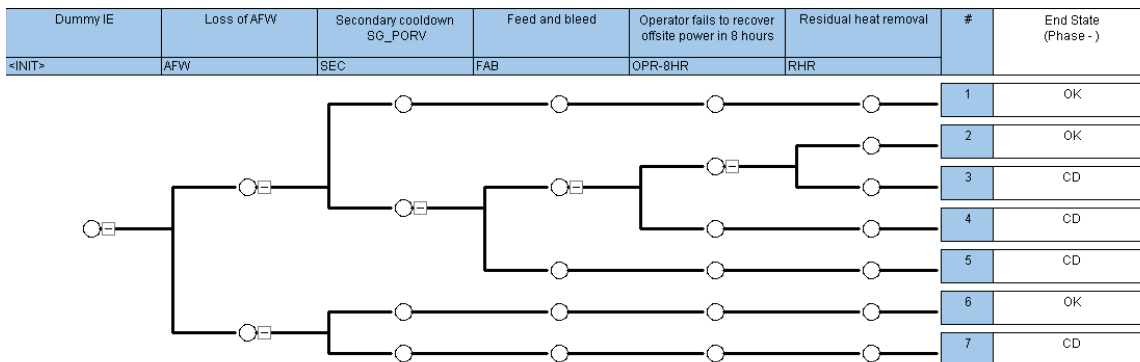
Figure 79.   Station blackout event tree.

101

4.2.3.3   *EMRALD Model*

The dynamic PRA model was developed using EMRALD and is based on the SAPHIRE model. The core of the model is equivalent to the SAPHIRE model with additions to handle dynamic changes depending on results from the seismic event on the piping structure or events in the 3D flooding simulation.

A logic evaluation similar to the fault trees in SAPHIRE is done in EMRALD. The Boolean logic with component inputs is evaluated when the state of any of the inputs changes. Unlike traditional PRA model, which uses event tree to graphically represent accident sequences, there is no sequentially depiction of the responses of the systems and operator actions to an initiating event. The accident sequences are implicitly represented in the plant state diagram with the flow paths between the start states with their initiating events, system or component states, and key/end states. For a more detailed description of the state-based PRA methods in EMRALD refer to Prescott, Smith and Samptah (2013).

The component seismic driven event probabilities are dynamically set depending on the sampled PGA value. The SAPHIRE model has 10 bins earthquake levels, since we only have 3 bins for the pipe failure values; we reduced the component seismic failure values to 3 bins as well. See appendix A for a list of component event failure values.

In order reduce the total computation time needed bounds were modeled for both the 3D simulation runs and the running of RELAP. An earthquake initiating event had to generate a PGA > 0.5 in order to be considered significant enough to effect the systems normal operations. Highly probable fuel failure conditions, given timing and failed events directly moved the simulation to fuel failure, without any RELAP evaluation and high probable success conditions moved directly back to normal operations. To maximize the value of each 3D simulation, repeated sampling of the RELAP inputs and runs was done. For each 3D simulation, 100 RELAP runs were attempted with varied "Early failure of the MCP seal" and operator recovery action times.

To reduce dynamic RELAP runs, pre run scenarios described in Section 4.2.5.3 were run. The script that preps for a RELAP run these results to further eliminate running known cases, running only the cases between the known bounds. Finally, each RELAP run result is stored into a matrix of input parameters, with 10 min bounds on time based items. Any subsequent RELAP runs matching the same matrix value will return the previously run result.

The EMRALD model starts in normal operations the only event being tested, from this state, is an earthquake driven LOOP event. The following possible transitions then take place, as show in Figure 80:

1. Normal_Op – The normal operation of the plant.

    Immediate Actions

    a. Reset the systems back to initial conditions.

    Conditional Events

    a. 24HrMission_Time – After 24 hours, terminate this run, no imitating event occurred.
    b. IE_LOOP_EQ – The earthquake that triggered a LOOP occurred so set the PGA and move to LOOP_EQ_OCCURED.

2. LOOP_EQ_OCCURED – An earthquake that triggered a LOOP occurred.

    Immediate Actions

a. Eval_Pipe_Failures – Sample on the EQ and determine if any.

b. Start_SBO_Eval – Start evaluating any systems related to SBO.

Conditional Events

a. RPS – If Reactor S/D equipment fails to initiate move to Core_Damage.

b. DGEN_Fail – If the diesel generators fail, move to SBO.

3. SBO – (Key State) Station black out, the only power is battery backup.

Immediate Actions

a. Goto_AC_Failed – Add AC_Failed to the current state list.

Conditional Events

a. Pipe_Rupture – If there is a pipe rupture then move to Running_3D_Sim.

b. No_Pipe_Ruptures – There are no pipe ruptures move to Loop_Eval.

4. Running_3D_Sim – 3D simulation is needed to evaluate components due to possible flooding.

Immediate Actions

a. Start_3D_Sim – Start the 3D simulation.

b. Set_Pipe_Fail_Vals – Set the location, and flow rate of the any pipe failures that occurred.

Conditional Events

c. OP_FW_Rec – Operator shuts down the fire water system so stop the 3D simulation by going to Stopping_3D_Sim.

d. AFW and SG_PORV – The system that are affected by the simulation have failed, no more 3D simulation is needed, so move to Stoping_3D_Sim.

5. Stopping_3D_Sim – (Key State) The 3D simulation is no longer needed, so shut it down.

Immediate Actions

a. Stop_3D_Sim – Send a message to stop the 3D simulation.

b. Goto_Loop_Eval – Move to the Loop_Eval state.

Conditional Events - None

6. Eval – The starting point for repeatedly evaluating the rest of the systems.

Immediate Actions

a. Start_Sys_Eval – Start sampling and evaluation of the main systems.

Conditional Events

a. AC_Recover and No_Key_Sys_Failures – AC power from offsite power or the diesel generators is recovered and there are no key system failures, so move to Rerun_Loop.

b. 2.5Hrs and AC_Recovery and Key_Sys_Failures – After 2 hours and the AC power is recovered and there are key system failures then move to Running_RELAP.

c. 13Hrs and No_AC_Recover – After 13 hours and if there is no AC power recovery then move to Fuel_Damage.

7. Running_RELAP – Conditions are met where there is possible fuel damage but further calculations are needed using RELAP.

    Immediate Actions

    a. Set_LGLeakRate – Sample and set if the RELAP simulation is to have a large leak rate.

    b. Set_RecTime – Sample and set the recovery time for RELAP where an operator is able to manually adjust the PORV.

    c. Inc_Loop_Cnt – Increment the counter indicating how many times RELAP was run for the current SBO event.

    d. Run and Process_RELAP – Modify the RELAP input deck with the failure time of any components or systems and run RELAP. If RELAP indicates damage add to Fuel Damage to the current state list. After running RELAP move to Rerun_RELAP_Loop.

    Conditional Events - None

8. Fuel_Damage – Fuel damage has occurred.

    Immediate Actions

    a. Inc_Fuel_Damage – Increment the fuel damage variable to keep track of how many time fuel damage occurs in the multiple runs for a given initiating event and 3D simulation.

    Conditional Events – None

9. Rerun_RELAP_Loop – Run RELAP 100 times for each EQ event causing SBO.

    Conditional Events

    a.   Loop_Cnt_LT_n – The Loop count is less 100 so run RELAP again.

    b. Loop_Cnt_EQ_n – The loop count is equal to the desired number so move to Normal_Op.

10. AC_Failed – Indicator that AC is currently in a failed state both offsite and diesel generators.

    Conditional Events

    a. AC_Recovery – Set the time that AC recovers due to recovery of offsite power, or diesel generator recovery.

11. AC_Recovered – Indicator that AC has due to recovery of offsite power, or diesel generator recovery.

    Immediate Actions - None

    Conditional Events – None

12. Done – (Terminal State) Exit this run of the EMRALD simulation.

    Immediate Actions - None

    Conditional Events – None
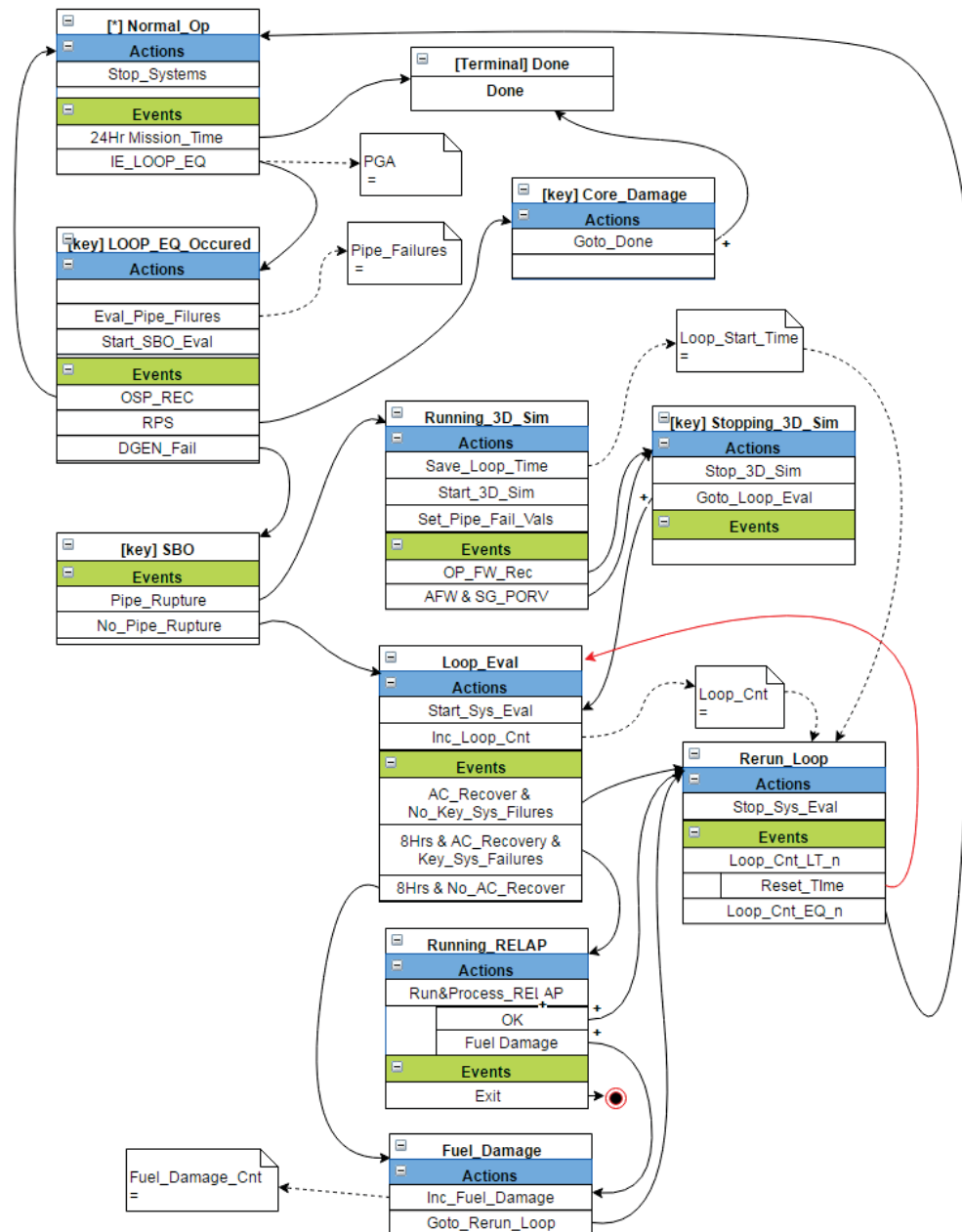
Figure 80. The Plant Response Diagram to calculate failure probabilities by coupling seismic analysis, dynamic probabilistic risk assessment, 3D simulation, and RELAP.

Several values such as RecTime, which are set during each EMRALD simulation, use a log normal curve distribution to determine a value. The PGA value is determined using dynamically executed code. This code does a random sampling over a linear interpolation from data described in Section 3.1. An independent sampling of this code was done to verify it matched that given in Section 4.2.3.1, before it was added to the model.

The EMRALD model is run numerous times, for each run if a "Key State" occurs; it is recorded along with and indicated variables such as Fuel_Damage_Cnt. Thus the probability of SBO occurring is the number of times SBO occurred divided by the total number of runs. For this scenario, the probability

of fuel damage is calculated by combining the probability of normal fuel damage and that determined by RELAP, using the following equation:

$$Fuel\ Damage\ Probability = \frac{Fuel\_Damage\_Cnt}{(Total\ Runs)} + \frac{\Sigma(\frac{\Sigma RFuel\_Damage\_Cnt}{100})}{Total\ Runs}$$

Each EMRALD system was tested against the SAPHIRE main or sub fault tree result for validation before being used in the overall plant response diagram.   Detailed information on EMRALD operations and options are not covered in depth, but can be obtained in Prescott, Smith, and Samptah (2013).

4.2.4   Flooding Analysis

The Neutrino tool described in Section 3.2 was used to setup and simulate the seismic driven flooding scenario. The structure layout and fire water piping is described in more detail in report INL-EXT-16-39353.

4.2.4.1   *Flooding Analysis Setup and Simulation*

For this demonstration the 3-D model of the two switchgear rooms constructed for the generic PWR are used as the rigid body structures for the Neutrino flooding model. This consists of a 3-D polygon model of a floor of the facility and other rigid objects representing components.

These critical components those susceptible to water damage, including four battery units, two 4kV switchgear units, two 125V DC distribution panels and four UPS units. Refer to report INL-EXT-16-39353 for more detail on the layout of these components and Section 4.2.3 for information on the effects of their failures on the systems.

Dynamic particle emitters are used to simulate a rupture from the water based fire suppression system. For this setup, only the top 10 pipe break locations were added to the simulation model. These location were determined by the seismic analysis described in Section 4.2.2. The flow rate of these particles is set dynamically by EMRALD before the simulation starts. A small break is set at 0.001 cm, a medium break is set at 0.003 cm, and a large break is set at 0.005 cm.
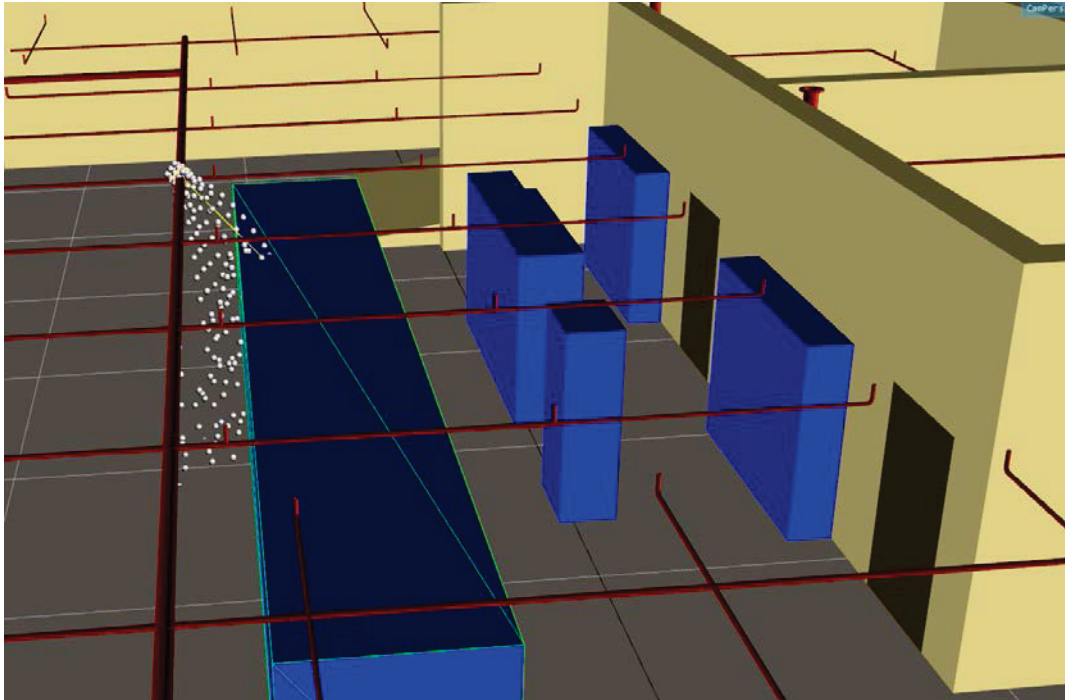
Figure 81.   Example of pipe fracture using Neutrino.

When the simulation is loaded, the desired events data is also loaded. This indicates what measurement field events are needed and are to be sent back to EMRALD. In this model each component has a failure for critical water height failure and a possible spray failure. As a simulation runs, it monitors fluid interaction with component measurement fields. If a component's failure criteria are met, a failure message is sent through the network communication to EMRALD.

Figure 82.   Neutrino measuring flood height at 0.248 meters.

4.2.4.2   Needed Enhancements

The setup and execution of this scenario illustrated needed capabilities in the simulation tool set. Although we can create a particle emitter with a given flow rate,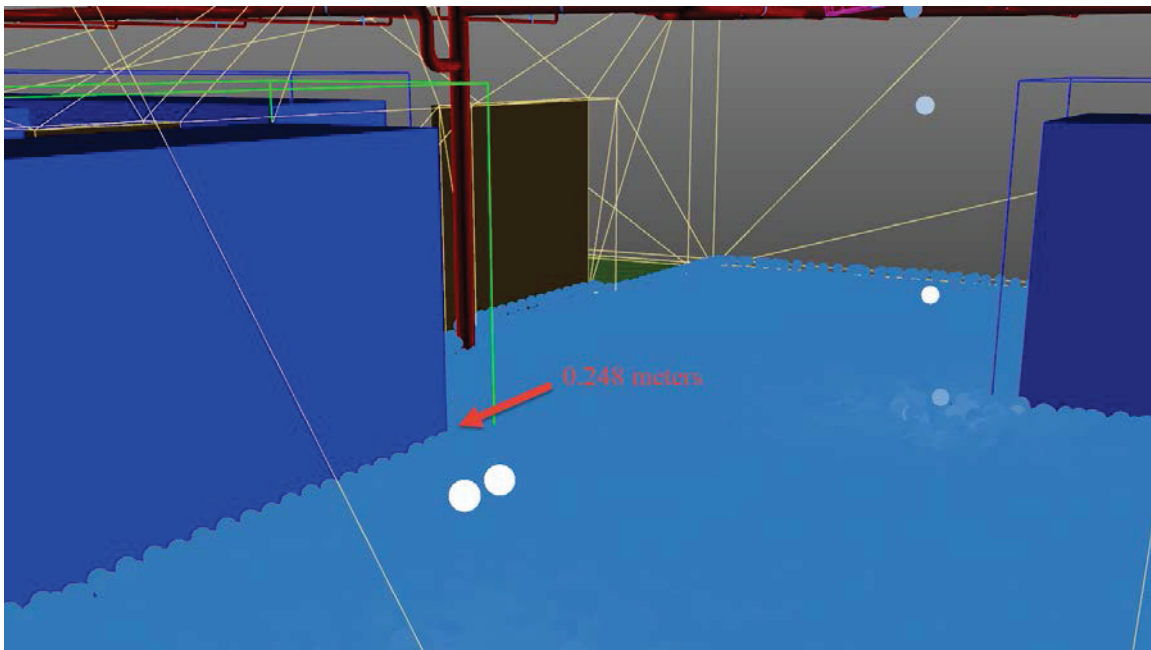 the velocity of those particles depends on the size of the particles, emitter and flow rate. This means that the particle size is the key to getting a good distance on spray. However, the smaller particles, the slower the simulation runs. Second, the particle emitter only emits the particles in the direction indicated, whereas real spray has a pattern or area that is affected.

Because our simulation does not need high resolution or small particles in order to have accurate measurement fields, a better method to simulate spray could be implemented. This method could emit particles according to a pre calculated spray pattern, both area and distance. It would still emit the same volume but target those particles to match the pattern.

Figure 83.   Needed emitter with spray pattern capability
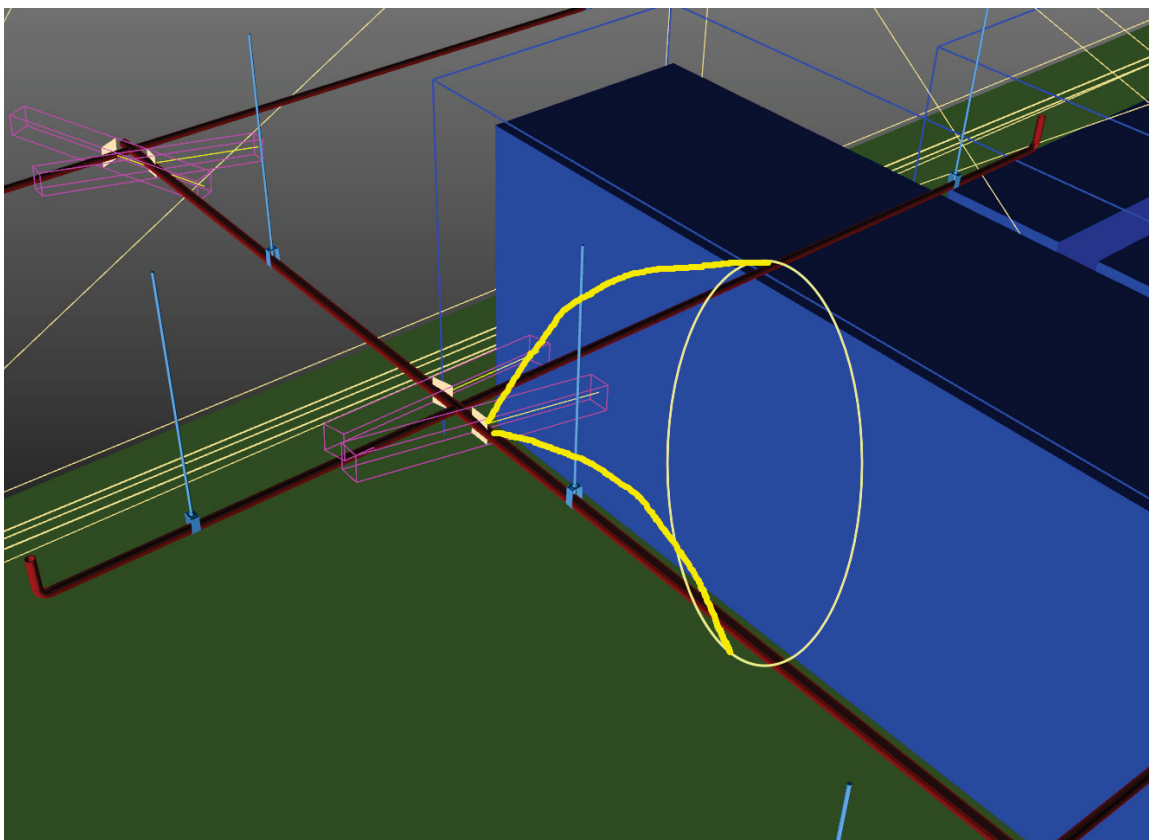
4.2.5   System Thermalhydraulic Analysis

4.2.5.1   Modelling

As detailed in (Parisi 2016), the reference NPP for IA2 is the INL Generic PWR (IGPWR). Using publicly available information, we created the IGPWR, which is based on a 2546 MWth Westinghouse 3-loop PWR (Virginia Electric and Power Company 2007). The main characteristics are reported in Table 23.

Table 23. Design Parameters of the INL Generic Pressurized Water Reactor.

Parameter	Value (SI units)	Value (British units)
Core Power [MW$_{th}$]	2,546	
Reactor Inlet / Outlet Temperature [^{o}C / ^{o}F]	282 / 319	540 / 606
Number of Fuel Assemblies	157	
Rod Array	15x15	
RCS Coolant Flow [kg/s / lb$_m$/hr]	12,738	101.6E+8
Nominal RCS Pressure [MPa /psia]	15.5	2,250
MCP seal water injection [m^3/s / gpm]	3.78E-3	8
MCP seal water return [m^3/s / gpm]	1.42E-3	3
MCP Power [MW / hp]	4.00	5,364
Number of SG	3	
PRZ PORV set points op./clos. [MPa / psig]	16.2 / 15.7	2,350 / 2,280
PRZ PORV capacity [kg/s / lb$_m$/hr]	2 x 22.5	2 x 179,000
PRZ SV set points op./clos. [MPa / psig]	16.4 / 17.7	2,375 / 2,575
PRZ SV capacity [kg/s / lb$_m$/hr]	3 x 37.0	3 x 293,330
Relief Tank Rupture Disc capacity [kg/s / lb$_m$/hr]	113.4	9.0E+5
Relief Tank Rupture Disc set point op. [MPa / psid]	6.89	1000
Relief Tank Total Volume [m^3 / ft^3]	36.8	1300
Relief Tank Water Volume [m^3 / ft^3]	25.5	900
SG PORV capacity [kg/s / lb$_m$/hr]	1 x 47.0	1 x 3.73E+5
SG PORV set points op./clos. [MPa / psig]	7.24 / 6.89	1,050 / 1,000
SG SV capacity [kg/s / lb$_m$/hr]	5 x 94.0	5 x 7.46E+5
SG SV set points op./clos. [MPa / psig]	8.16 / 7.53	1,184 / 1,092
Secondary Pressure [MPa / psia]	5.405	785
Secondary Side Water Mass @ HFP [kg / lb$_m$]	41,639	91,798
SG Volume [m^3 / ft^3]	166	5,868
SG Steam Flow rate @ HFP [kg/s / lb$_m$/hr]	473.0	3.756E+6
FW Temperature [^{o}C / ^{o}F]	228	443
Main FW pump [m^3/s / gpm]	2 x 6.513 (at 518 m)	2 x 13,800 (at 1,700 feet)
Turbine-driven AFW pump [m^3/s / gpm]	1 x 0.3304 (at 832 m)	1 x 700 (at 2,730 feet)
Motor-driven AFW pump [m^3/s / gpm]	2 x 0.1625 (at 832 m)	2 x 350 (at 2,730 feet)
Emergency Condensate Storage Tank [m^3 / ft^3]	416	14,691

Parameter	Value (SI units)	Value (British units)
Accumulator Water Volume [m^3 / ft^3]	3 x 27.61	3 x 975
Accumulator Pressure [MPa /psig]	4.14-4.59	600-665
High Head Safety Injection [m^3/s /gpm]	3 x 0.0708 (at 1,767 m)	3 x 150 (at 5,800 ft)
Low Head Safety Injection [m^3/s /gpm]	2 x 1.416 (at 68.6 m)	2 x 3,000 (at 225 ft)
Containment Volume [m^3 / ft^3]	50,970	1,800,000
Containment Design Pressure [MPa /psig]	0.31	45
Containment Operating Pressure [MPa /psia]	0.062 to 0.071	9 to 10.3
Containment Operating Temperature [^oC / ^oF]	24 to 52	75 to 125
RHR Pump capacity [m^3/s /gpm]	2 x 1.888 (at 70.1 m)	2 x 4,000 (at 230 ft)
Component Cooling Water Pump capacity [m^3/s /gpm]	2 x 4.248 (at 61.0 m)	2 x 9,000 (at 200 ft)

The RELAP5-3D model developed for analyzing SBO-like events is based on an input-deck describing:

- Reactor pressure vessel (RPV);
- Three main circulation circuits (MCC), including the main coolant pumps (MCP) and the steam generators (SG);
- Pressurizer (PRZ), and its main valves (PORV and SV);
- Connections for the emergency core cooling system (ECCS) and the auxiliary feed-water (AFW);
- Secondary part of the SGs up to the SG outlet, including the main valves (PORV and SV);
- Main feed-water (MFW).

The sketches of the RPV and of the MCC, including the secondary side of the SGs, are provided in Figure 84 and Figure 85.

Three independent TH channels representing the central, the middle and the periphery of the core are used. A sketch of the three-channel core region subdivision is given in Figure 86, together with the number of the fuel assemblies and their relative radial power. Passive and active heat structures simulate the heat transfer between the coolant and fuel, the structures and the secondary side of the IGPWR. No heat losses toward the containment are included in the model.

There are 214 hydraulic volumes connected by 257 junctions and coupled to 240 heat structures compose the nodalization. The total number of mesh points, discretizing the heat structures, is 1312. The model is based on a nodalization developed for the RELAP/SCDAP code for SBO analyses (Bayless 1987).
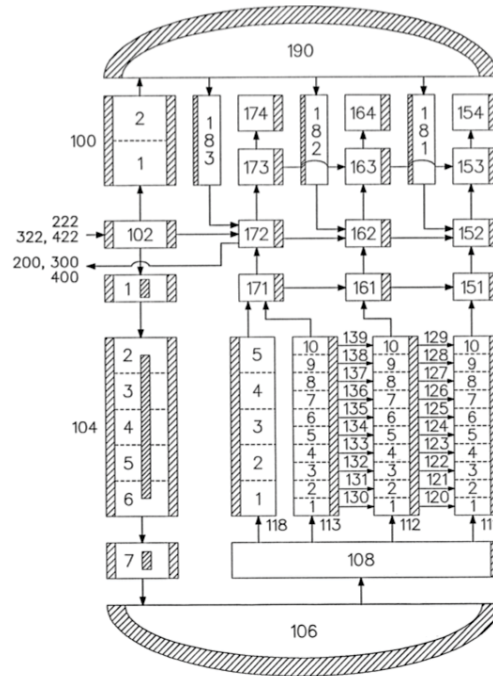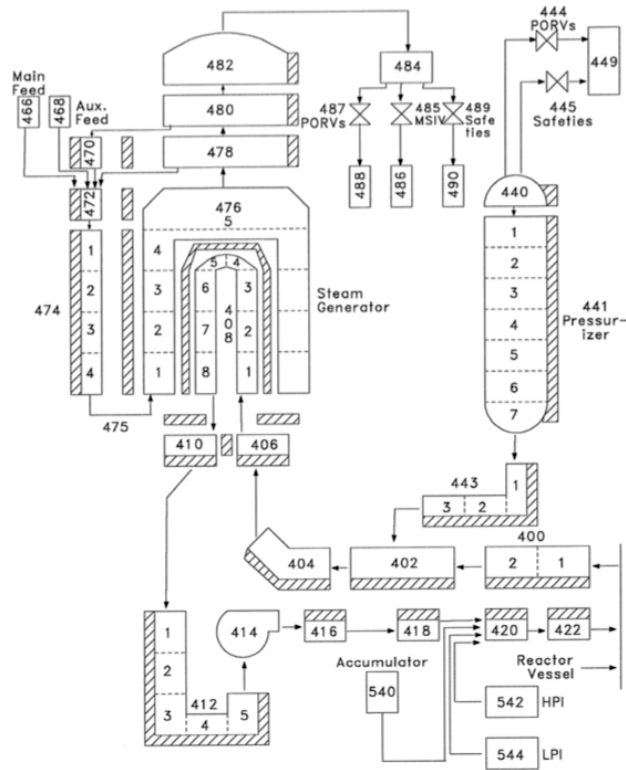
Figure 84.   RELAP5-3D RPV Model.

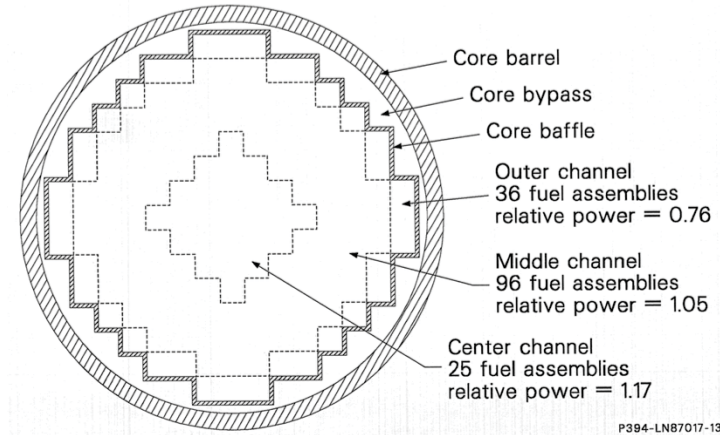Figure 85.   RELAP5-3D MCC and SG Model.

Figure 86. RELAP5-3D Core Model.

The possible operator actions (SG cool-down, feed and bleed, AFW flow control, etc.) are implemented through the RELAP5-3D control logic. RELAP5-3D control variables calculate the derived parameters for the control logic and for the transients' analyses.

4.2.5.2   Model Validations

A steady state and an on-transient validation have been performed for assessing the RELAP5-3D model calculations. Results demonstrated that the model is in an excellent agreement with the NPP reference data and with independent transient calculations. Details are provided in (Parisi 2016).

4.2.5.3   Scenarios

SBO is defined by the 10 CFR 50.2, as the complete loss of alternating current (AC) electric power to the essential and nonessential switchgear buses in a NPP (i.e., loss of offsite electric power system concurrent with turbine trip and unavailability of the onsite emergency AC power system).

SBO does not include the loss of available AC power to buses fed by station batteries through inverters or by alternate AC sources, nor does it assume a concurrent single failure or design basis accident. Thus, loss of all AC power results in unavailability of all normal electrical equipment and most of the safety electrical equipment.

For the IA2 test case, an EQ-induced loss-of-offsite and on-site AC power occurs at time t=0, resulting in a SBO event. Two cases have been considered and described in (Parisi 2016): Long Term SBO (LTSBO) and Short Term SBO (STSBO).

In the first case, it is assumed that no DC power is lost and the operator is able to perform reactor cool-down using feed-and-bleed procedure on the secondary side. The first 8 hours of the event (until battery depletion) are considered.

112

On the last case (STSBO), more EQ-induced failures on the site are assumed: all DC power is lost and no water source is available for the actuation of the TD-AFW. Because of the unavailability of heat sinks, the reactor core rapidly overheats and fuel damage (PCT>1500 K) occurs in ~2.5 hours.

The above scenarios do not credit the mitigating actions from an emergency crew and they consider just the actions performed by the operator in the control room (SG depressurization and cooling).

Thus, as a successive step for the IA #2 activities, some mitigative measures have been modeled. The mitigative actions are consistent with the so-called FLEX strategy (NEI, 2012), which is being pursued by the US NPP licensees after the Fukushima Dai-ichi accident. FLEX strategy aims to increase the level of Defense in Depth (DiD) during extended loss of AC power with Loss of Ultimate Heat Sink caused by Beyond-Design Bases External Events (BDBEE).

The following systems were considered available to the NPP crew (NRC 2013):

- TD-AFW: available until battery exhaustion (~8 hr) or Emergency Condensate Storage Tank (ECST) water depletion (~6 hr)

- SG and PRZ PORV: available until battery exhaustion (~8 hr).

- High-pressure, diesel-driven pump (Kerr pump), to be connected to the Low-Pressure Injection System (LPIS) drain lines

- Portable air bottles to operate the SG PORVs

- TD-AFW manual operation without DC power (blackrun mode)

- Portable, diesel-driven pump (Godwin pump) for supply water to the fire header and from there to the TD-AFW

- Portable power supply for monitoring SG and RPV levels

The successful implementation of procedures including the above back-up systems can lead to a mitigation of the SBO outcome protecting one or more fission barriers and eventually avoiding core damage by coping time extension.

Two cases were run for testing the mitigating strategies, the mitigated LTSBO (MLTSBO) and the mitigated STSBO (MSTSBO). For each one of these cases, an early failure of the MCP seal (182 gpm leak per pump after 13 minutes) has been also considered.

4.2.5.3.1   Mitigated LTSBO

The MLTSBO scenario involves no damage of the batteries and the use of mobile pumps, air bottles and power supply for operating the TD-AFW after battery depletion (8 hr). Water injection in the primary side is also performed at t=+3.5 hr, after the SG cool down and primary side depressurization. The sequence of events for the base case and for the early MCP seal failure is reported in Table 24. The timing of the SOARCA report calculations (NRC 2013) are also reported for comparison.

Table 24. Sequence of events and results for the reference MLTSBO case.

EVENT DESCRIPTION	TIME [hh:mm] INL / RELAP5-3D (NRC 2013).	
	MCP seal leakage	Early MCP seal failure
	(21 gpm)	(182 gpm)
Initiating event Station blackout – loss of all onsite and offsite AC power	00:00	00:00
Reactor trip MSIVs close MCP seals initially leak at 21 gpm/pump (~1 Kg/s)	00:00 (00:00)	00:00 (00:00)
TD-AFW auto initiates at full flow	00:01 (00:01)	00:01 (00:01)
RCP seal fail, leaking 182 gpm/pump	N/A	00:13 (00:13)
First SG SRV opening	00:15 (00:03)	00:15 (00:03)
Operators control TD-AFW to maintain level	00:15 (00:15)	00:15 (00:15)
Void Formation in the UH	01:41	00:27
Operators initiate controlled cooldown of secondary at ~100 F/hr (~55.5 K/hr)	01:30 (01:30)	01:30 (01:30)
UP water level starts to decrease	02:02 (01:57)	00:38 (01:13)
Accumulators begin injecting	02:34 (02:25)	02:15 (02:15)
Vessel water level begins to increase	02:36 (02:30)	N/A
Start emergency diesel pump injection into RCS	03:30 (03:30)	03:30 (03:30)
SG cool-down stopped at 120 psig (9.29 MPa) to maintain TD-AFW flow	03:43 (03:35)	03:43 (03:35)
ECST empty. Operator activate a portable, diesel-	~07:35	~08:44

driven pump (Godwin pump) for supply water to the TD-AFW		
DC Batteries Exhausted. Operator actions control the secondary pressure at 120 psi and maintain TD-AFW flow	08:00	08:00
Level maintained at the CL elevation with emergency pump	N/A	12:38

Mitigated LTSBO – 21 gpm leakage

The trend of the main TH parameter for the base case - MLTSBO are provided in the next figures and in Appendix B.1. After the reactor scram, the MCP run-down and the SG isolation, the TD-AFW is automatically started. After 15 minutes, the operator takes control of the TD-AFW for regulating the SG level. At t=+1.50 hr, SG depressurization and cooldown is performed actuating the SG PORV and the TD-AFW. The primary side pressure and temperature are reduced by the SG cooldown as well.

The primary side pressure of the core stays above the saturation conditions until the middle of the transient (t=+13 hr). The primary side pressure reduction allows the injection of the accumulator water at t=+2hr and 36 minutes. Accumulator water injection leads to an increase of the RPV level above the top of the UP. It is then assumed that the emergency crew is able to connect a mobile diesel (Kerr) pump to the header of the LPSI. However, the Kerr pump water is not injected, since the RPV water level stays above the HL/CL top during the considered time window of the MLTSBO scenario (24 hr).

At t=+8.0 hr the batteries are depleted, so the emergency crew uses the fire-water and mobile equipment for continuing the operation of the TD-AFW. These emergency actions allow a safe cooldown of the plant during the remaining hours.
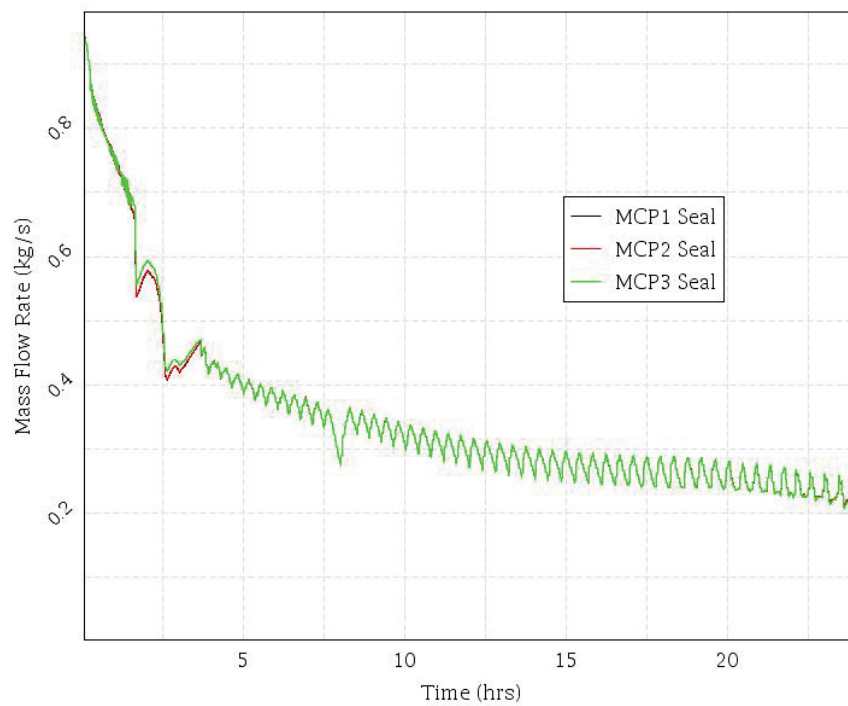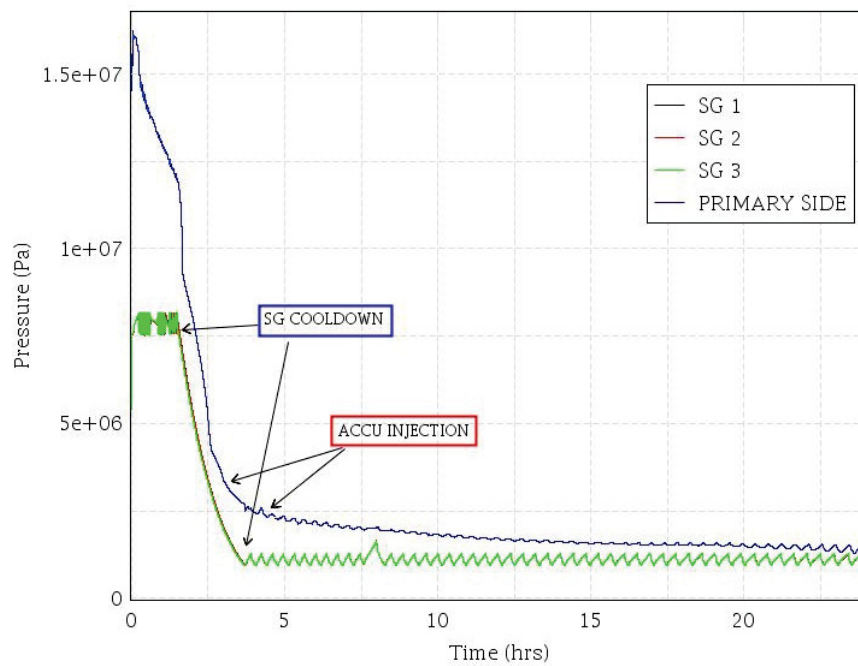
Figure 87. MLTSBO – MCP Seal Leakage.

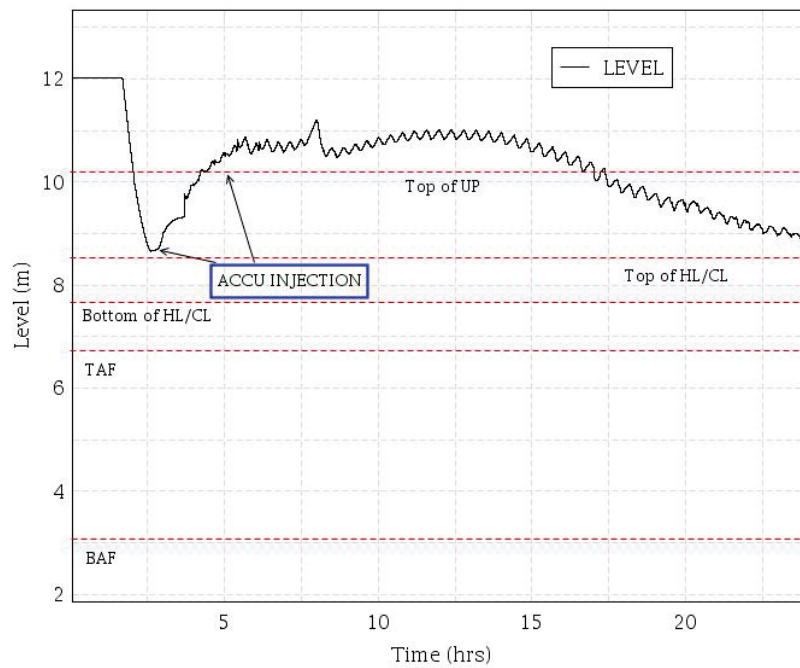Figure 88. MLTSBO – Pressures trends.
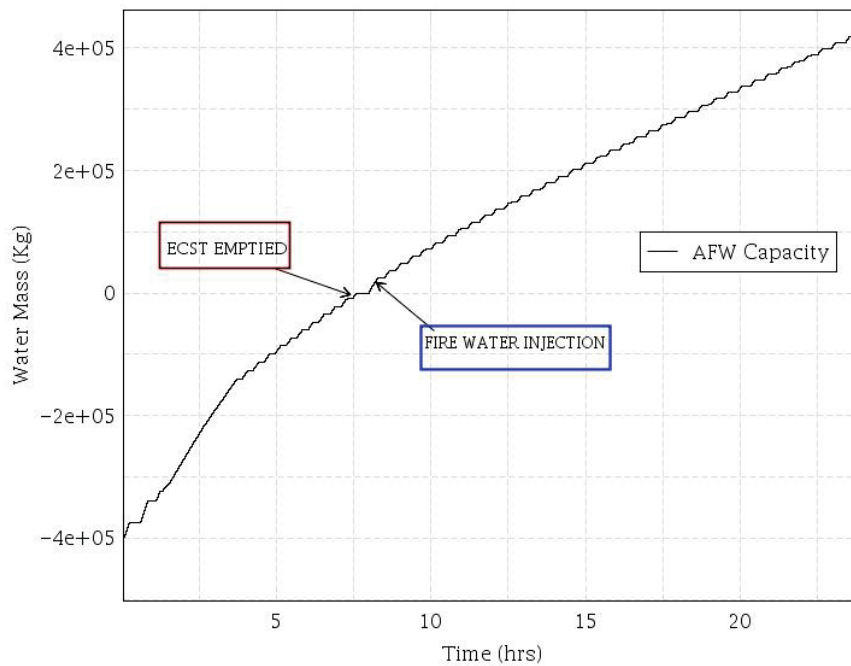
Figure 89.   MLTSBO – RPV Water Level.

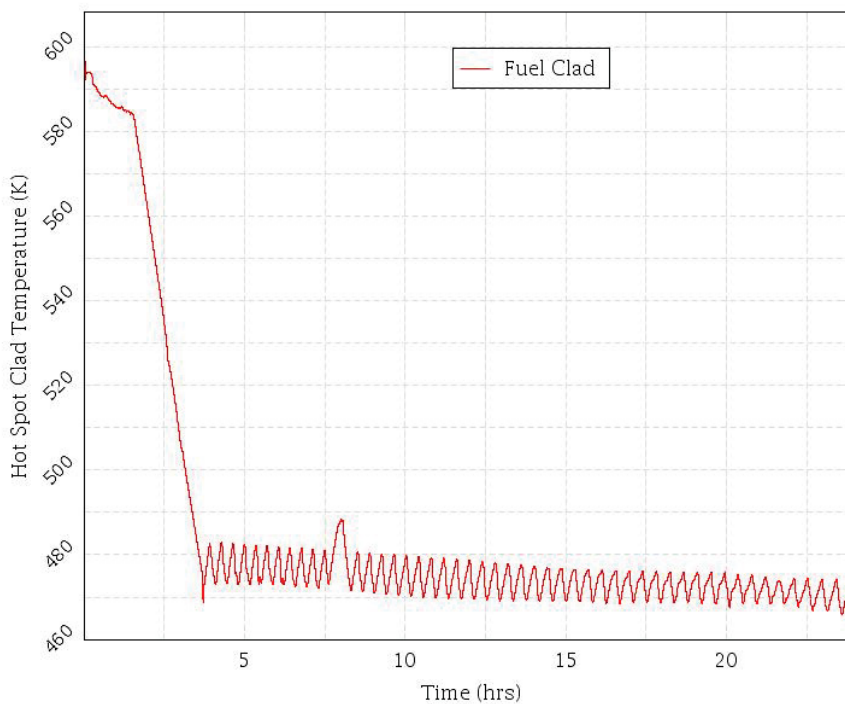

Figure 90.   MLTSBO – AFW Capacity.

Figure 91.   MLTSBO – Hot Spot Clad Temperature.

Mitigated LTSBO – 182 gpm leakage

The trend of the main TH parameter for the early MCP seal leakage - MLTSBO are provided in the next figures and in Appendix B.2. The transient differs from the previous one by the larger break area (8 times bigger) in the MCP seals. Thus, the transient dynamic is closer to a reference SBLOCA.

After the reactor scram, there are: MCP run-down, SGs isolation and automatically start of TD-AFW. At t=+13 minutes, the MCP seal leakages increase at 182 gpm per MCP. Operator takes control of the TD-AFW for regulating the SG level at t=+15 minutes. At t=+1.50 hr, SG depressurization and cooldown is performed actuating the SG PORV and the TD-AFW.

During the first 13 minutes the primary pressure drops because of the energy removal from the SGs. Then, at t>+13 minutes, the primary pressure drops to the saturation conditions because of the MCP Seal LOCA mass flow increases at 182 gpm. The consequent void production reduces the pressure decrease rate until this rate is increased again by the SG cooldown at t=+1.5 hr.

Two-phase natural circulation occurs in the primary system until the end of the transient. The primary side pressure reduction allows the injection of the accumulator water at t=+2hr and 15 minutes. This water injection leads to an increase of the RPV water level to the top of the HL/CL. The emergency crew is then able to connect a mobile diesel (Kerr) pump to the header of the LPSI at t=+3.5 hr, allowing a RPV water level stabilization at the HL/CL bottom, thus avoiding core uncovering.

At t=+8.0 hr, the batteries are depleted, so the emergency crew uses the fire-water and mobile equipment for continuing the operation of the TD-AFW. These emergency actions allow a safe cooldown of the plant during the remaining hours.

The RCS two phase NC is strongly reduced at t=~+12 hr, because of the voiding in the descending parts of the SG tubes of loops #1 and #3. The NC is increased again at t=~+15hr by loop seals #1 and #3 clearings.
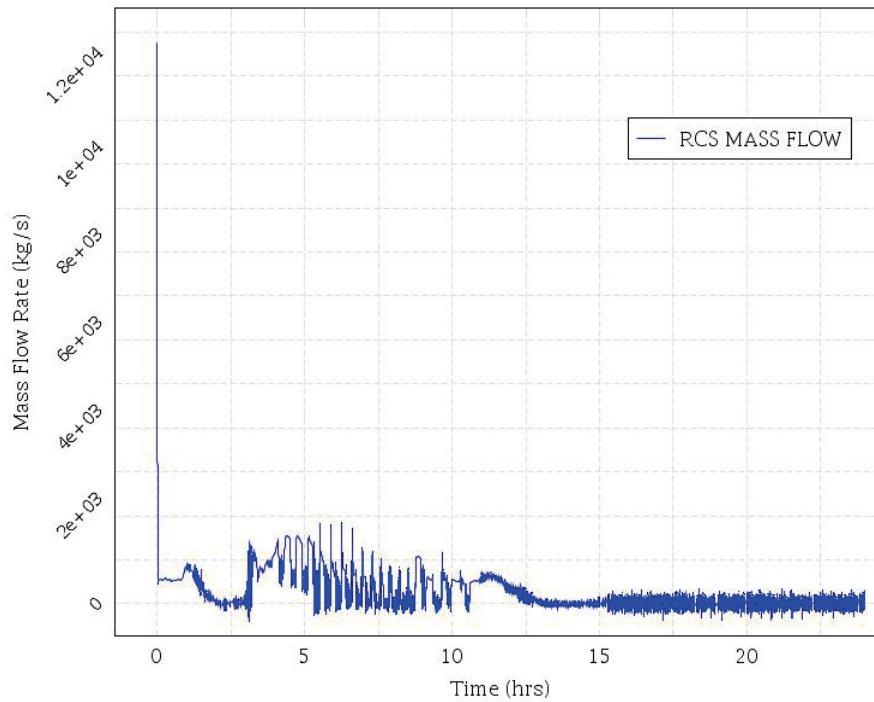

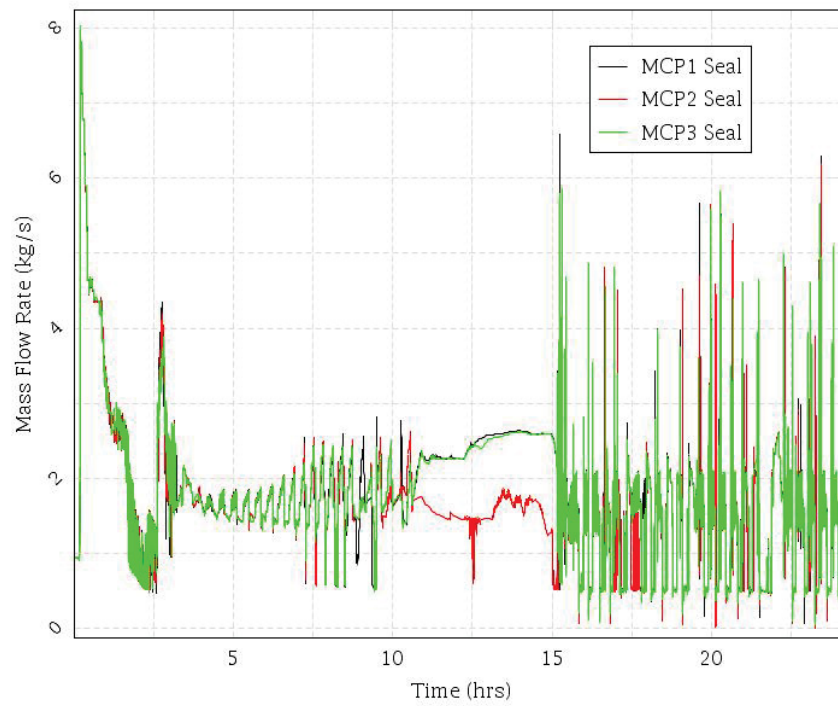Figure 92. MLTSBO and 182 gpm LOCA – RCS Mass Flow.

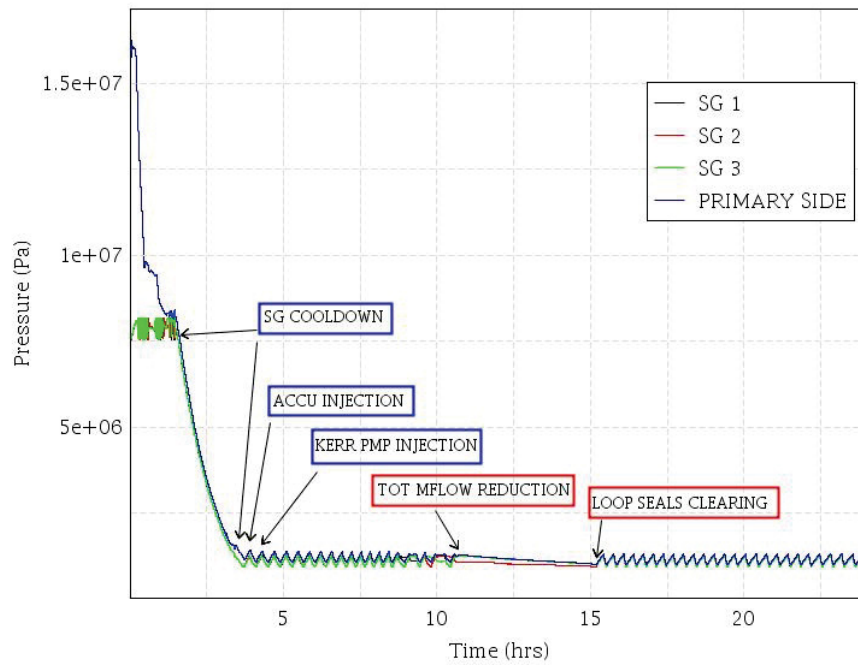Figure 93.   MLTSBO and 182 gpm LOCA – MCP Seal Leakage.
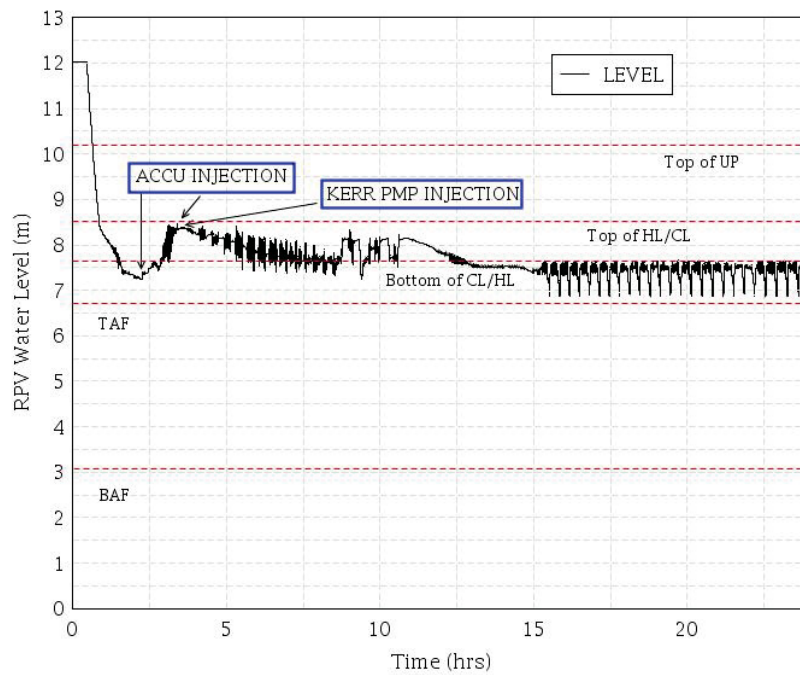

Figure 94.   MLTSBO and 182 gpm LOCA – Pressures trends.

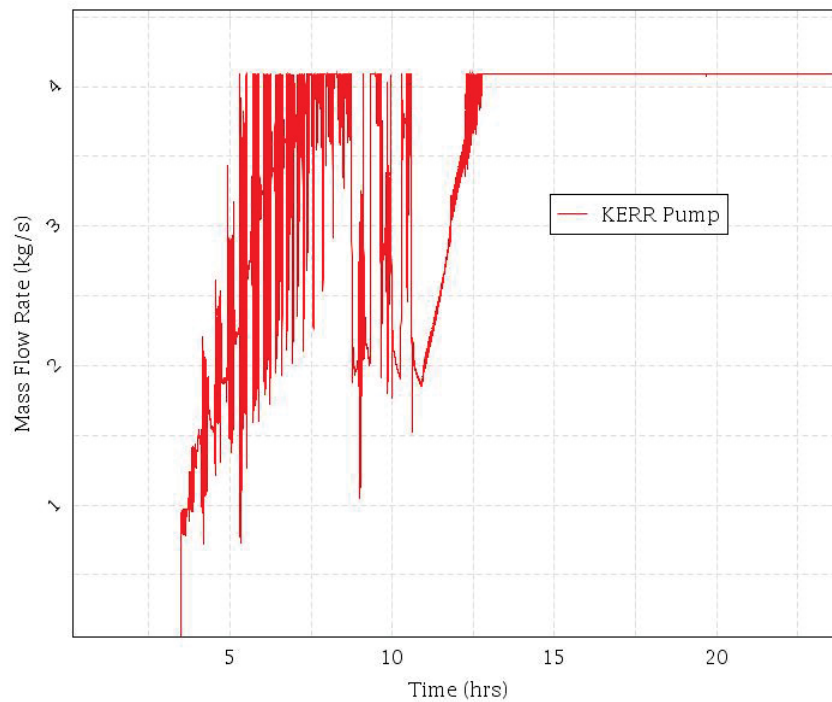Figure 95.   MLTSBO and 182 gpm LOCA – RPV Water Level.

Figure 96.   MLTSBO and 182 gpm LOCA – Kerr Pump Injection Mass Flow.
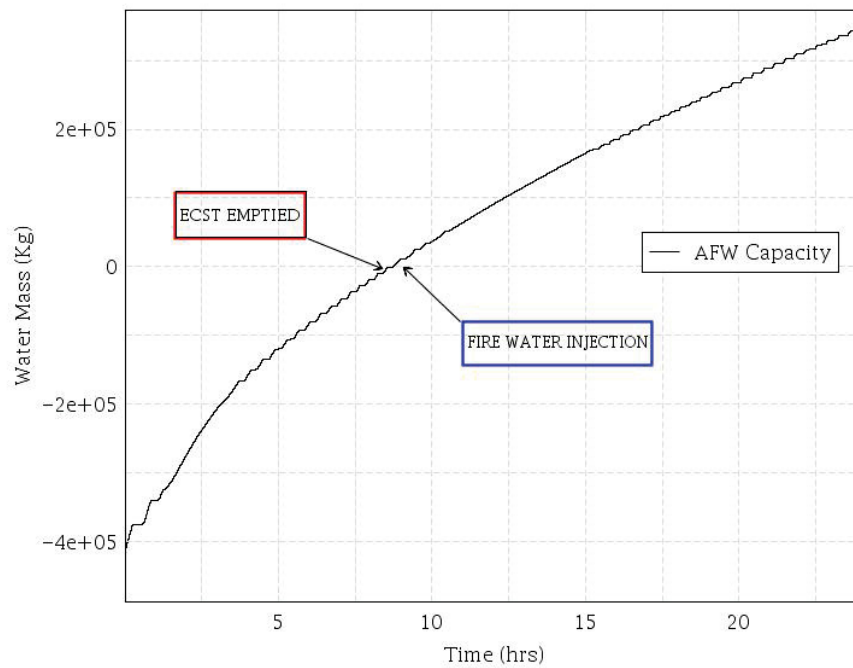
121

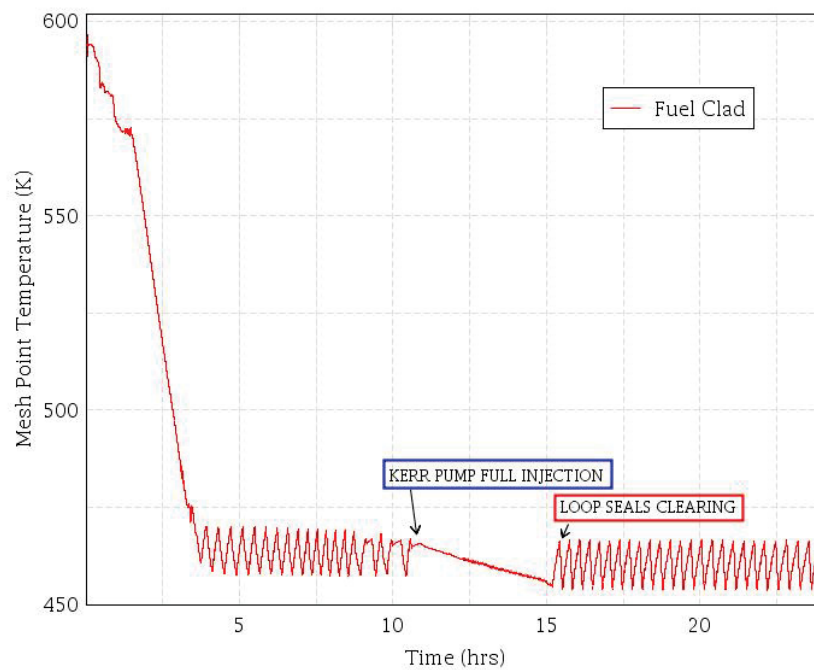Figure 97.   MLTSBO and 182 gpm LOCA – AFW Capacity.

Figure 98.   MLTSBO and 182 gpm LOCA – Hot Spot Clad Temperature.

4.2.5.3.2   Mitigated STSBO

The scenario MSTSBO is involving the immediate loss of TD-AFW pump functionality because of EQ damages. Because the mitigative actions are not supposed to be deployed before 2 hours after the TD-AFW loss, this scenario always results in core uncovers and fuel failure. This statement has been verified by a set of sensitivity analysis where the recovery time, the TD-AFW failure time and the MCP leakage rate have been changed. Results are provided in Table 25.

Table 25. Fuel Failure Map for Mitigated STSBO for 21 and 182 gpm MCP seal leakage

TD-AFW Failure Time (hr)	Recovery Time (hr)		
	0.5	1	2
0.0	F	F	F
1	F	F	F
2	S	F	F

This scenario has not been calculated by EMRLAD/Neutrino/RELAP5-3D sequence because it has been assumed:

- a TD-AFW failure immediately after the EQ;

- a minimum recovery time of 2 hr.

If the scenarios selected by EMRLAD have such boundary condition (TD-AFW failure by EQ), they are automatically identified as scenarios leading to fuel damage.

4.2.5.3.3   Mitigated LTSBO and Battery Failure

The coupling between Neutrino and RELAP5-3D involve scenarios where significant damage happens to components in the auxiliary building (e.g., batteries, batteries chargers, switches, etc.). A set of calculations has been run assuming:

- Batteries failure happens during the first hour at maximum. This is the time required by the NPP operators for shutting down the leakages of the sprinkler system;

- If batteries failure happens, the minimum time required for setting up recovery actions has been assumed equal to 1.5 hr;

- Recovery actions are based on:
    - Use of air bottles for actuations of SG PORV and blackrun of TD-AFW;
    - Use of Godwin pump for injecting water in the fire water header for feeding the TD-AFW;
    - Use of mobile Kerr pump for injecting water in the primary side via the LPSI header;
    - Use of mobile power supply for monitoring the SG and RPV levels.

The set of RELAP5-3D analysis presented in Table 26 and Table 27 identify the fuel failures or its safe state depending on the recovery time and the battery failure time.

This information, evaluated at discrete time intervals, help to identify the set of boundary conditions for running the combined EMRLAD/Neutrino/RELAP5-3D calculations. E.g., for a battery time failure of t=+1000 s and a MCP seal leakage of 21 gpm, Neutrino/RELAP5-3D calculations will be run if the sampled recovery time is 3 < t < 3.5 hr (see next Paragraph).

Table 26. Fuel Failure Map for Mitigated LTSBO and Battery Failure for 21 gpm MCP seal leakage

Batteries Failure Time (s)	Recovery Time (hr)			
	1.5	2	3	3.5
0.0	S	S	F	F
1000.	S	S	S	F
2500.	S	S	F	F
3600.	S	S	S	F

Table 27. Fuel Failure Map for Mitigated LTSBO and Battery Failure for 182 gpm MCP seal leakage

Batteries Failure Time (s)	Recovery Time (hr)			
	1.5	2	3	3.5
0.0	S	S	F	F
1000.	S	S	F	F
2500.	S	S	F	F
3600.	S	S	F	F

An example of the possible scenarios reported in the previous Tables is provided in the figures below and in Appendix B.3. E.g., for the case: 182 gpm MCP seal leakage, Batteries Failure Time =+2500 seconds, and recovery time t =+2.5 hr.
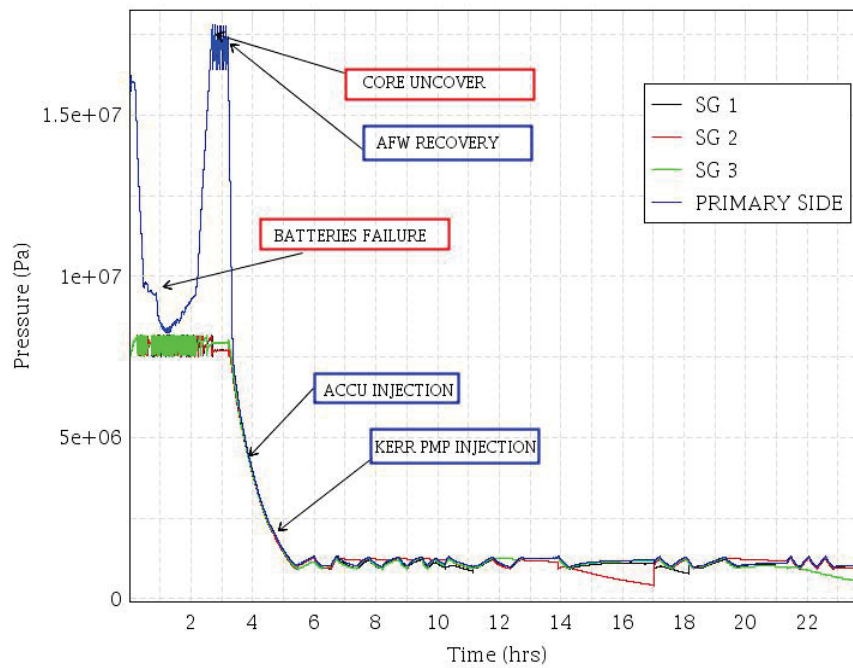
Figure 99. MLTSBO and 182 gpm LOCA and Battery Failure – Pressures trends.
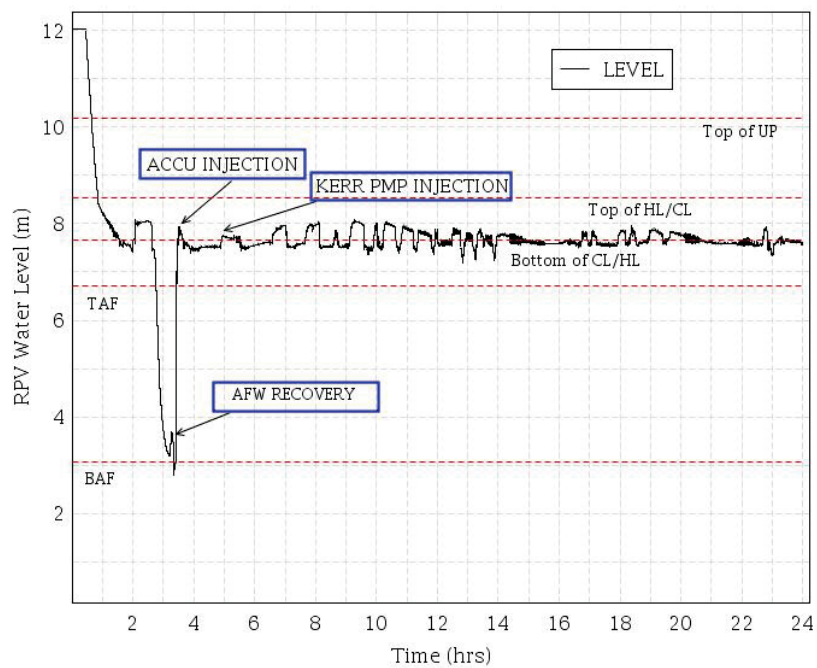

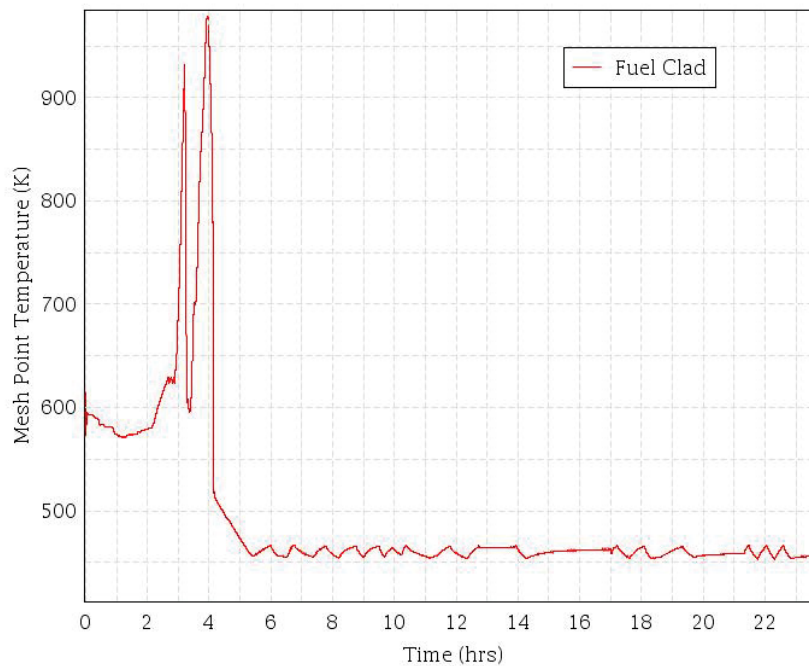Figure 100. MLTSBO and 182 gpm LOCA and Battery Failure – RPV Water Level.

Figure 101. MLTSBO and 182 gpm LOCA and Battery Failure – Hot Spot Clad Temperature.

4.2.5.4 *Uncertainty Analysis*

The advanced use of best estimate tools combined with the PRA implies the quantification of the uncertainties of the deterministic calculations (i.e., performing best estimate plus uncertainty calculations). A simplified uncertainty analysis of the RELAP5-3D BE calculations for the MLTSBO, 182 gpm LOCA and Battery Failure is reported hereafter. The RAVEN code is applied for the automatic processing of the RELAP5-3D input parameters and for the output data processing.

In general, every UQ method is based on the following steps:

1. Selection of the NPP and scenario

2. Characterization of the scenario and identification of important phenomena

3. Selection of the code

4. Preparation and qualification of the input deck

5. Selection of the uncertainty method

6. Application of the uncertainty method

7. Comparison of the results with the relevant criteria

Points 1, 3 and 4 are addressed by the selection of the IGPWR, MLTSBO scenarios, RELAP5-3D code and relative MLTSBO input deck qualification (Parisi 2016). For the characterization of the scenario and the identification of important phenomena, it should be noted that:

126

- this step is generally performed by means of the Phenomena Identification and Ranking Table (PIRT) development. A PIRT development may require the efforts of several experts and it is beyond the scope of the IA #2.

- for the sake of simplicity, a simplified analysis of thermal-hydraulic phenomena is proposed hereafter. In particular, four phases are identified for the MLTSBO characterized in the previous paragraph., i.e.:

  - Phase I: from t=0.0 s to t=41 minutes. Reactor scram, pump run-down, MCP seal LOCA, primary side depressurization, establish RCS two-phase phase natural circulation (NC), SG at full pressure

  - Phase II: from t=41 minutes to t=3.2 hr. RPV water level reduction, core uncover, primary side pressure surge, stop of RCS two-phase NC, SG dry-out, fuel clad temperature spike, PRZ-SRV valves opening

  - Phase III: from t=3.2 hr to t=5 hr. SG and core reflooding. Clad temperature quenching. Steam condensation in the SG – primary side. Restart of RCS two-phase NC.

  - Phase IV: from t=5 hr to t=24 hr. Sustained two-phase NC.

- The most important thermal-hydraulic phenomena characterizing the above phases are identified. They are:

  - NC in the primary loop

  - Secondary side mass inventory loss through the SG SRV and PORV

  - Primary mass inventory loss through the MCP seal and PRZ SRV

  - Heat transfer between primary and secondary system

- The Figure of Merits (FOMs) selected for the analysis is the PCT. The PCT limit is set to 2200 F (1447 K).

- The following list of the input parameters were selected for the sensitivity analyses and their uncertainty band was specified:

  - Core Decay Heat, with a uniform uncertainty distribution of +/-7% of the nominal value. This sensitivity takes into account the uncertainty on the decay heat power

  - Core Pressure Losses: uniform uncertainty distribution resulting in a variation of +18% and -25% of the mass flow. It takes into account the uncertainties on the vertical and the cross-flows during the natural circulation phase at low flow

  - Critical Flow at the SRV/PORV of SG and PRZ: uniform uncertainty distribution resulting in a variation of +/- 30% of the flow area. It takes into account uncertainties in the critical flow prediction and the valves inlet conditions

  - Mass Flow through the MCP seal break: a variation of +/- 20 gpm is considered. It takes into account the uncertainty in the seal break area and on its modeling.

  - SG Heat Exchange Multiplier: uniform uncertainty distribution resulting in a variation of +/-20%. It takes into account the uncertainties in the heat exchange during the different phases.

Sensitivity calculations are run (see Table 28) for assessing the effect of the single uncertainty parameters on the FOM.

Table 28. Sensitivity Parameters.

Run #	Sensitivity Parameter
Reference Case	Nominal values
1A	Core Decay Heat +7 %
1B	Core Decay Heat -7 %
2A	Reduction of RPV internal circulation mass flow
2B	Increase of RPV internal circulation mass flow
3A	SG/PRZ PORV and SRV valve flow areas increased by 30%
3B	SG/PRZ PORV and SRV valve flow areas decreased by 30%
4A	MCP seal LOCA +20 gpm
4B	MCP seal LOCA -20 gpm
5A	SG HX Multiplier +20%
5B	SG HX Multiplier -20%

The sensitivity analysis showed that the considered uncertainty on the seal LOCA mass flow has a negligible effect on the PCT (see Appendix B.4). Thus, the demonstration of the propagation of the uncertainties is performed for the remaining four parameters listed above and it is carried on using the Code Scaling, Applicability and Uncertainty Evaluation methodology (point 5).

Then input parameters are then simultaneously perturbed by RAVEN code using a Monte Carlo sampler. Wilks' formula is used for achieving a 95% fractile/95% confidence limit on the resulting FOM. 59 calculations are runs (see Figure 102). Ranking of the input uncertain parameters is also performed *a posteriori*, identifying the correlation coefficients between the FOMs and input uncertainties.
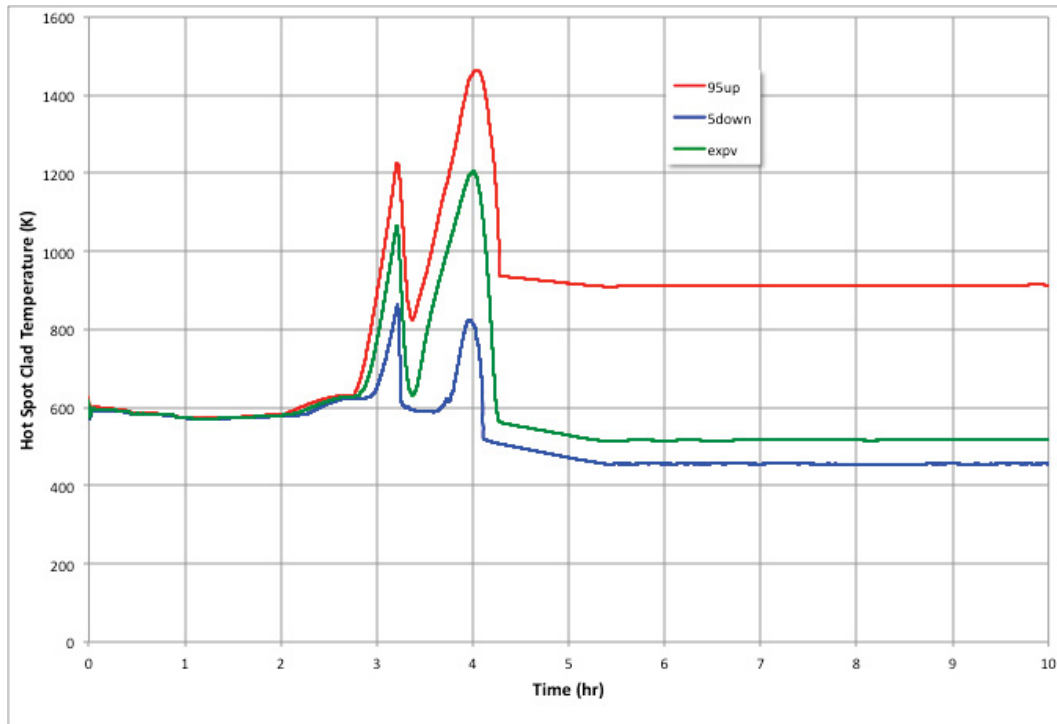
Figure 102. RAVEN/RELAP5-3D uncertainty analysis for MLTSBO, 182 gpm LOCA and Battery
Failure – PCT.

Table 29. RAVEN/RELAP5-3D Uncertainty Analysis – Pearson Correlation Coefficients for PCT and
Uncertainty Parameters.

Input Uncertainty Parameters	Pearson Correlation Coefficients
Decay Power	+0.0796
SG HX Multiplier	+0.0438
SG PORV Area	-0.0086

4.2.6   Coupled Results

The simulations from the combined RISMC tools were run on five high end computers. Each
computer running 4 jobs. The computer specifications were as follows:

- CPU – Intel Xeon E5-2683
- Speed 2.00 GHz
- 2 Sockets
- 56 Logical Processors

EMRALD code managed the calculation flow, running Neutrino 3-D flooding calculations. In
order to save computational resources, RELAP5-3D was directly run only when the sequence of events
was on the fuel status uncertain zones identified in Table 26 and Table 27 (e.g., at battery failure time of
1000 seconds, MCP leakage 21 gpm, and 3 hr < recovery time < 3.5 hr). Calculation statistics are

reported in Table 30 below, while the final CDF calculation are reported in Table 32. RELAP5-3D indirect calculations resulting in non-fuel damage events are ~7.4% of the total events.

Table 30. EMRALD/Neutrino/RELAP5-3D Statistics.

Parameter	Value
Total EMRALD runs	67,877,823
Total Running Time	~263 hours
Significant EQ Events (PGA > X)	4311
SBO Events	258
Neutrino simulations	261
RELAP5-3D indirect calculations	245
RELAP5-3D direct calculations	0

No direct RELAP5-3D calculations resulted from the combined EMRALD/Neutrino/RELAP5-3D calculations the likely reason for this was an error discovered after the simulations were run. The recovery time was assumed at t=+2 hr, i.e. not depending from the battery failure time. This would cause almost all sampled recovery times to fall within the known region. Final results with estimation of the EQ-induced SBO and of CDF probabilities are reported in Table 32. Table 31 reports the number of seismic events, grouped by PGA, which triggered the SBO calculations. Final results with estimation of the seismic-induced SBO and of CDF probabilities are reported in Table 32.

Table 31. Seismic events causing SBO – PGA grouping.

PGA of EQ Events	Number of Events
< 1.5 g	38
[1.5 g – 2.0 g)	82
[2.0 g – 2.5 g)	77
[2.5 g – 3.0 g)	11
[3.0 g – 3.5 g)	10
[3.5 g – 4.0 g)	9
>= 4.0 g	7

Table 32. Final CDF.

Event	Probability (events/year)
SBO	3.80E-6
CDF	2.84E-8
CDF w/o RELAP5-3D feedback	1.47E-8

5. SUMMARY AND PATH FORWARD

Development of the next generation tools and methods for external events PRA is ongoing under the RISMC technical pathway. Toolkit success centers on integration of the tools and methods under a common framework, MOOSE. These tools and methods make use of existing and newly developed tools and methods, coupled with the experience and data gained in the past decades, to define and analyze more realistic risk assessment models.

Significant capability has been added to Mastodon to simulate 3-D wave passage effects through nonlinear soil. Verification has demonstrated the capability of Mastodon to model wave passage effects in 1-D, 2-D, and 3-D. Additional capability will be added to Mastodon over the next year to implement a robust gapping and sliding element for cyclic shaking, web-based verification and user manuals, stochastic finite elements, and frequency independent damping. Verification of added capabilities will occur in parallel with code writing activities. Table 33 provides an overview of the planned activities for FY 2017.

Table 33. Planned development activities for FY 2017

LWRS (FY 2015 and FY 2016)	LWRS (FY 2017)
Newmark Beta Time Integration	Gapping and Sliding Element for Cyclic Shaking
Hilber-Hughes-Taylor Time Integration	Web-based Verification and User Manuals
Nonlinear Soil Constitutive Model (Soil-HYS)	Frequency Independent Damping
Soil-Foundation Interaction, Gapping and Sliding (Under Development)	Verification of New Capabilities
	Beta Version of Mastodon

Neutrino provides an advanced GUI that makes it easy to visualize the model being worked on. Neutrino provides a mesh-less based SPH approach for simulating both internal and external flooding. Neutrino allows for different types of particle emitters: a flow rate particle emitter that can be used to simulate water flow through a penetration or a pipe break; a Toricelli emitter that creates particles to match a given rainfall rate, surface area, and opening; a teleport emitter that moves particles from one level to another simulating the flow through a pipe. Other emitter options and validation tests are in development.

EMRALD, is a dynamic PRA code based on three-phased discrete event simulation. EMRALD communicates with both the seismic and flooding tools to calculate risk. A model for EMRALD consists of states with immediate actions, and conditional event actions. Many different types of events and actions can be evaluated or executed, designed in a way for easy equivalents to items in traditional PRA such as basic events and fault trees. States can also be tagged as "key states" and are noted if a simulation run ends on that state. Through multiple runs of the simulation model, probabilities of each key state are derived. In addition, heuristics can be made to show the path or cause of the key state and the times of those events.

FY 2017 will focus on couple the seismic, flooding, and dynamic PRA capability in the MOOSE framework. Verification of capabilities will be a key focus of FY 2017. In addition, RISMC is currently working with an industry partner to identify an industry application problem that the RISMC toolkit will solve in FY 2017.

6. REFERENCES

Aki, K. and P. G. Richards, 2012, Quantitative Seismology, University Science Books.

Bayless, P. D., 1987, "Natural Circulation during a Severe Accident: Surry Station Blackout", EGG-SSRE-7858, September 1987.

Baker, J. W., 2015, "Efficient Analytical Fragility Function Fitting Using Dynamic Structural Analysis," Earthquake Spectra, Vol. 3, No. 1, pp. 579-599.

Bielak, J., K. Loukakis, Y. Hisada and C. Yoshimura, 2003, "Domain Reduction Method for Three-Dimensional Earthquake Modeling in Localized Regions, Part I: Theory," Bulletin of Seismological Society of America, https://dx.doi.org/10.1785/0120010251.

Bolisetti, C., J. L. Coleman, M. Talaat and P. Hashimoto, 2015, "Advanced Seismic Fragility Modeling Using Nonlinear Soil-Structure Interaction Analysis," INL/EXT-15-36375, Idaho National Laboratory, Idaho Falls, Idaho, 2015.

Bolisetti, C. and A. S. Whittaker, 2015, "Site Response, Soil-Structure Interaction and Structure-Soil-Structure Interaction for Performance Assessment of Buildings and Nuclear Structures," MCEER-15-0002, Multidisciplinary Center for Earthquake Engineering Research, University at Buffalo, The State University of New York, Buffalo, NY, 2015.

Bolisetti, C., A. S. Whittaker and J. L. Coleman, 2016, "Linear and Nonlinear Soil-Structure Interaction Analysis," Soil Dynamics and Earthquake Engineering, Under review.

Chiang, D. Y. and J. L. Beck, 1994, "A New Class of Distributed-Element Models for Cyclic Plasticity — I. Theory and Application, International Journal of Solids and Structures," Vol. 31, No. 4, pp. 469-484.

Coleman, J. L., C. Bolisetti and A. S. Whittaker, 2015, "Time-Domain Soil-Structure Interaction Analysis of Nuclear Facilities," Nuclear Engineering and Design, Vol. 298, pp. 264-270.

Coleman, J. L., C. L. Smith and A. M. Kammerer, 2016, "Plan to Verify and Validate Multi-Hazard Risk-Informed Margin Management Methods and Tools," INL/EXT 16 39195, Rev. 1, Idaho National Laboratory, 2016

Coleman, J.L, C. L. Smith, D. Burns, and A. M. Kammerer, 2016. "Development Plan for the External Hazards Experimental Group", Report INL/EXT-16-38328, Revision 1, Idaho National Laboratory, Idaho Falls, ID

CSI, 2011, Computer Program: SAP2000 - Structural Analysis Program, Version 11.0.0. Computers and Structures, Inc., Berkeley, California.

Darendeli, M., 2001, Development of a New Family of Normalized Modulus Reduction and Material Damping Curves, Ph.D. Thesis, Department of Civil Engineering, University of Texas, Austin.

DOE, 1997, "Seismic Evaluation Procedure for Equipment in U.S. Department of Energy Facilities," DOE/EH-0545, United States Department of Energy, Washington, D.C., March 1997.

EPRI, 1994, "Methodology for Developing Seismic Fragilities," EPRI TR-103959, Prepared by Jack R. Benjamin and Associates, Inc. and RPK Structural Mechanics Consulting for the Electric Power Research Institute, Palo Alto, CA, 1994.

EPRI, 2009, "Seismic Fragility Application Guide Update," prepared by Kennedy, R., G. Hardy, and K. Merz for the Electric Power Research Institute, EPRI 1019200, Palo Alto, CA, 2009.

Gaston, D., G. Hansen, and C. Newman, 2009. "MOOSE: A Parallel Computational Framework for Coupled Systems for Nonlinear Equations," in International Conference on Mathematics, Computational Methods, and Reactor Physics, Saratoga Springs, NY, 2009.

Groholski, D. R., Y. M. A. Hashash, M. Musgrove, J. Harmon, and B. Kim, 2015, "Evaluation of 1-D Nonlinear Site Response Analysis Using a General Quadratic/Hyperbolic Strength Controlled Constitutive Model," 6th International Conference on Earthquake Geotechnical Engineering, Christchurch, New Zealand.

Hashash, Y. M. A., D. R. Groholski, C. A. Phillips, D. Park and M. Musgrove, 2011, "DEEPSOIL 5.0 User Manual and Tutorial". 2011.

INL, 2003, "Seismic Evaluation for Electrical Cabinets 670 E 23, 670 E 28, 670 E 103, 670 E 105, 670 E 116, and 670 E 459," EDF-4316, Idaho National Laboratory, Idaho Falls, ID. 2003.

Iwan W. D., 1967, "On a Class of Models for the Yielding Behavior of Continuous and Composite Systems," Journal of Applied Mechanics, Vol. 34, No. 3, pp. 612-617.

LSTC, 2013, LS-DYNA Keyword User's Manual-Version R 7.0., Livermore Software Technology Corporation, Livermore, California. 2013.

Luco, J.E. and H.L. Wong, 1980, "Soil-Structure Interaction: A Linear Continuum Mechanics Approach (CLASSI)," Report CE79-03, University of Southern California, Los Angeles, CA.

Lysmer, J. and R. L. Kuhlemeyer, 1969, "Finite Dynamic Model for Infinite Media," Journal of the Engineering Mechanics Division, Proc. American Society of Civil Engineers, Vol. 95, EM4, pp. 859-876.

Masing, G., 1926, "Eiganspannungen and Verfestigung beim Messing," Journal of Geotechnical Engineering.

NEI, 2012, "Diverse and Flexible Coping Strategies (FLEX) Implementation Guide," Report 12-06, Nuclear Energy Institute, August 2012.

NRC, 2012a, "Central and Eastern United States Seismic Source Characterization for Nuclear Facilities" NUREG-2115, Nuclear Regulatory Commission. March 2012.

NRC, 2012b, "Practical Implementation Guidelines for SSHAC Level 3 and 4 Hazard Studies" NUREG-2117, Nuclear Regulatory Commission. April 2012.

NRC, 2013, "State-of-the-Art Reactor Consequence Analyses Project. Volume 2: Surry Integrated Analysis," NUREG/CR-7110, Vol. 2, Rev. 1, Nuclear Regulatory Commission, August 2013.

OpenSees version 2.5.0 - http://opensees.berkeley.edu/

Ostadan, F., 2006, "SASSI2000: A System for Analysis of Soil Structure Interaction - User's Manual," University of California, Berkeley, California.

Parisi, C., S. R. Prescott, R. H. Szilard, J. L. Coleman, R. E. Spears and A. Gupta, 2016, "Demonstration of External Hazards Analysis," INL/EXT-16-39353, Idaho National Laboratory, Idaho Falls, Idaho, July 2016.

Prescott, S., C. Smith, R. Samptah, 2014, "Incorporating dynamic 3D simulation into PRA", INL/CON-14-33680, Idaho National Laboratory, Idaho Falls, Idaho, 2014.

Sampath, R., N. Montanari, N. Akinci, 2016, "Large-scale solitary wave simulation with implicit incompressible SPH," Journal of Ocean Engineering and Marine Energy. 2016, 10.1007/s40722-016-0060-8.

Spears, R. and J. Coleman, 2014, "Nonlinear Time Domain Soil-Structure Interaction Methodology Development," INL/EXT-14-33126, Idaho National Laboratory, Idaho Falls, Idaho.

Virginia Electric and Power Company (Dominion), 2007, "Surry Power Station Units 1 and 2: Updated Final Safety Analysis Report," Revision 39, September 2007. (NRC ADAMS accession no. ML072980795)

Willford, M., R. Sturt, Y. Huang, I. Almufti and X. Duan, 2010, "Recent Advances in Nonlinear Soil-Structure Interaction Analysis using LS-DYNA." Proceedings of the NEA-SSI Workshop, October 6-8, 2010, Ottawa, Canada.

APPENDIX A – EMRALD MODEL DATA

	Type	Component	FTS/FTO			FTR			Seismic-FTR		3DVar
				Prob		Lambda	Prob		Variable Lambda		
1	Pump	AFW_MDP_P1	_FS	2.23E-03	_FR	4.54E-06	1.09E-04	_SI	Seis_AFW_MDP_SCBP1		
2	Pump	AFW_MDP_P2	_FS	2.23E-03	_FR	4.54E-06	1.09E-04	_SI	Seis_AFW_MDP_SCBP2		
3	Pump	AFW_MDP_P3	_FS	2.23E-03	_FR	4.54E-06	1.09E-04	_SI	Seis_AFW_MDP_SCBP3		
4	Pump	AFW_MDP_P4	_FS	2.23E-03	_FR	4.54E-06	1.09E-04	_SI	Seis_AFW_MDP_SCBP4		
5	MOV	AFW_MOV_CRL1			_FF	4.54E-06	3.63E-05				
6	MOV	AFW_MOV_CRL2			_FF	4.54E-06	3.63E-05				
7	MOV	AFW_MOV_CRL3			_FF	4.54E-06	3.63E-05				
8	MOV	AFW_MOV_CRL4			_FF	4.54E-06	3.63E-05				
9	CKV	AFW_CKV_CKVE5	_FO	1.30E-05							
10	CKV	AFW_CKV_CKVE6	_FO	1.30E-05							
11	CKV	AFW_CKV_CKVE7	_FO	1.30E-05							
12	CKV	AFW_CKV_CKVE8	_FO	1.30E-05							
13	BAT	UDC_BAT_BAT1A			_FO	1.86E-06	1.49E-05	_SI	Seis_UDC_BAT_BAT1A		BAT_1_A
14	BAT	UDC_BAT_BAT1B			_FO	1.86E-06	1.49E-05	_SI	Seis_UDC_BAT_BAT1B		BAT_1_B
15	BAT	UDC_BAT_BAT2A			_FO	1.86E-06	1.49E-05	_SI	Seis_UDC_BAT_BAT2A		BAT_2_A
16	BAT	UDC_BAT_BAT2B			_FO	1.86E-06	1.49E-05	_SI	Seis_UDC_BAT_BAT2B		BAT_2_B
17	CBK	UDC_CBK_BAT1ACB1			_SO	1.71E-07	1.37E-06	_SI	Seis_UDC_CBK_BAT1ACB1		UPS_1_A
18	CBK	UDC_CBK_BAT2ACB1			_SO	1.71E-07	1.37E-06	_SI	Seis_UDC_CBK_BAT2ACB1		UPS_2_A
19	CBK	UDC_CBK_BAT1BCB1						_SI	Seis_UDC_CBK_BAT1BCB1		UPS_1_B
20	CBK	UDC_CBK_BAT2BCB1						_SI	Seis_UDC_CBK_BAT2BCB1		UPS_2_B
21	MCC	CST_MU_SUPPLY1			_FO	2.00E-06	4.80E-05				
22	MCC	CST_MU_SUPPLY2			_FO	2.00E-06	4.80E-05				
23	UDC	UDC_125VDC_1	_FO	1.00E-04							UDC_125VDC_PNL_1
24	UDC	UDC_125VDC_1	_FO	1.00E-04							UDC_125VDC_PNL_1
25	DGP	DGP_BAC_MRBE3			_FF	4.17E-07	1.00E-05	_SI	Seis_DGP_BAC_MRBE3		
26	DGP	DGP_DGN_DG1	_FS	4.53E-03	_FR	2.89E-03	6.70E-02	_SI	Seis_DGP_DGN_DG1		
27	DGP	DGP_DGN_DG2	_FS	4.53E-03	_FR	2.89E-03	6.70E-02	_SI	Seis_DGP_DGN_DG2		
28	DGP	DGP_CBK_EDBE5	_FC	2.55E-03	_SO	1.71E-07	4.10E-06	_SI	Seis_DGP_CBK_EDBE5		
29	DGP	DGP_CBK_EDBE6	_FC	2.55E-03	_SO	1.71E-07	4.10E-06	_SI	Seis_DGP_CBK_EDBE6		
30	DGP	DGP_RLY_67E327GB	_FF	2.50E-05				_SI	Seis_DGP_RLY_67E327GB		
31	RPS	PPI_SYS_OPIORPS	_FF	3.00E-07							

Figure 103. EMRALD components and their failure event probability values.

Component Seismic Event	Dynamic Failure Probability by PGA			
	PGA < .5	PGA .5 to 1.0	PGA 1.0 to 1.75	PGA > 1.75
Seis_AFW_MDP_SCBP1	0	1.37E-10	4.20E-02	5.97E-01
Seis_AFW_MDP_SCBP2	0	1.37E-10	4.20E-02	5.97E-01
Seis_AFW_MDP_SCBP3	0	1.37E-10	4.20E-02	5.97E-01
Seis_AFW_MDP_SCBP4	0	1.37E-10	4.20E-02	5.97E-01
Seis_UDC_BAT_BAT1A	0	1.32E-17	4.21E-04	1.29E-01
Seis_UDC_BAT_BAT1B	0	1.32E-17	4.21E-04	1.29E-01
Seis_UDC_BAT_BAT2A	0	1.32E-17	4.21E-04	1.29E-01
Seis_UDC_BAT_BAT2B	0	1.32E-17	4.21E-04	1.29E-01
Seis_UDC_CBK_BAT1ACB1	0	1.37E-10	4.20E-02	5.97E-01
Seis_UDC_CBK_BAT2ACB1	0	1.37E-10	4.20E-02	5.97E-01
Seis_UDC_CBK_BAT1BCB1	0	1.37E-10	4.20E-02	5.97E-01
Seis_UDC_CBK_BAT2BCB1	0	1.37E-10	4.20E-02	5.97E-01
Seis_DGP_BAC_MRBE3	0	2.86E-19	3.18E-02	8.81E-01
Seis_DGP_DGN_DG1	0	4.97E-25	7.80E-03	8.33E-01
Seis_DGP_DGN_DG2	0	4.97E-25	7.80E-03	8.33E-01
Seis_DGP_CBK_EDBE5	0	1.37E-19	4.20E-02	5.97E-01
Seis_DGP_CBK_EDBE6	0	1.37E-19	4.20E-02	5.97E-01
Seis_DGP_RLY_67E327GB	0	2.86E-19	3.18E-02	8.81E-01

Figure 104. Dynamic failure rates for components depending on the PGA value sampled.

APPENDIX B – RELAP5-3D TRANSIENT RESULTS

B.1 Mitigated LTSBO – 21 gpm leakage
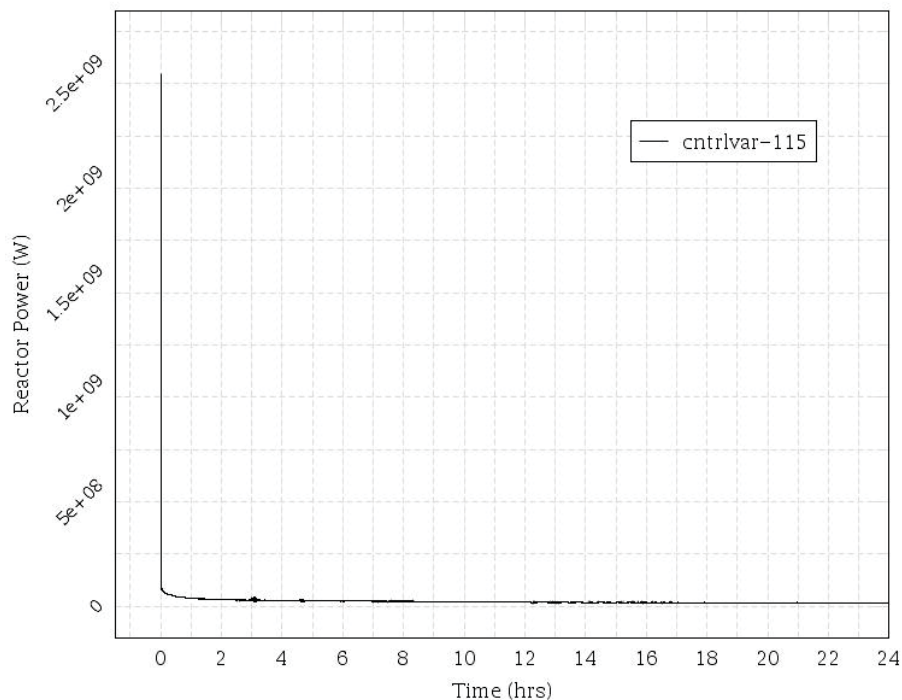
Figure 105. MLTSBO – Reactor Power.
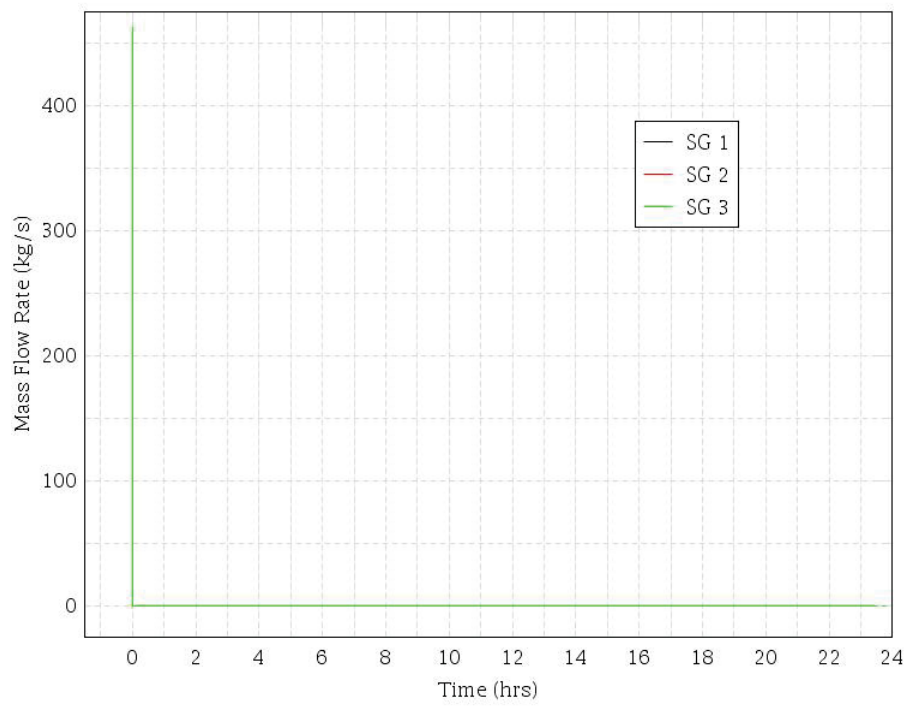
Figure 106. MLTSBO – SG Mass Flow.
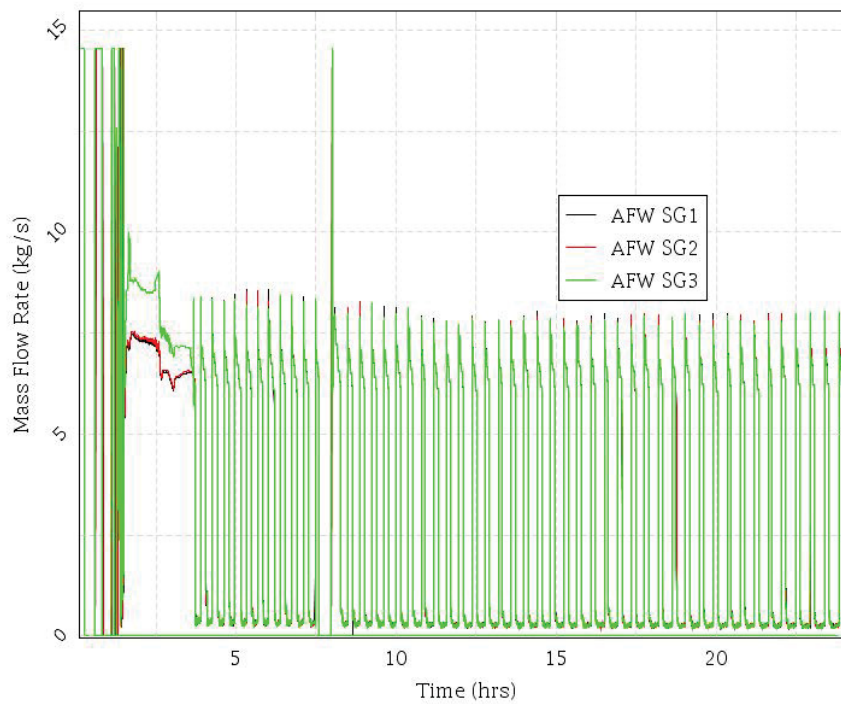
Figure 107. MLTSBO – TD-AFW Mass Flow.
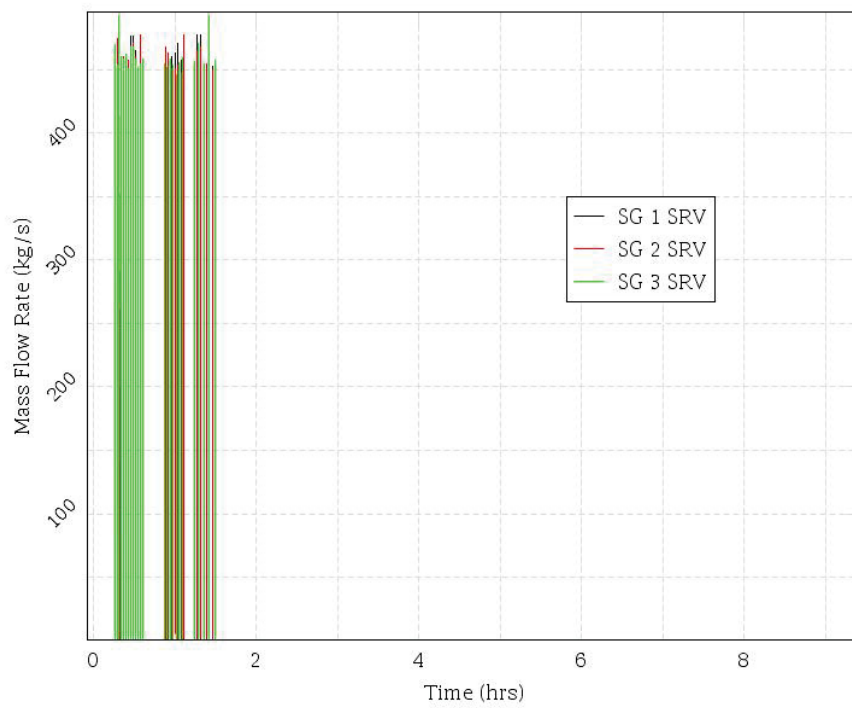
Figure 108. MLTSBO – SG SRV Mass Flow.
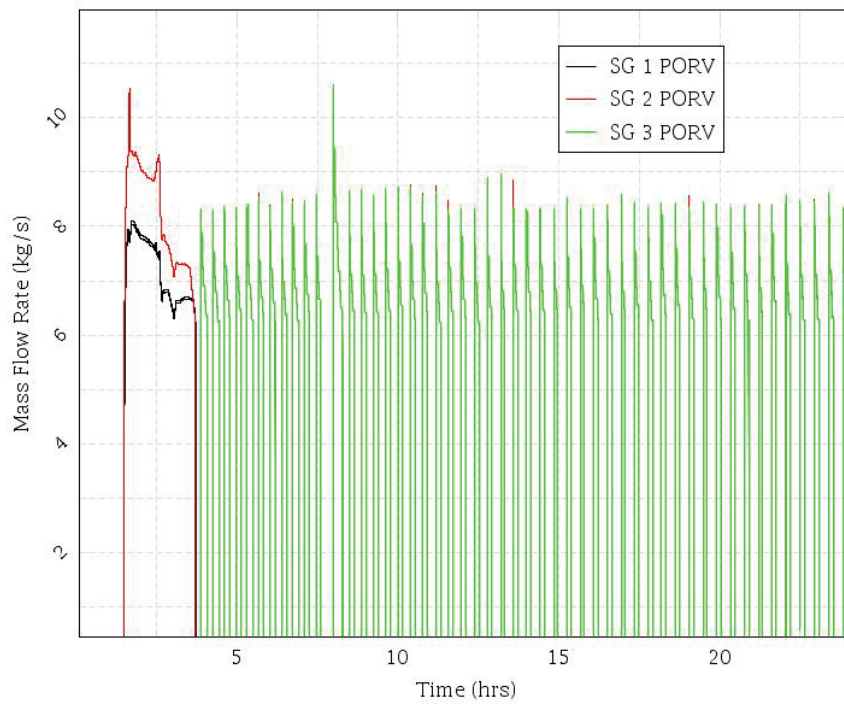
Figure 109. MLTSBO – SG PORV Mass Flow.
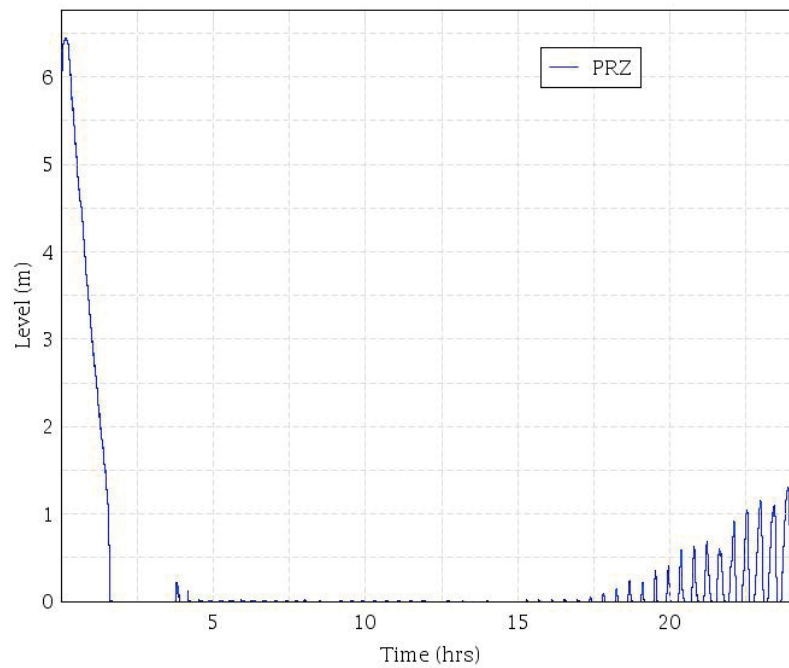
Figure 110. MLTSBO – PRZ Level.
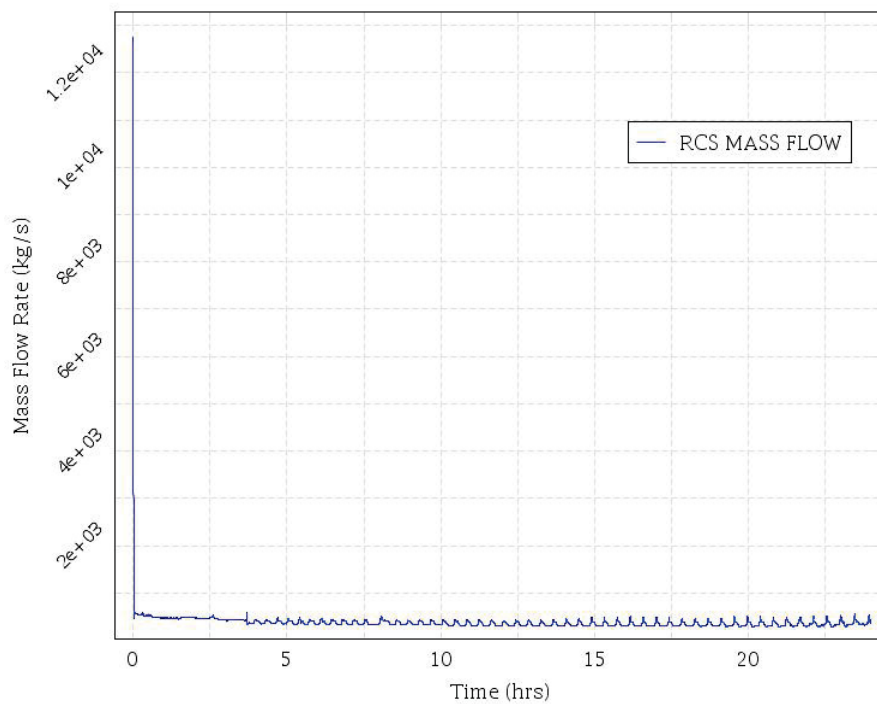
Figure 111. MLTSBO – RCS Total Mass Flow.

140
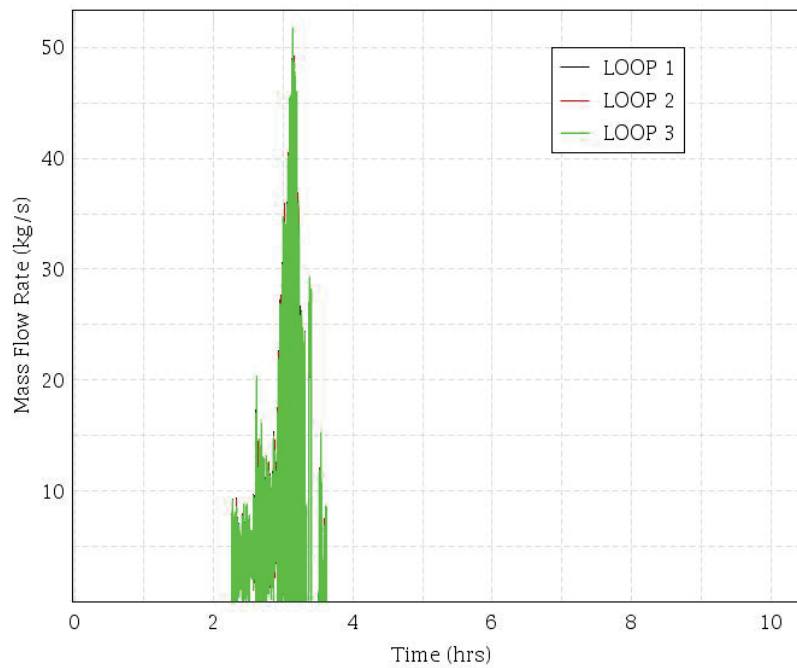
Figure 112. MLTSBO – Accumulators Mass Flow.

B.2 Mitigated LTSBO – 182 gpm leakage
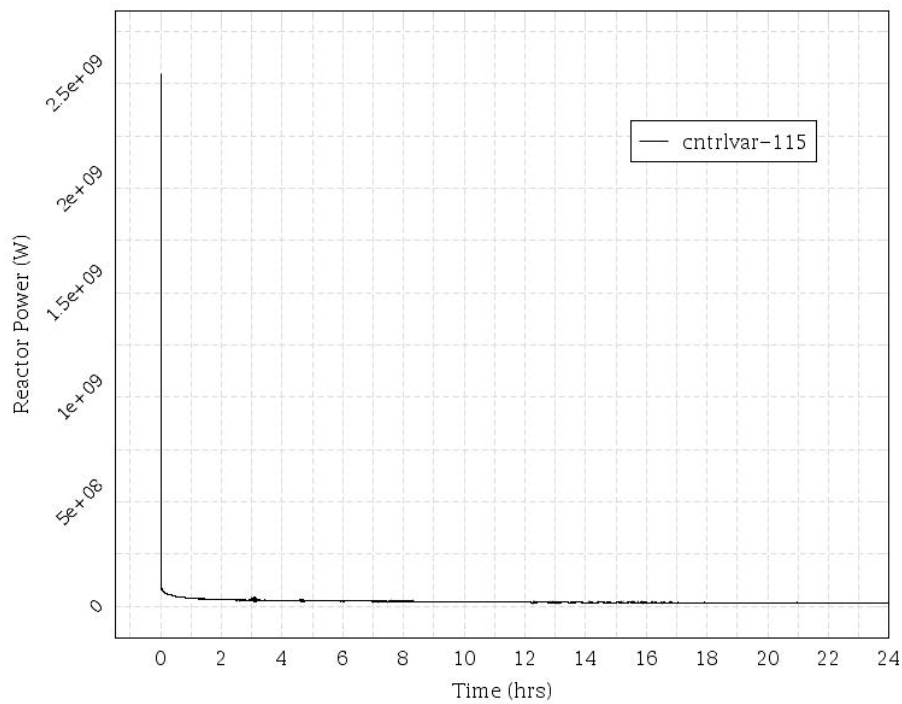
Figure 113. MLTSBO and 182 gpm LOCA – Reactor Power.
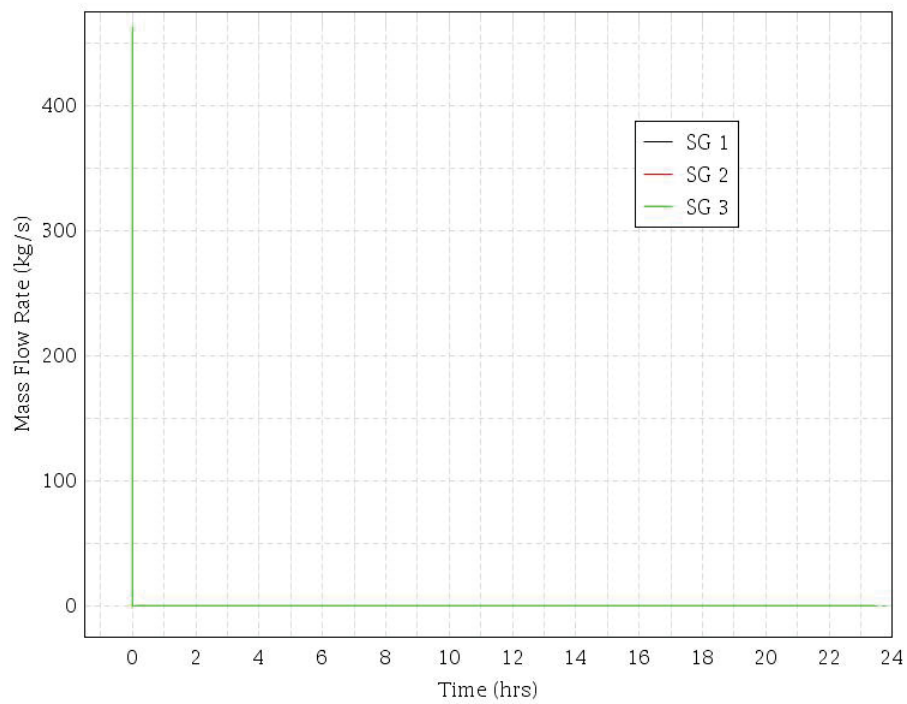
Figure 114. MLTSBO and 182 gpm LOCA – SG Mass Flow
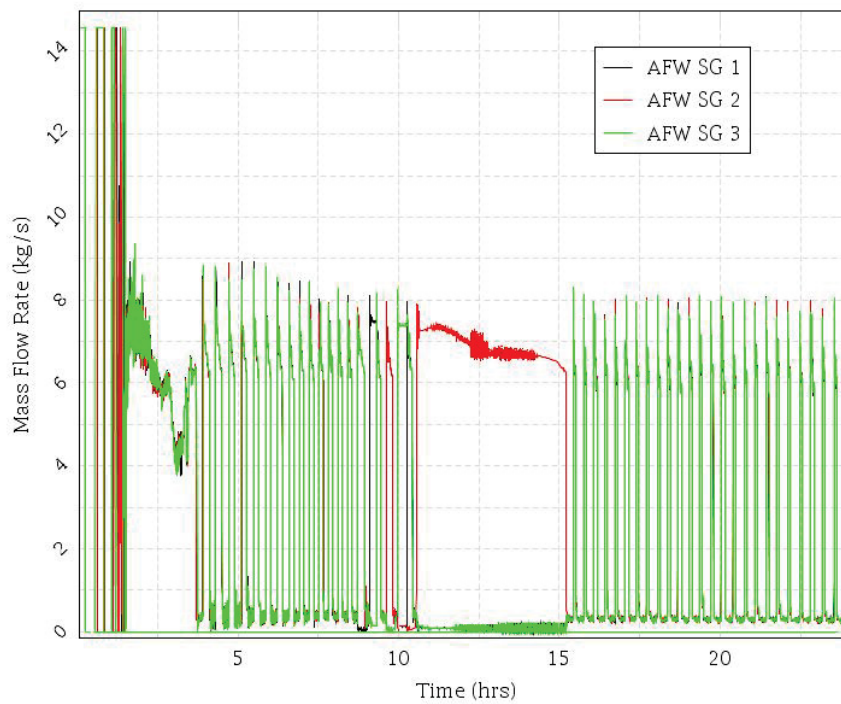
Figure 115. MLTSBO and 182 gpm LOCA – TD-AFW Mass Flow.
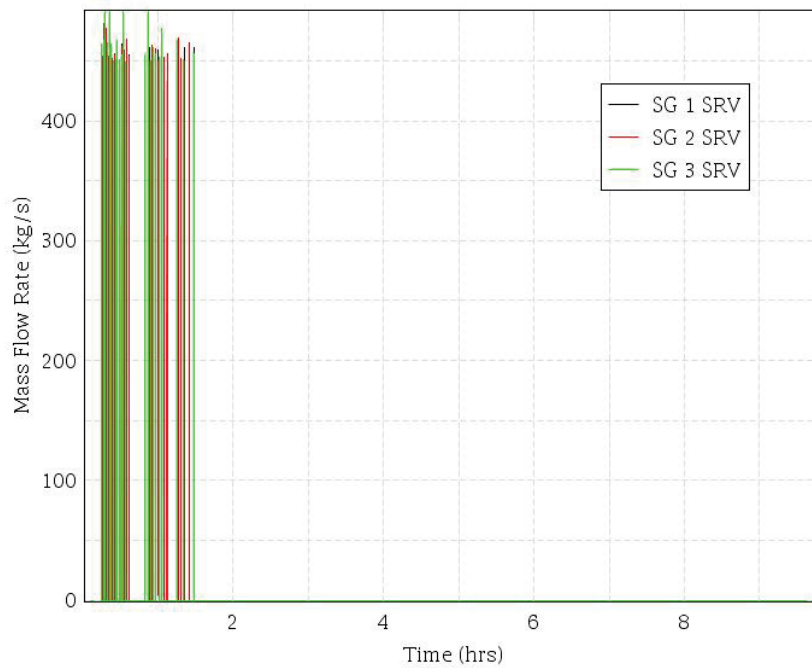
Figure 116. MLTSBO and 182 gpm LOCA – SG SRV Mass Flow.
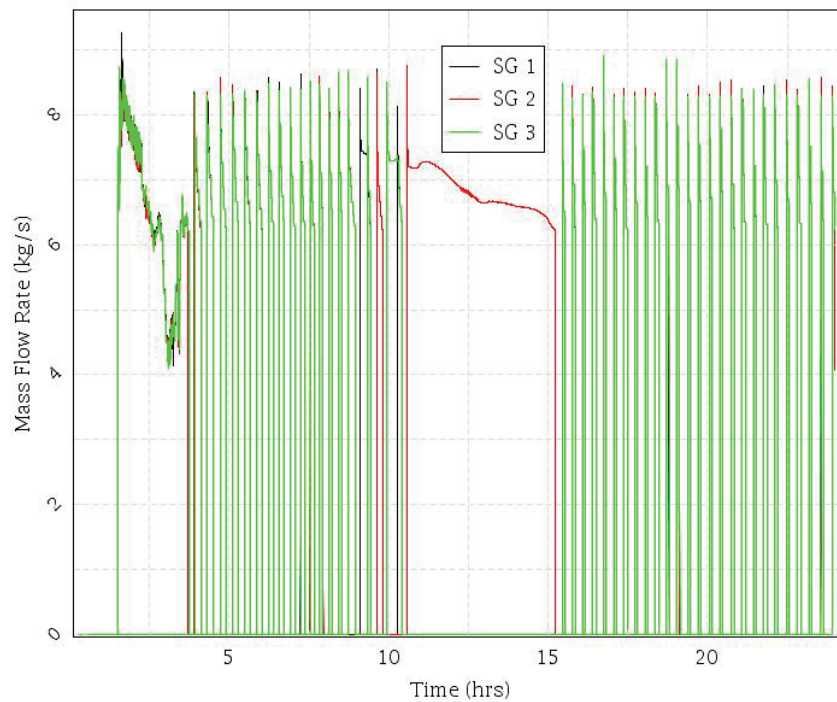
Figure 117. MLTSBO and 182 gpm LOCA – SG PORV Mass Flow.
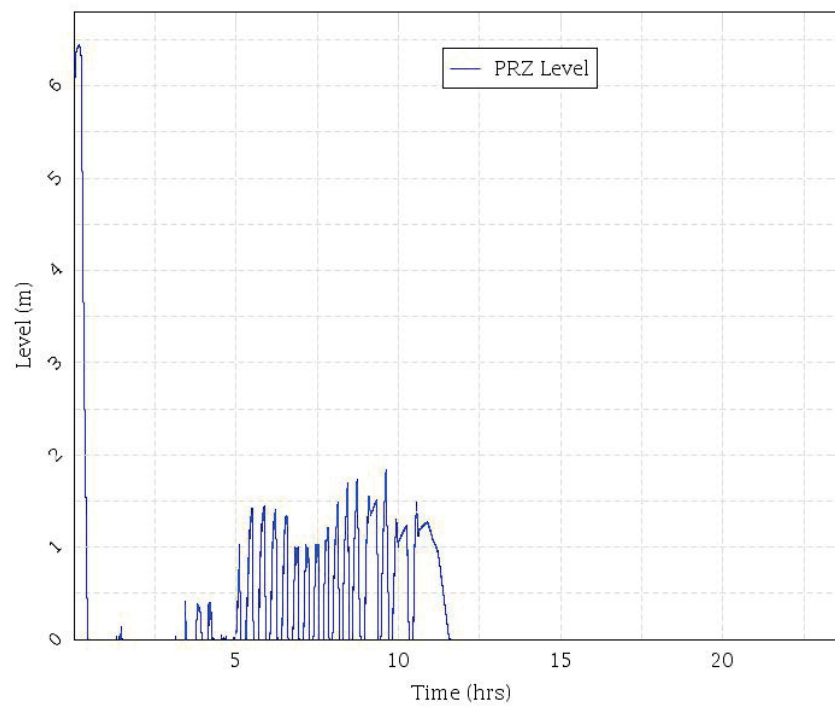
Figure 118. MLTSBO and 182 gpm LOCA – PRZ Level.
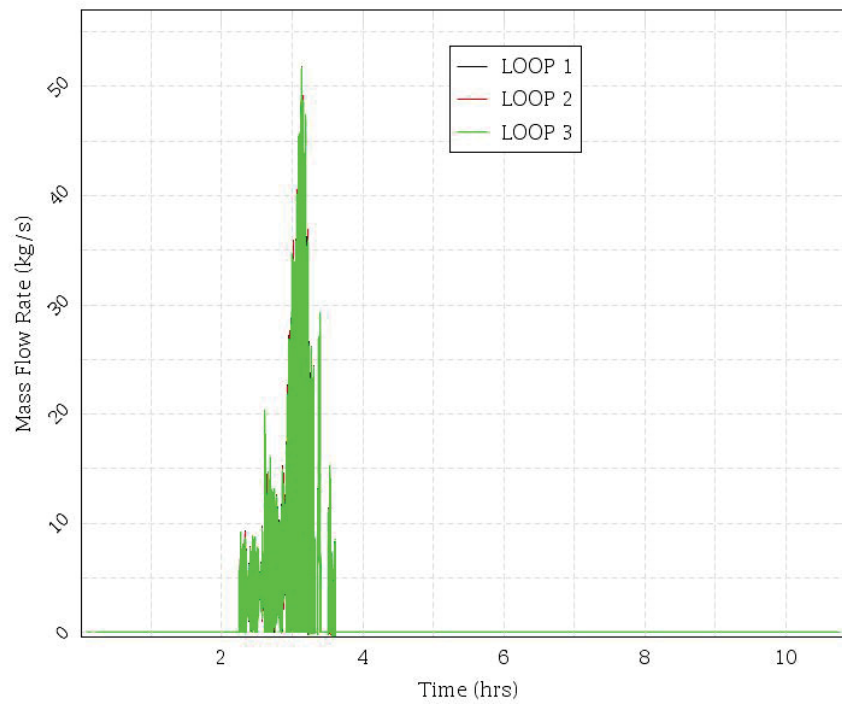
Figure 119. MLTSBO and 182 gpm LOCA – Accumulators Mass Flow.
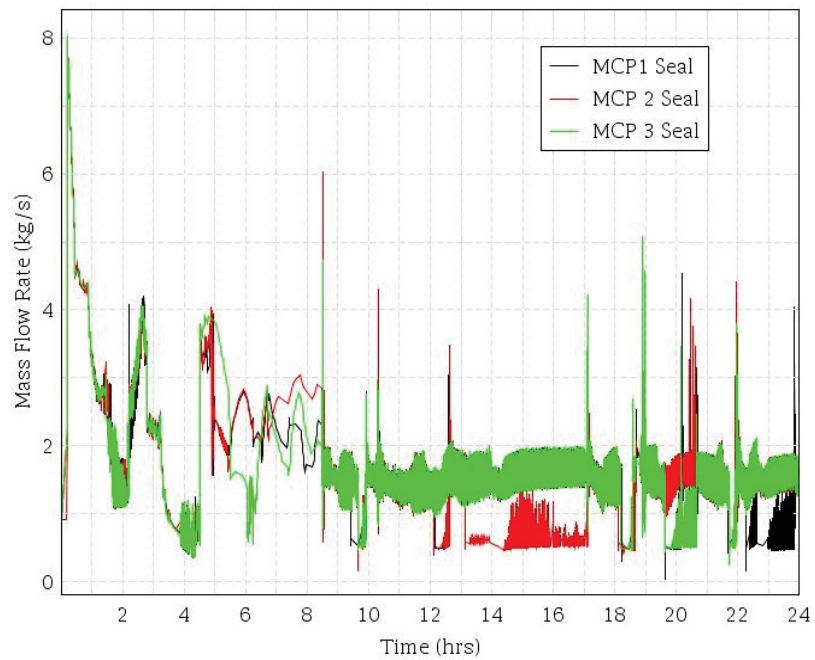
Figure 120. MLTSBO and 182 gpm LOCA and Battery Failure – MCP Seal Leakage.
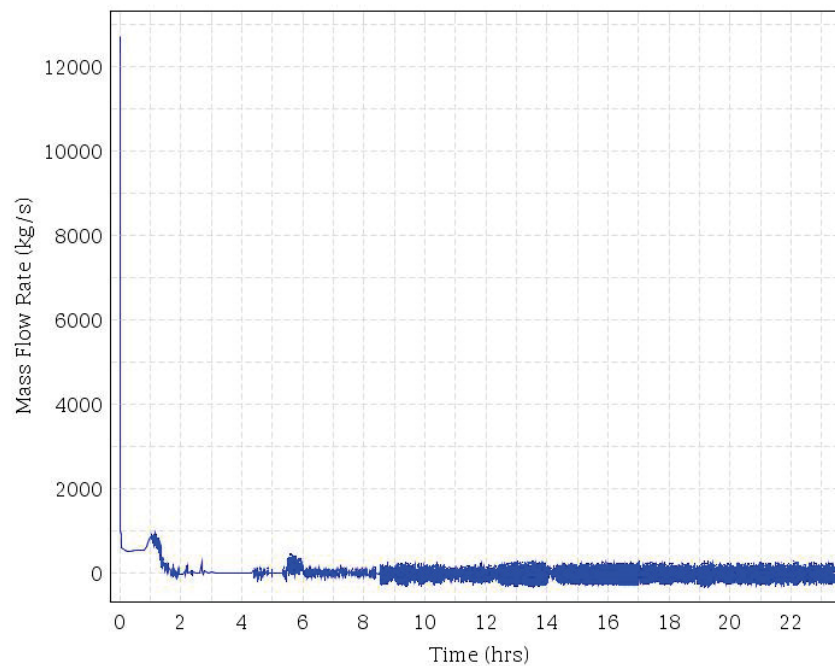
Figure 121. MLTSBO and 182 gpm LOCA and Battery Failure – RCS Mass Flow.

145
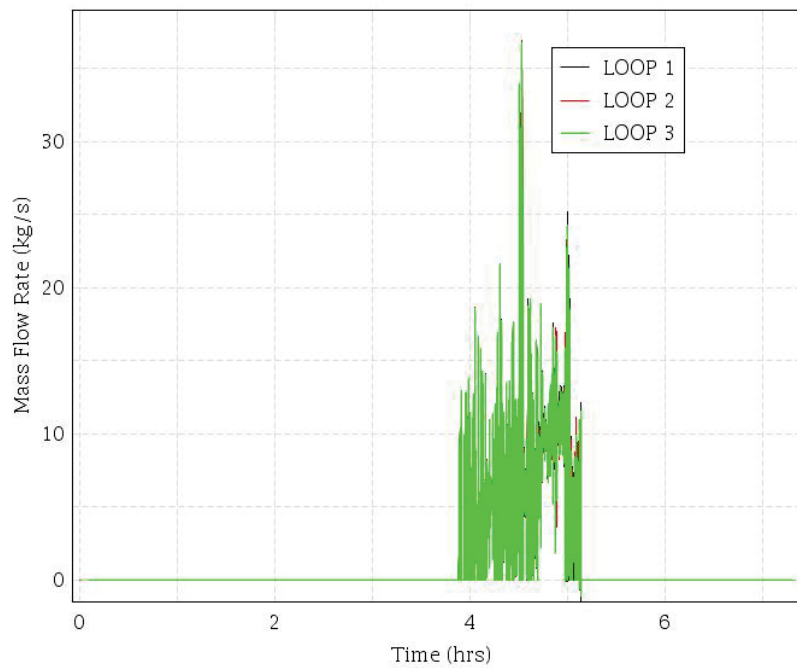
Figure 122. MLTSBO and 182 gpm LOCA and Battery Failure – Accumulators Mass Flow.
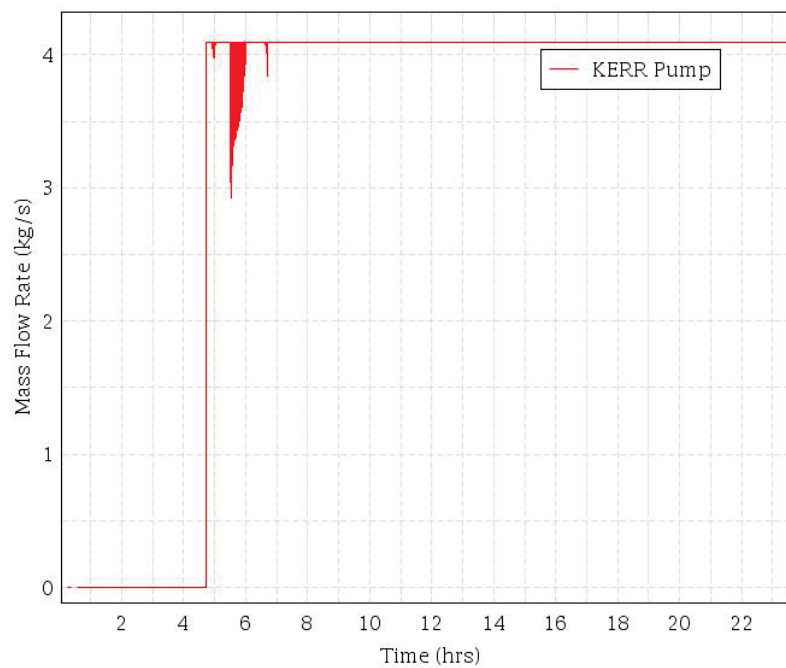
Figure 123. MLTSBO and 182 gpm LOCA and Battery Failure – Kerr Pump Injection Mass Flow.

146

B.4 Sensitivity Analysis
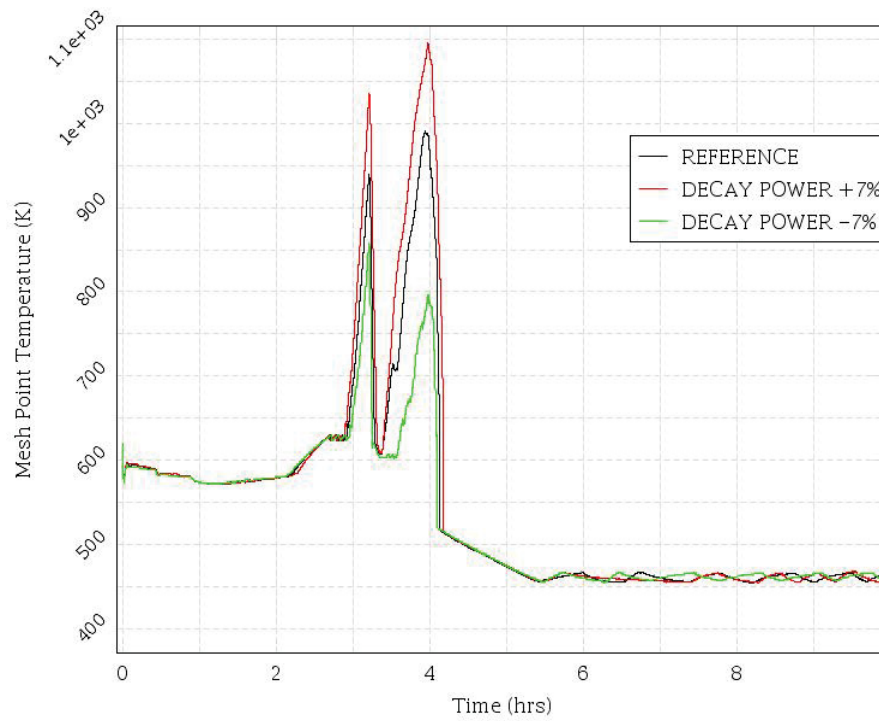
Figure 124. Sensitivity on Decay Power – PCT.
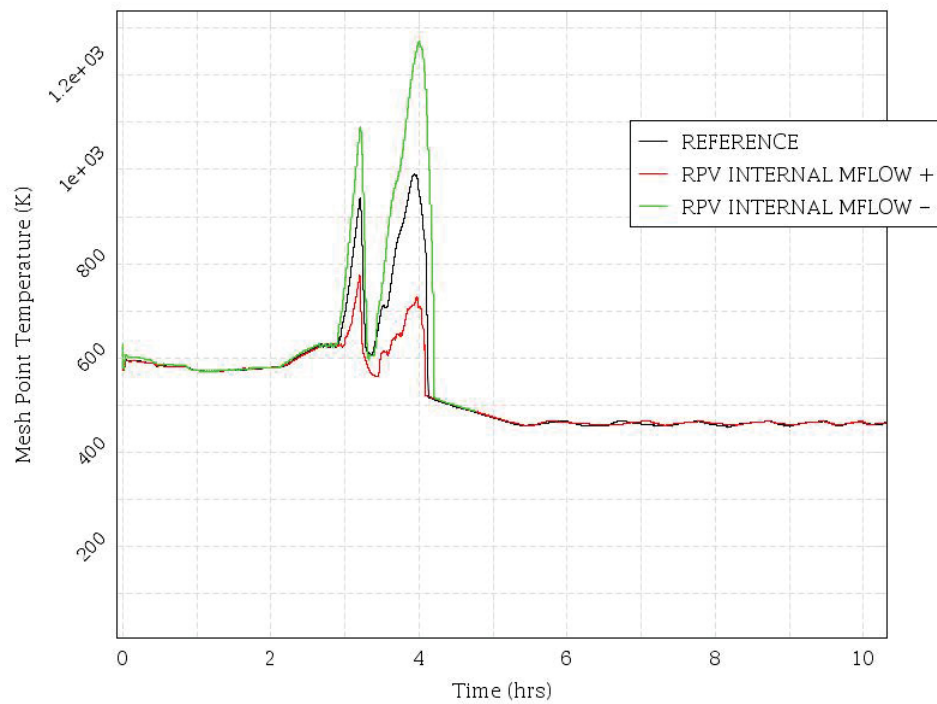
Figure 125. Sensitivity on RPV Internal Mass Flow – PCT.
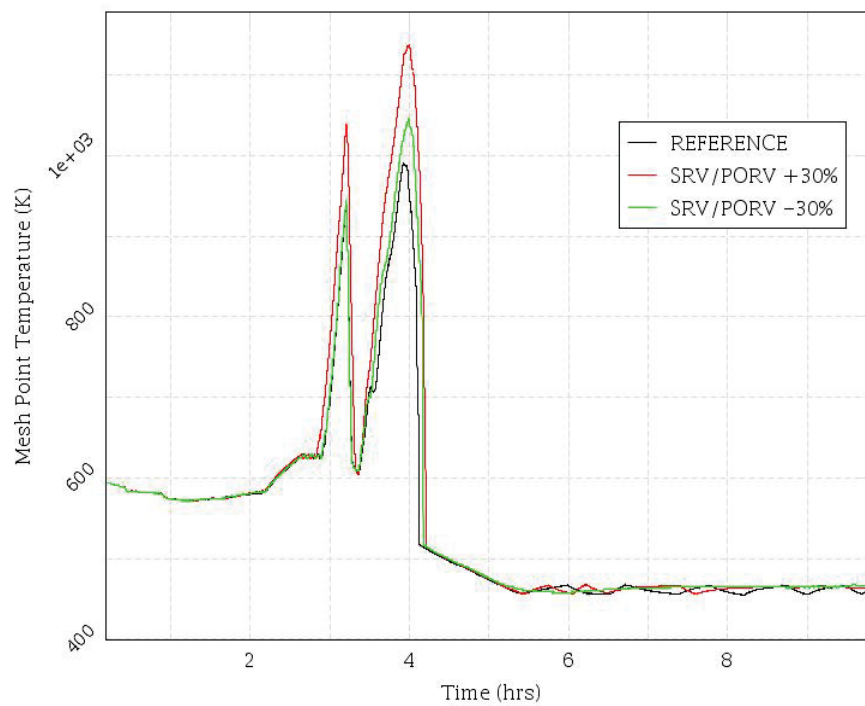
Figure 126. Sensitivity on SG and PRZ Valve Flow Areas – PCT.
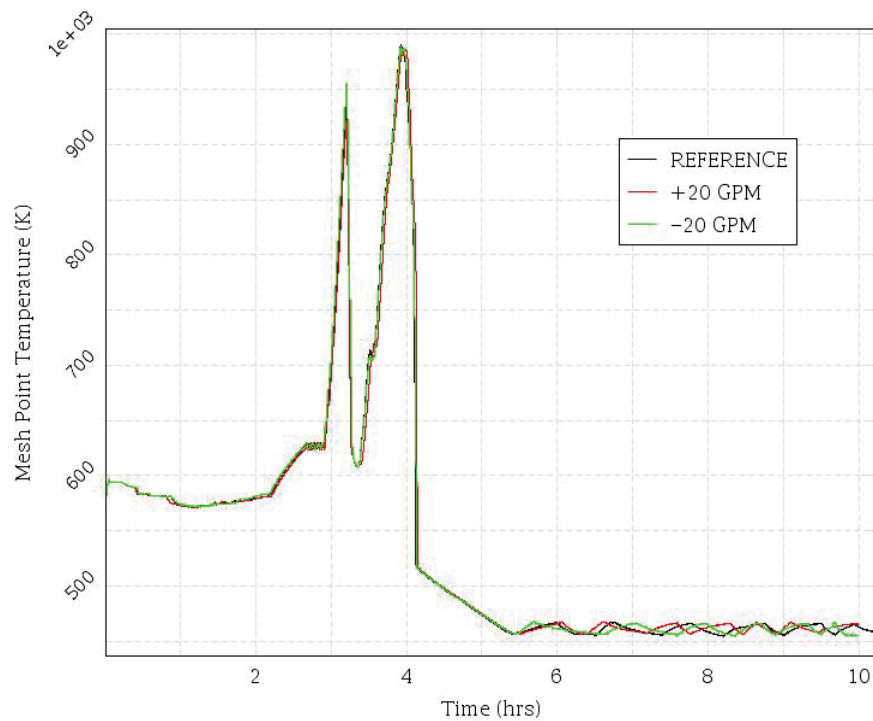
Figure 127. Sensitivity on MCP Seal LOCA – PCT.

148
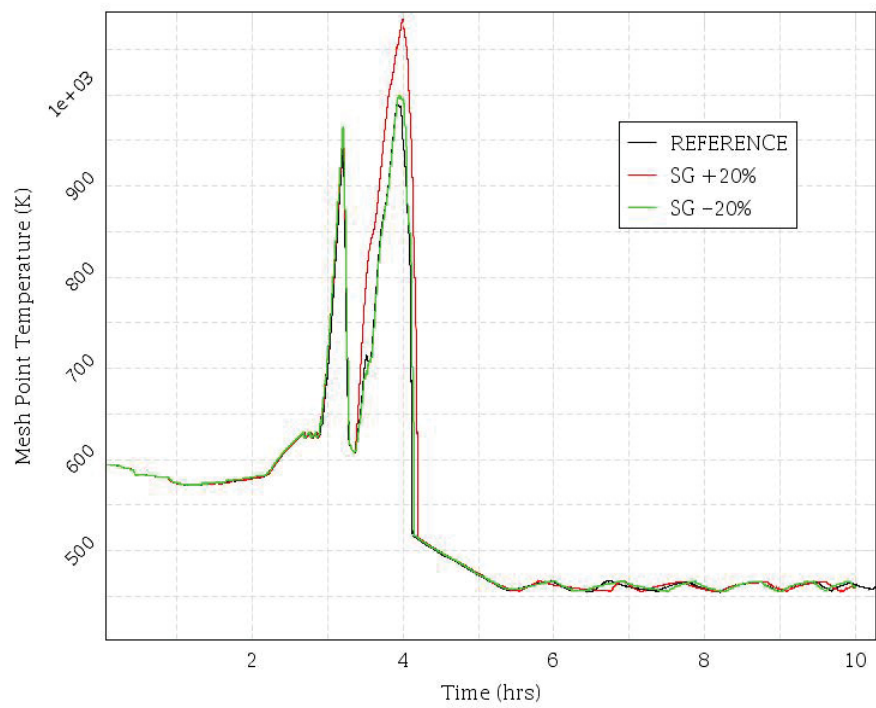
Figure 128. Sensitivity on SG Heat Transfer Coefficient – PCT.

APPENDIX C – TIME-DEPENDENT FRAGILITY SURFACES

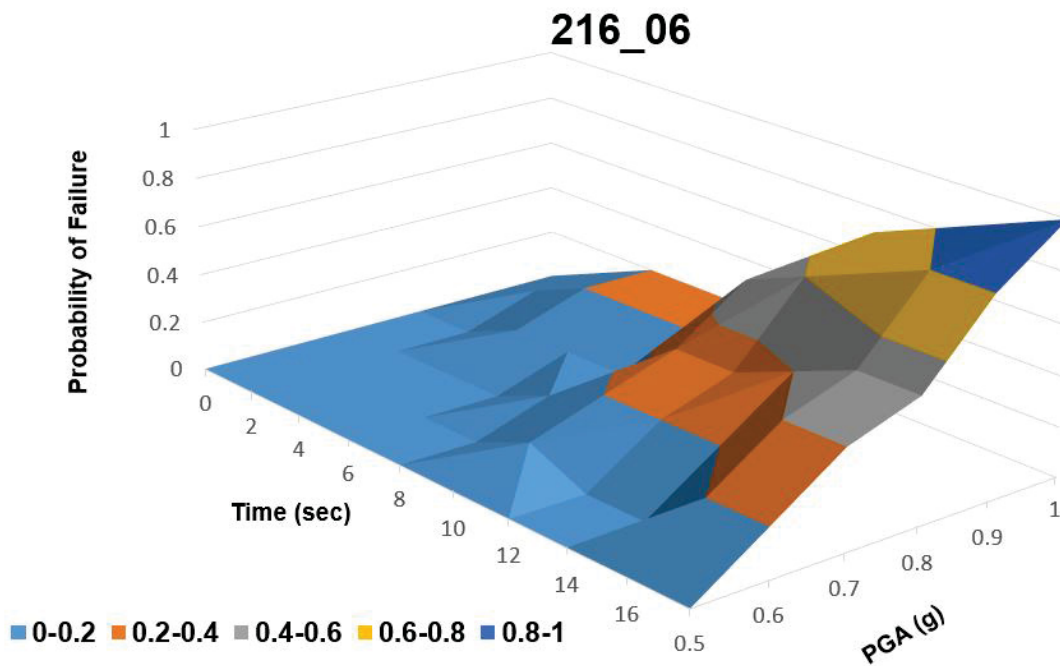*B.1 Mitigated LTSBO – 21 gpm leakage*
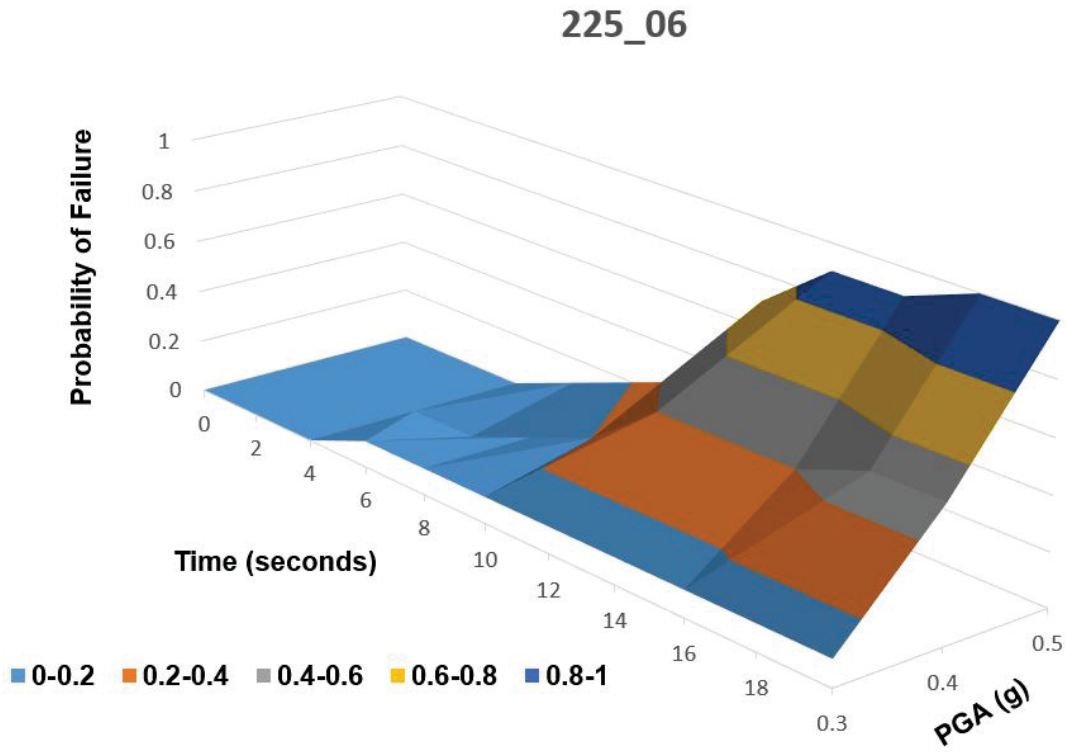
225_06

Figure 129. Time-dependent fragility surface for node 225_06

21
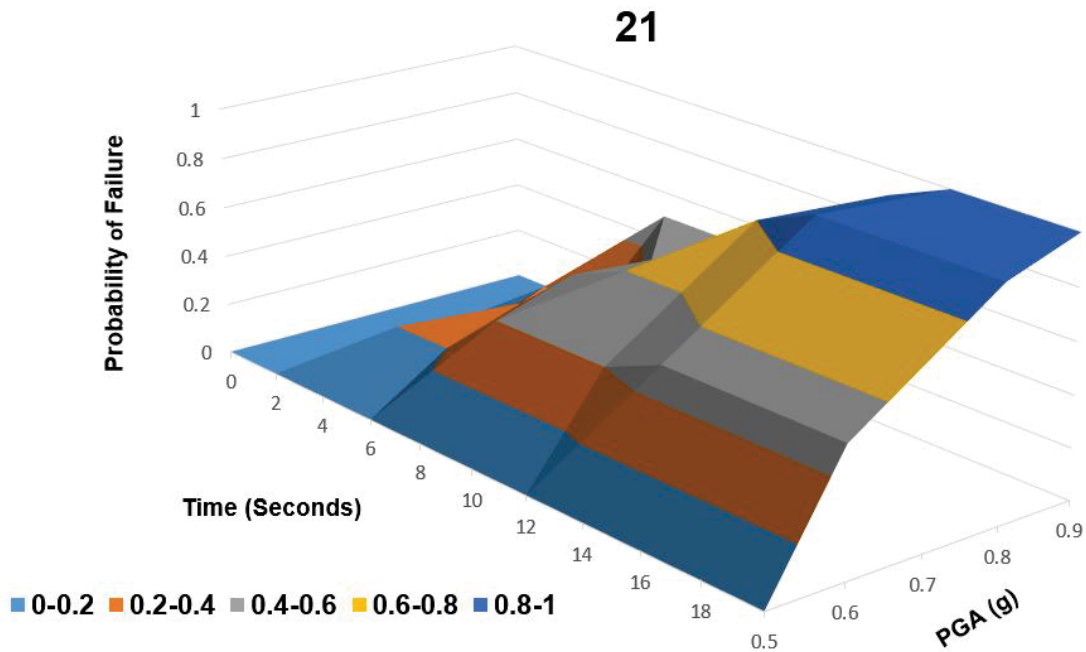
Figure 130. Time-dependent fragility surface for node 21

151
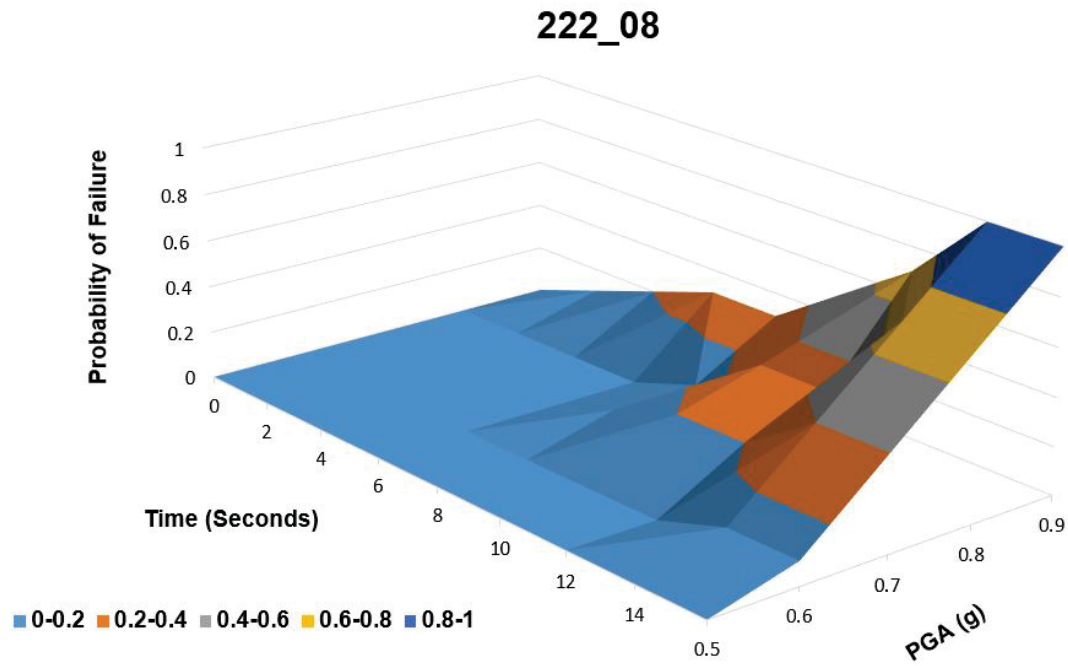
Figure 131. Time-dependent fragility surface for node 225222_08
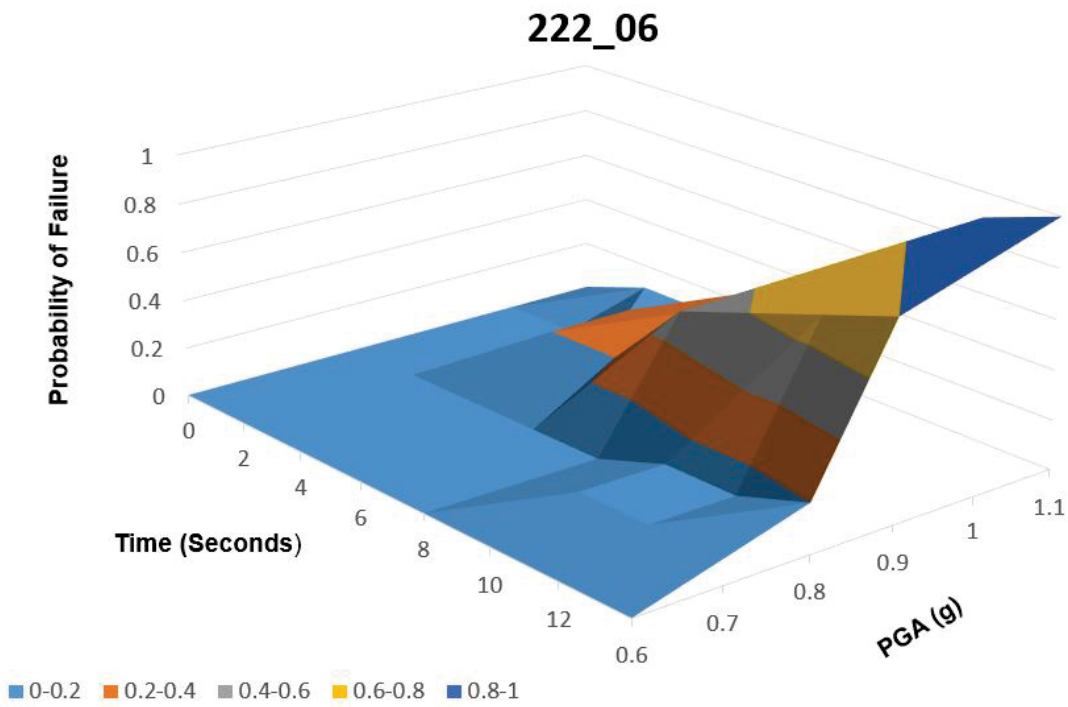
Figure 132. Time-dependent fragility surface for node 222_06
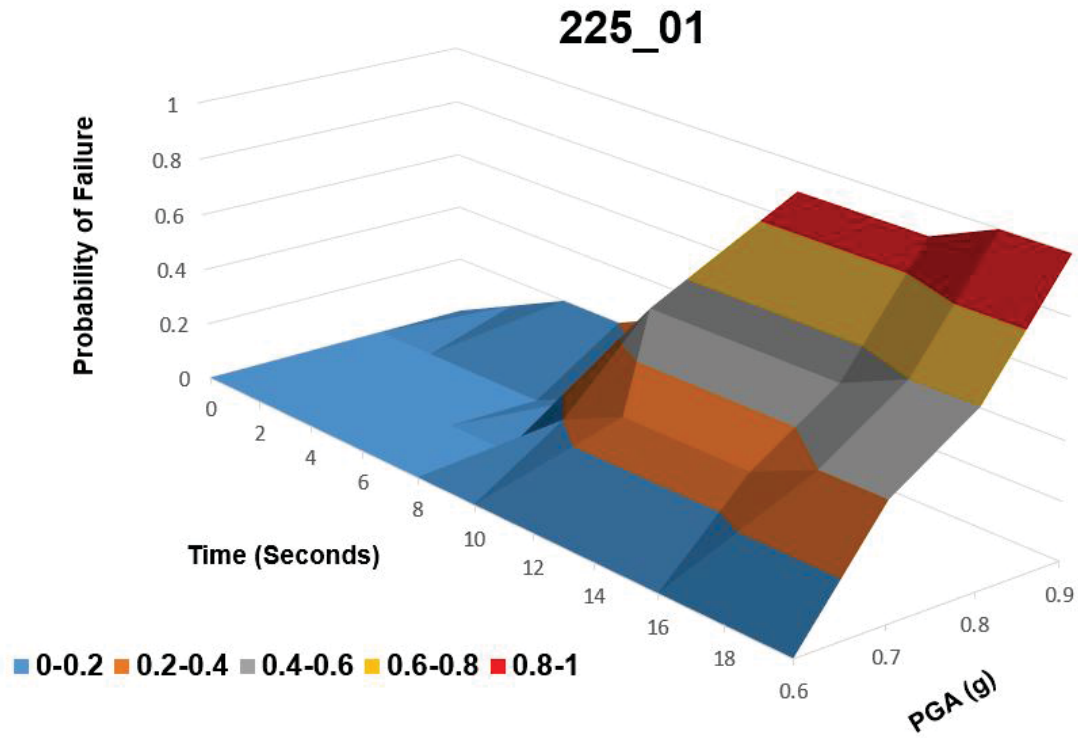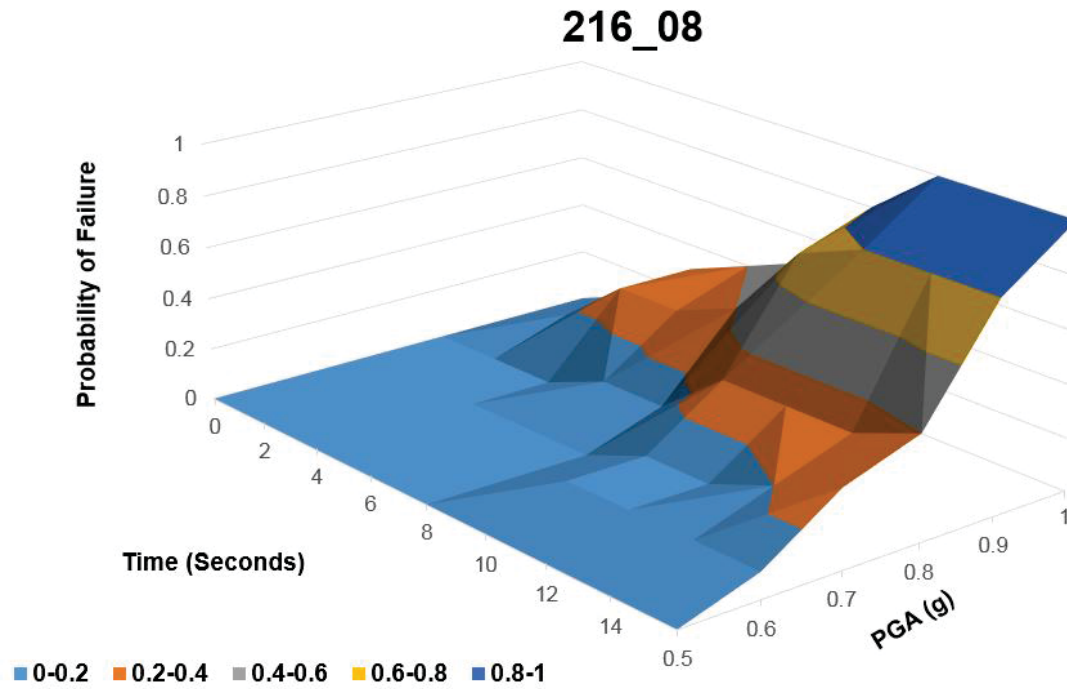
Figure 133. Time-dependent fragility surface for node 225_01

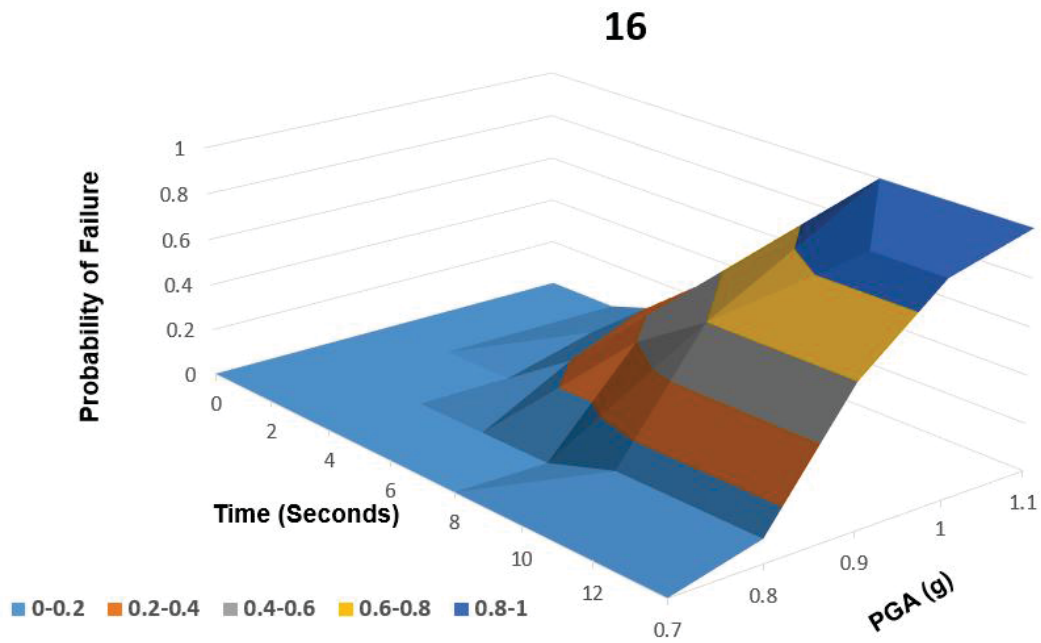Figure 134. Time-dependent fragility surface for node 216_06

216_08

Figure 135. Time-dependent fragility surface for node 216_08

16

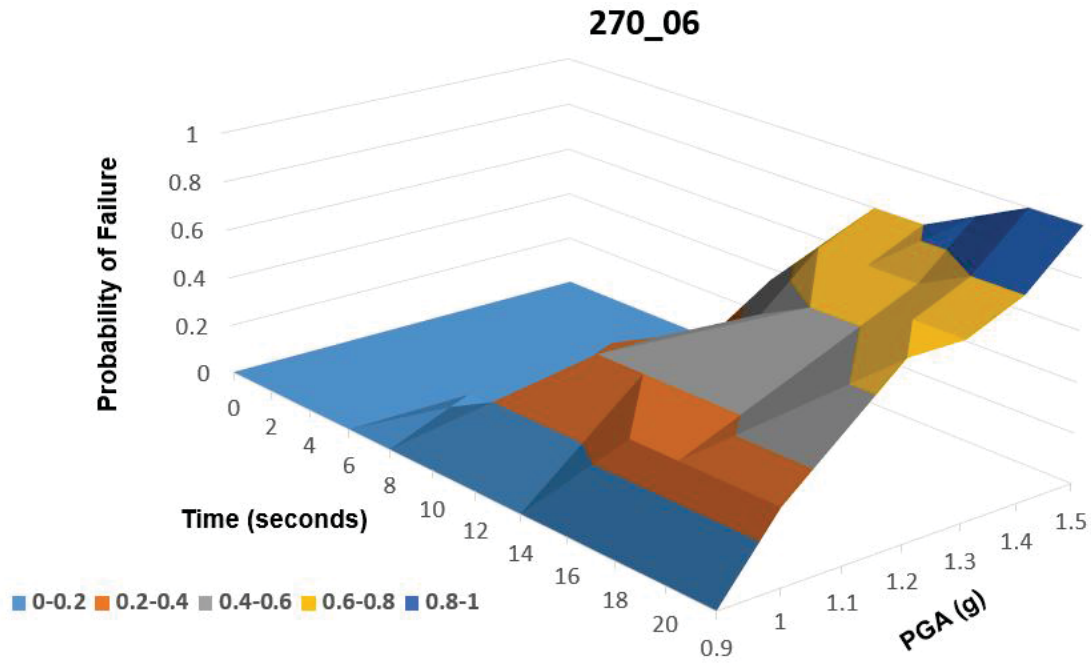Figure 136. Time-dependent fragility surface for node 16
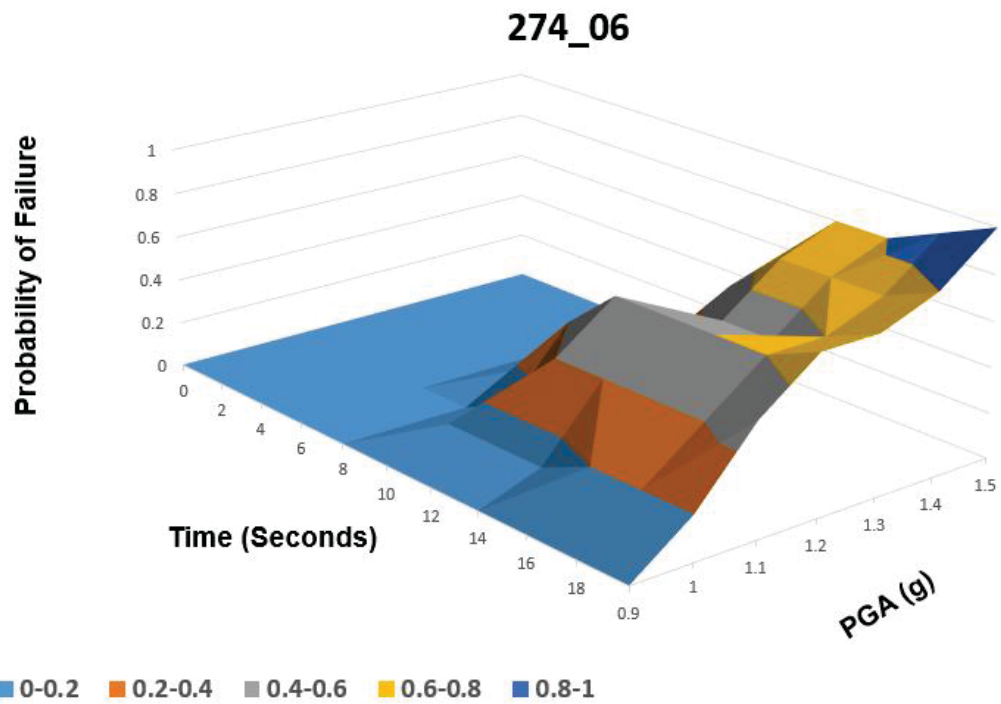
Figure 137. Time-dependent fragility surface for node 270_06

Figure 138. Time-dependent fragility surface for node 274_06